Synthesis of ferroelectric oxides for photovoltaic applications

Alessandro Quattropani

UNIVERSITÉ DE STRASBOURG

ÉCOLE DOCTORALE Mathématiques, Science de l'Information et de l'Ingénieur
UMR 7357

THÈSE présentée par :

Alessandro QUATTROPANI

soutenue le : **17 Décembre 2018**

pour obtenir le grade de : **Docteur de l'université de Strasbourg**

Discipline/ Spécialité : Science des Matériaux

Synthesis of Ferroelectric Oxides for Photovoltaic Applications

THÈSE dirigée par :

M.SLAOUI Abdelilah Directeur de recherche, ICube, CNRS-Université de Strasbourg

RAPPORTEURS :

M.EL MARSSI Mimoun Professeur, LPMC Université de Picardie Jules Verne, Amiens

Mme. BESLAND Marie-Paule Directrice de recherche, Institut des Matériaux Jean Rouxel, Nantes

---

AUTRES MEMBRES DU JURY :

Mme. VIART Nathalie Professeur, IPCMS, CNRS-Université de Strasbourg

---

MEMBRES INVITÉ :

M. DINIA Aziz : Professeur, IPCMS, CNRS-Université de Strasbourg

M. FIX Thomas Chargé de recherche, ICube, CNRS-Université de Strasbourg

M. REHSPRINGER Jean-Luc Directeur de recherche, IPCMS, CNRS-Université de Strasbourg

To my family

Aknowledgements

First I would like to thank my Thesis Director, Dr. Abdelilah Slaoui, for continual guidance and assistance throughout the duration of my Ph.D., and without whom this work would not have been possible. Even, its high support allowed my personal career growth by putting at disposal his work knowledge.

I would like to thanks the members of jury Mimoun El Marrsi, Marie-Paule Besland, Nathalie Viart, Aziz Dinia, Thomas Fix, Jean-Luc Rehspringer, not only for have made through Strasbourg even if the chaos of the recent events but even for their interest in my work and suggestions and corrections to this manuscript which increase the value of this work.

I should give particular thanks to the contributions to this work to my supervisor Dr.Thomas Fix. He made vital contributions to most of the work and gave me invaluable help on a totally new research topic for me. His patience and wise allowed me to growth familiar with the research environment and pushed me to the end of these three years.

Another special thanks should be given to Prof. jean-Luc Rehspringer , for his invaluable help on chemical processes and for having putting his experience on the work in order to make big steps in the work.

I should thank Professor Aziz Dinia, which allowed me to work independently in IPCMS, which collaboration allowed a huge breakthrough in the work.

Another special thank should go to Dr.Guy Schmerber, for his patience and understanding during my PhD project as well as willing to accomplish the work in very limited time laps. My PhD would have not be the same without his support.

A huge thanks to Cristophe Lefevre, which allowed me to work with him at the Synchrotron which allows a big step forward in this research project.

A big thanks will go to Damien Aureau and Mathieu Fregnaux for the XPS measurements that will put this work of 3 years under a new light; I would like to thank even Judith Driscoll which allowed a collaboration with the University of Cambridge where I have learnt more about the Kelvin Probe Force Microscopy.

A special thanks to the people who helped me during this work; in this sense I would like to thank Silviu Colis, Gilles Versini, Mircea Rastei, Bohdan Kundys, Daniel Stoeffler, Cristophe Lefevre, Cedric Leuvrey, Gérald Ferblantier, Dominique Muller, Sophie Barre and all the people who helped me during these 3 years.

A particular thought to Stephan Roques and Florian Mugler, which not only were always avaible for help but even with their sympathy made my life in the laboratory more easy and less stressing.

Eventually I would like to say a special thanks to the PhD and Post-Docs and Master's students who were with me in the laboratory especially I would like to thank Anatolie Graviluta, which is huge support and joyness during these 3 years.

I should eventually mention all my Italian friends I met in Strasbourg which made my life way more easy and funny. I have found special people which I will be in contact for long and tat will always will make me feel a little bit more home wherever I will go.

Alessandro Quattropani

Table of contents

Chapter 1.

Photovoltaics: an overview

During the last decade, humankind have undergone a strong energetic challenge since the technological advance and the high rate of development of emergent countries, such as China, India and Brazil, have followed a huge energy request. Consequently, a high energy demand at low cost are requested to satisfy the global needs. On the other hand, the scarcity of fossil fuels and the recent global weather changes pushed scientist to look forward to implement solutions of green energy production. Among the renewable energy options, photovoltaic energy, consisting in converting the sun radiation to electricity, has been intensively studied because of the large amount of energy received every day by our planet from the sun. In fact, in only one hour the sun irradiates the earth with a quantity of energy which would satisfy the global needs per years. The photovoltaic technologies advanced a lot since the discovery by Einstein[1] of the photoelectric effect and the first solar cells developed at Bell's laboratory in 1950. For many years the commercialized silicon panel were too expensive to compete with fossil fuels[2], thus the photovoltaic energy remains for years only exclusive for special applications such as energy generation for satellites or off-grid connected zones. In more recent years, thanks to research and advances in PV technologies and a large development of equipment and automation, a huge drop in costs occurred which make photovoltaics enough competitive with conventional energy production methods. This drop stimulated the research and development of the PV technology; it can be pointed out that in 2017, 98.9 GW of solar panels have been installed worldwide as compared to less than 20 GW in 2010. Fig.1.1 summarizes this large increment by plotting the installed solar capacity between 6 big groups worldwide. It is noticeable how the huge development nowadays is linked especially to the emergent markets in China, and more generally, in the Asian-Pacific countries (APAC).

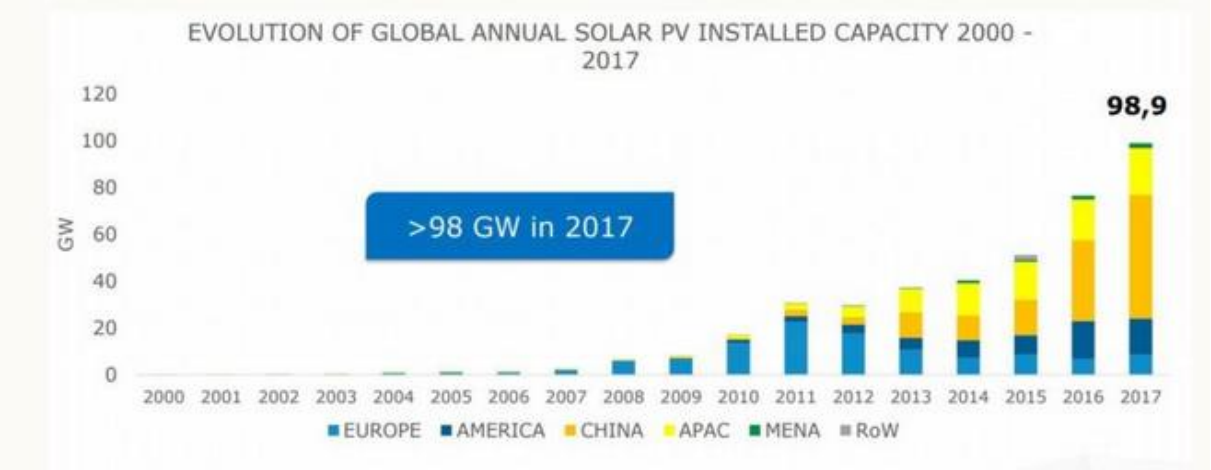

Fig.1.1. Worldwide solar panel energy installation from 2000 to 2017 [3]

1.1. Photovoltaics: principle

1.1.1. The solar spectrum

In order to introduce the solar cell devices, it is important to get familiar with the photovoltaic technology. The energy is provided by the sun, which behaves as a black body at 5800 K and its emission band is optimal at a wavelength of 500 nm. The average solar irradiation outside of the atmosphere has a power of 1366 W/m^2. When the solar radiation enters the atmosphere, it gets weighted by different factors: the different layers of the atmosphere, weather conditions well as the longitude and observation height. The gases which are composing the atmosphere (as Ozone (O_3), carbon dioxide (CO_2) and water vapour) absorbs the radiations close to their binding energy, so that the visible spectra presents some "features" as shown in fig.1.2. Solar irradiation varies at different position on earth so that a reference called "Air Mass" (AM) has been established in order to compare the different irradiation in different part of the globe. Two standards are defined for terrestrial use. The standard spectrum for space applications is referred to as AM0. It has an integrated power of 1366.1 W/m^2. The AM1.5 Global spectrum is designed for flat plate modules and has an integrated power of 1000 W/m^2 (100 mW/cm^2). The AM1.5 Direct (+circumsolar) spectrum is defined for solar concentrator work. It includes the direct beam from the sun plus the circumsolar component in a disk 2.5 degrees around the sun. The direct plus circumsolar spectrum has an integrated power density of 900 W/m^2.

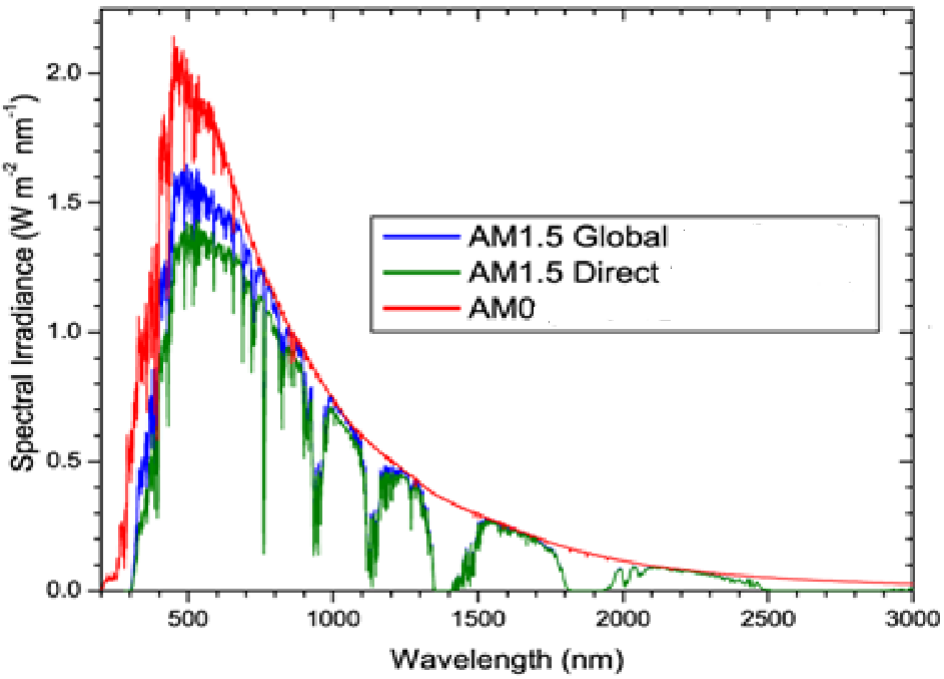

Fig.1.2. Solar Spectrum at different irradiation energy. Modified from[4]

1.1.2. The absorption of the sun light

Semiconductors present an energy gap between the valence and the conduction bands which varies typically between 0.3 to 3 eV. When a photon with an energy higher than the bandgap reaches the semiconductor it can be absorbed by the material and an electron can be promoted to the conduction band, leaving in the valence band a pseudo-charge of opposite sign, the hole.

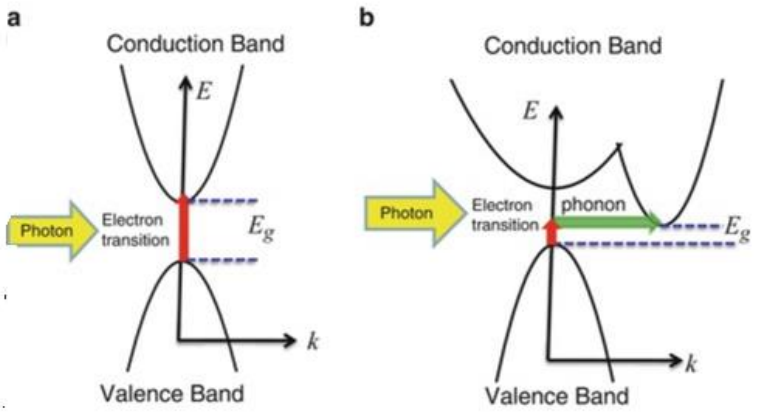

Fig.1.3. Direct (a) and indirect (b) transition bandgap

In fig.1.3 are presented two types of possible transition which depends on the nature of the bandgap. When the valence band maximum and conduction band minimum are coincident in the K-space, the material has a direct bandgap (fig.1.3.a); the transition is vertical and it is radiative: This is the case, for example, for GaAs, which find different applications in optoelectronics as well as solar cell for space applications. In the case of Silicon, instead, the bandgap is indirect: in this case the valence band maximum and conduction band minimum are not coincident in the K space and the electronic transition are not vertical, so non-radiative because they imply a change in the wave vector of the electron. In this case, in order for a photon to be absorbed, either it has sufficient energy to get promoted to a relative minimum (and then will relax in the absolute minimum by thermalization) or the transition will occur with the help of a phonon absorbed (or emitted) by the electron (fig.1.3.b).

1.1.2. The absorbing material

The solar cell device is based on an absorbing material which should be able to absorb the incident photons, create the hole-electron pairs as well as to separate them in order to collect them and consequently generate a current. Only few materials are able to strike as a solar cell absorber. The most important parameters for a solar cell needs are

- Concentrations of doping atoms; this can be of two types; donor atoms which donate free electrons, ND, or acceptor atoms, which accept electrons, NA. The concentrations determine the width of a space-charge region of a junction.
- Mobility μ, and diffusion coefficient, D, of charge carriers that characterize carriers transport due to drift and diffusion, respectively.
- Lifetime τ, and diffusion length, L, of the excess carriers that characterize the recombination-generation processes
- Bandgap energy, E_G, absorption coefficient, α, and refractive index, n, which characterize the ability of a semiconductor to absorb visible and other radiation

1.1.3. Photovoltaic Effect

Electron-hole separation is generally possible in solar cell devices thanks to a potential barrier present within the semi-conductor. The most common type of barrier are the homojunction (which is a p-n junction of the same semiconductor); heterojunction (p-n junction of two different materials) and Schottky barrier (metal/semiconductor). In the case of a silicon solar cell, the most used solution is a homojunction doped p and n, as shown in fig.1.4:

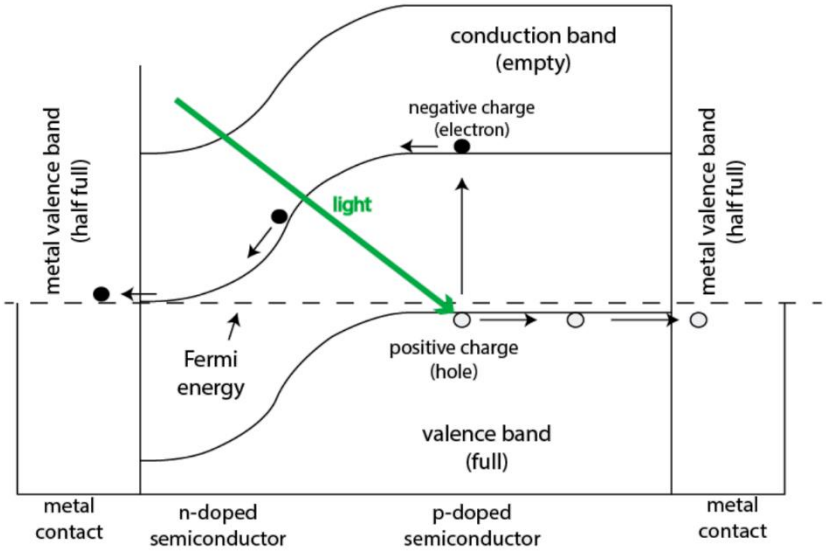

Fig.1.4. Band diagram of a p-n junction solar cell[5]

The generated photocarriers upon absorption and separation have a different behaviour that depends on the zone where they have been created:

- In the p or n zone, the minority carriers which reach the depletion zone are drifted from the electric field to the p-zone (the holes) and to the n-zone (the electrons) where they become majority carriers. A diffusion photo-current will be set into the system
- In the depletion zone, the electron-hole pair created by incident photons are dissociated by the electric field; the electrons move to the n zone and the holes to the p zone. In this case a generated photo-current is set.

These two currents give the total photocurrent I_{ph} which is proportional to the light intensity and it opposes to the diode current I_{obs} which comes from the polarization of the material. The resulting current will be:

$$I(V) = I_{ph} - I_{obs}(V) \qquad \text{(eq.1.1)}$$

For a ideal solar cell, equation 1.1 takes this form:

$$I(V) = I_{ph} - I_s(\exp(qV/kT) - 1) \qquad \text{(eq.1.2)}$$

where I_s is the saturation current of the diode; q the elemental charge; k the Boltzmann's constant and T the Temperature.

Under light, the solar cell characteristic of an ideal solar cell is the addition of a current of intensity I_{ph} and the characteristic of this diode in darkness. As a convention, the I/V curve is represented as the inversion of the current axis, so a typical Photovoltaic curve for a p-n junction based device looks like the curve in Figure 1.5:

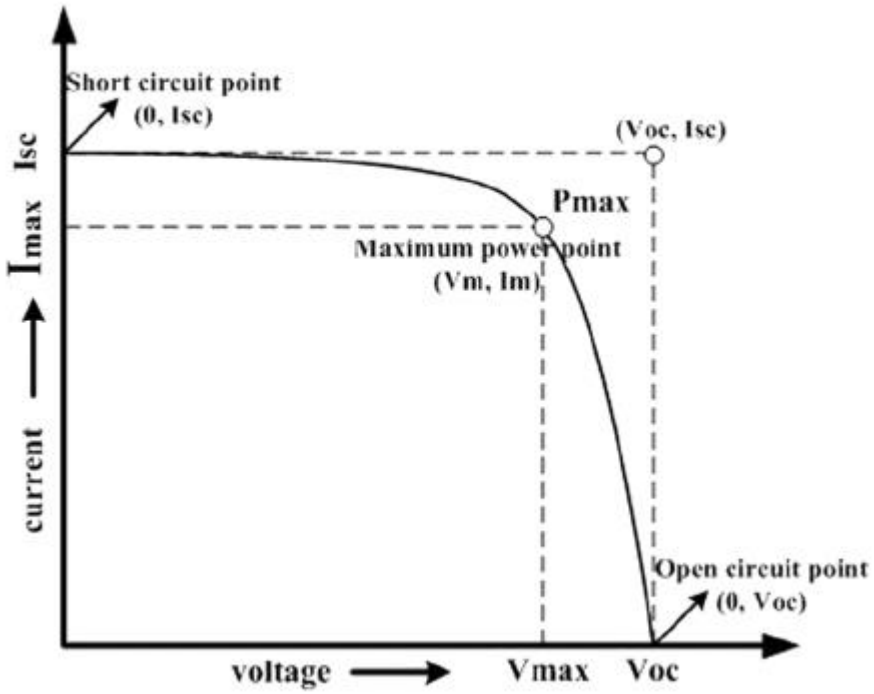

Fig.1.5. Conventional representation of a photovoltaic I-V curve for a p-n junction based device[6]

The important factors in the I-V curve are:

- I_{sc}: the short-circuit current (obtained for V=0) is the current due to the generation and collection of light-generated carriers. For an ideal solar cell at most moderate resistive loss mechanisms, the short-circuit current and the light-generated current are identical. Therefore, the short-circuit current is the largest current which may be drawn from the solar cell.
- V_{oc}: the open-circuit current (obtained for I=0) is the maximum voltage available from a solar cell. The open-circuit voltage corresponds to the amount of forward bias on the solar cell due to the bias junction with the light-generated current.
- I_m: the current obtained at the maximum power of the solar cell;
- V_m: the voltage obtained at the maximum power of the solar cell.

- The Fill Factor (FF): is the parameter which allows the determination of the efficiency of the solar cell together with the V_{oc} and I_{sc}. Graphically, the FF is a measure of the "squareness" of the solar cell and is also the area of the largest rectangle which will fit in the IV curve. The FF is the square represented in fig. 1.X and can be calculated as :

$$FF= (V_m I_m)/(V_{oc} I_{sc}) \quad \text{(eq.1.3)}$$

- The solar cell efficiency (η) which can be expressed as:

η= (maximum electrical power)/ (incident Solar power):

$$\eta= (V_m I_m)/\phi_i = (FF\ V_{oc} I_{sc})/\ \phi_s \quad \text{(eq.1.4)}$$

where ϕ_i it's the light flux received by the solar cell for a given surface; These parameters vary with the light intensity, so the convention is to use standard conditions at AM 1.5 at a T=25 °C.

1.1.4. Efficiency limiting factors

The photons conversion is not perfect, there are several factors which limits the efficiency of the solar cell. These losses can be classified in two types: 1) losses due to the material; 2) losses due to the technology used.

a) Losses attributed to the material properties:

The main losses in a silicon based solar cell as an example are shown in fig.1.6. The green part is that of the solar spectra effectively used by Silicon for electron-hole conversion. Photons with a wavelength higher than the one of the bandgap ($\lambda>\lambda_g$) do not have enough energy to promote an electron from the valence band to the conduction band and it is therefore lost (red part of the spectra in fig.1.6). On the other hand, the photons with an energy higher than the one of the bandgap (purple and blue in the spectra) give rise to only one electron-hole pair and the rest of the energy is lost as heat (thermalization).

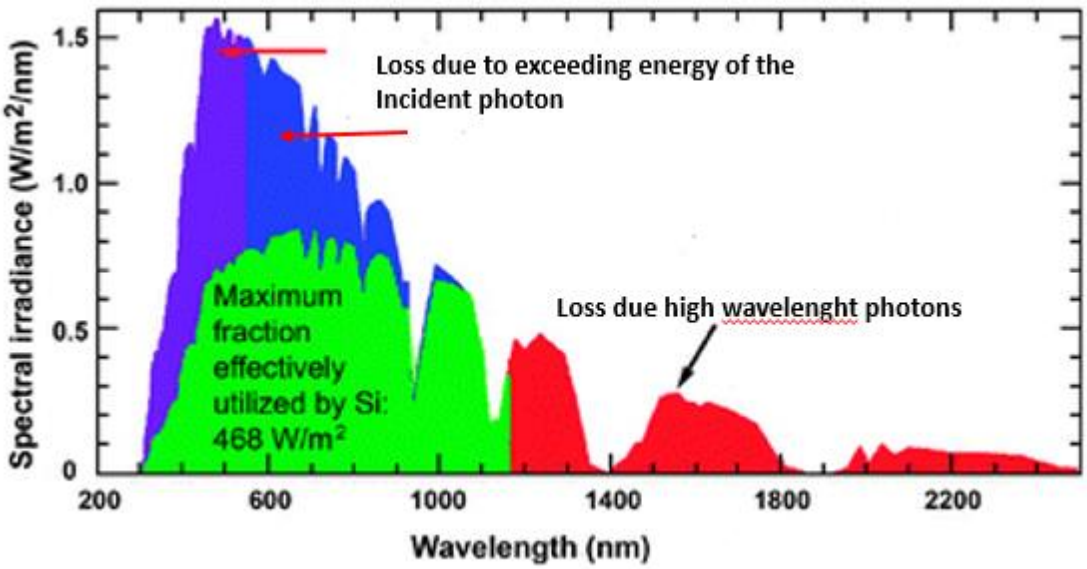

Fig.1.6. Solar Spectrum and loss into a Si based solar cell device[4]

Other losses are due to a non-perfect Fill Factor. As seen above, the I-V curve depends on the Boltzmann equation under an exponential form (exp (qV/kT) -1); the curve has not a rectangular shape and it is not higher than 0.89 in the best cases. These effect are due to a not perfect p-n junction, the resistance.

b) Losses attributed to the device fabrication:

One important loss in a silicon solar cell is the optical reflection. In fact, the refractive index of Silicon is different from the ones of the air so that at the interface air/Silicon some reflection would low the number of photons which reaches the absorbing material; another optical loss is the shadow effect due to metallic contacts that reflect the impinging sun light.

Finally, the absorption efficiency is important, especially for thin films (<100 μm) because a fraction of the photons which have enough energy get across the cell without being absorbed; the efficiency of collection is instead linked to the number of carriers generated and the ones which are finally collected. These are related to the number of carriers which recombines before being collected and depends on the lifetime of minority carriers (average time between the generation and recombination of a minority carrier).

1.1.5. The Shockley-Queisser Limit

The simple solar cell is based on the PN junction concept. Shockley and Queisser[7] were the first to develop a model which took into consideration a single-junction solar cell, in order to

establish the maximum theoretical efficiency of an ideal device. To do so, they started from some hypothesis:

- The sun behaves like a black body at a T=6000K;
- The solar cell behaves like a black body at T=300 K;
- The solar cell absorbs all the photons with an energy higher than its bandgap;
- Each absorbed photon generates an electron-hole pair which gets immediately dissociated at a rate of 100%;
- The recombination is only radiative;
- Each not recombined charge carrier is efficiently collected.

Using this model, the number of electrons generated in a solar cell is equal to the number of photons with an energy higher than the bandgap of the material minus the number of photons emitted by radiative recombination. In this way it is possible to calculate the maximum efficiency of a solar cell, which is 33.7% for a bandgap of 1.34 eV while it is 31% for the Silicon with a bandgap of 1,12eV, In fig.1.7 are shown (a) the curve calculated by Shockley and Queisser in their article (considering the sun as a black body at 6000 K) and (b) the one modified for a realistic solar spectrum.

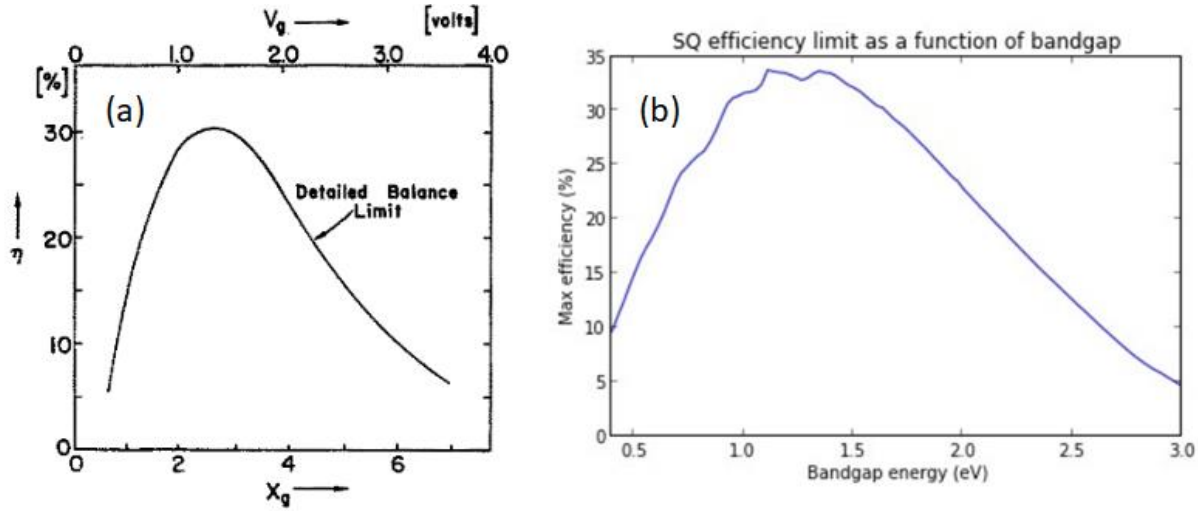

1.7. a) curve calculated by Shockley and Queisser in their article[7] (considering the sun a 6000 K) and (b) curve modified for a realistic solar spectrum[8].

1.2. Materials for Photovoltaic

Fig. 1.8 gives a generic view of the present photovoltaic device technologies based on the primary active materials. The established technologies are wafer-based solar cells (crystalline silicon and III-V compounds) or thin films (a-Silicon and Chalcogenides). Also represented are the emerging solar cells technologies such as those based on organic (polymers, small molecules), on hybrid materials (DSSC, perovskite) or using nanomaterials (dots, wires…).

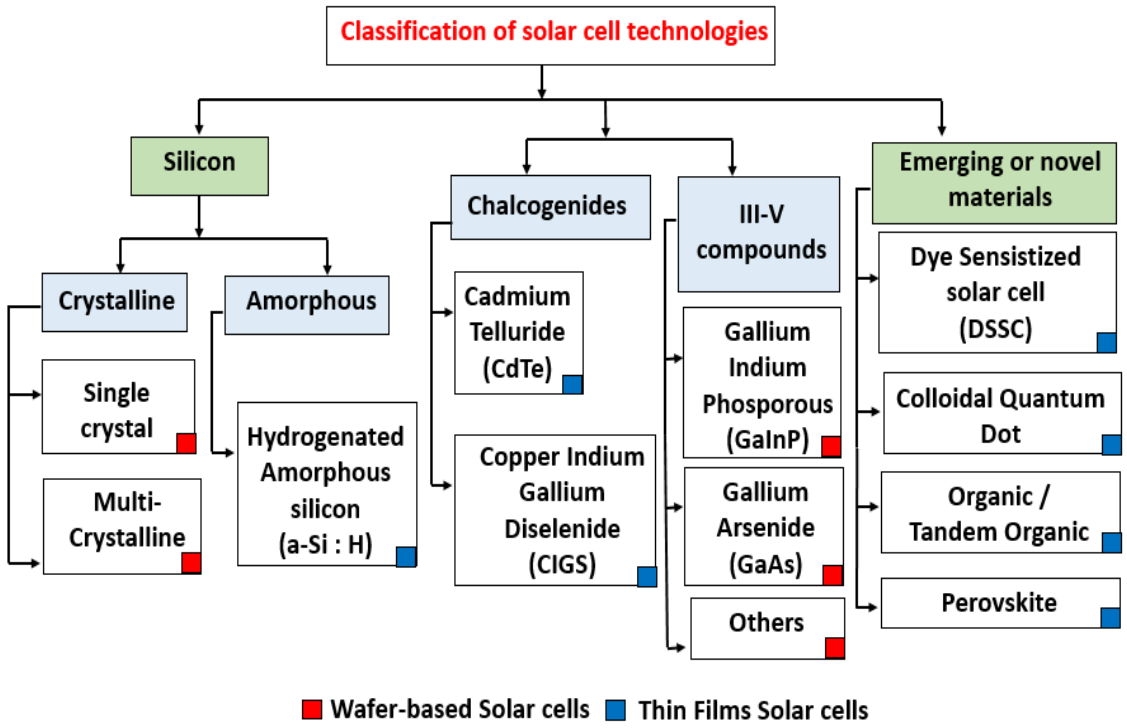

Fig.1.8. Solar cells classification based on the active material. Modified from[9]

1.2.1. Solar cells Technologies: state of the art

Figure 1.9 shows the graph established by the National Renewable Energy Laboratory (NREL) that summarizes the highest efficiencies reported since 1975. Several technologies and materials are employed to make solar cells. Let's consider first the single junction (one semiconductor) solar cells structures.

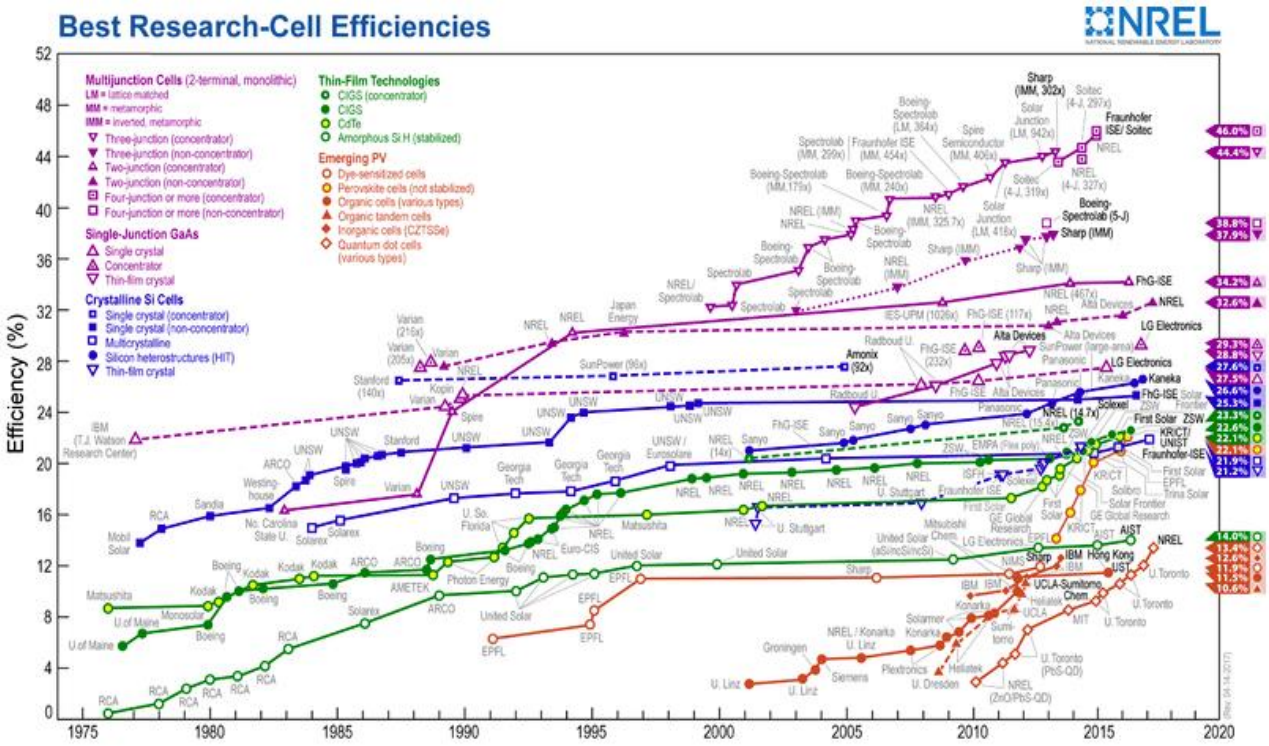

Fig.1.9.Highest efficiencies devices reported from 1975 till now[10]

Figure 1.10.a shows a schematic of a conventional solar cell structure based on single-crystalline or multicrystalline silicon wafers, 150 to 250 μm thick. The structure exhibits a conventional P-N homojunction where P region is a boron-doped silicon substrate and the N region is a phosphorous-doped silicon emitter. The backside contact is a screen printed Aluminium layer while the front contact is silver based screen printed through a mask. This structure is the most used to make modules and represents about 90% of the market share.

Fig. 1.10.b displays the schematic of an amorphous silicon based solar cell. In this case, the absorbing layer is an intrinsic amorphous silicon layer of about 1-2 μm thick, sandwiched between very thin (few nanometres) n and a p doped regions. The front contact is a transparent conducting oxide or TCO (in this case SnO_2) and the back contact is an Al film. The whole structure is deposited on a glass serving as a substrate and as a window for solar radiation.

Fig.1.10.c it is a schematic of a solar cell based on Cadmium Telluride (CdTe) which has experimented a huge increase of the market share and have surpassed a-Si technologies in thin films photovoltaic market thanks to their high quantum efficiencies. This structure uses a heterojunction with a n-type semiconductor which is CdS and a p-type one which is CdTe.

Similar structures to CdTe Cell but not represented here is that using inorganic compound CIGS (copper-Indium-Gallium-diSelenide) as the absorbing material which has achieved solar efficiencies well above 20%[11]. The challenge to create solar cells materials with earth-abundant and non-toxic elements pushed to the development of copper-zinc-tin-sulphide (CZTS) thin film compounds. CZTS is a quaternary compound with a direct bandgap of 1.5 eV and a large absorption[12] . Yet, the highest efficiency of these CZTS cells was found to be 12.6% in laboratory[13]. The main drawback of the CIGS and CZTS cells is the synthesis of the layers with the appropriate stoichiometry and free of secondary phases which often leads to inhomogeneous films and recombination centres

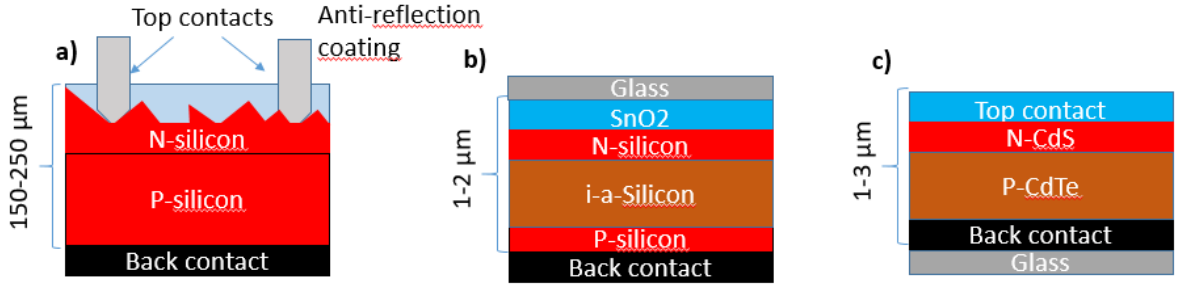

Fig.1.10. Schematic of (a) a conventional silicon solar cell; (b) an amorphous silicon solar cell, (c) a CdS-CdTe solar cell[9]

Among other cell structures, GaAs based solar cells are established since a decade. This III-V material is well suited for photovoltaic applications as the electrons move faster within this semiconductor as compared to Silicon; moreover, it forms a single junction III-V semiconductor which is well suited in terms of absorption, non-radiative energy loss, minority carrier lifetime and mobility. However, the high fabrication cost of these cells did not allow a large implementation in the market despite an efficiency of 28.8% as a cell and 24.1% in modules. Table 1.1 highlights the established PV technologies and the corresponding maximum efficiencies for the upper mentioned structures.

Solar cell	Maximum PCE	References
c-Si	26.6%	Yoshikawa et al.[14]
a-Si	13.4% (multijunction)	LG solar
CdTe	21%(lab)/17.5%(module)	First Solar
CIGS	20.3%	Jackson et.al.[15]
GaAs	28.8%(lab)/24.4%(module)	Matsubara et al.[16]
CZTSSe	12.6%	Wang et al. [13]

Table 1.1. Established technology solar cells and their maximum reported efficiencies

Figure 1.9 shows also that new type of solar cells has emerged more recently. Among them, organic photovoltaics using semiconductor polymers or small molecules as absorbing materials. The main advantages are low temperature deposition, the use of coating methods, printable on several substrates as well as low weight Finally, the tandem organic solar cells were investigated to increase the 11% record efficiency of the single-junction one, and thus it was possible by using an interconnection layer to reach 12.5% efficiency in 2016[17]. Another important advantage of these solar cells is that the dye have a very high absorption coefficient[18,19] which can allow even to few nanometres to absorb enough light to reach a high efficiency, although they shows a low dielectric constant. Several works have addressed Bulk Heterojunction Solar cells (BHJ) and DSSC[20–25] structures and an efficiency of 12.9% has been achieved with DSSC[26] and 8% for BHJ[27]. Liquid junction QDSC using quantum dots has instead improved till 5% while a 7% efficiency has been reported for a solid state one [22,23] until development of a very recent colloidal quantum dots which showed a 13.4% efficiency[28]. One important problem of these cells is related to the stability of the absorber material, which should be overcome to widespread these cells in the market.

Recently, a new class of material which involves organic and inorganic Perovskites got renewed interest among researchers. As it will be further discussed in the next chapter, Perovskites are compounds with formula ABX_3, where A and B are two cations (normally A has a larger ionic radii than B) and X is an anion, and they have shown an unprecedented increase in efficiency from 3% reported in 2009 [29] to more than 22% this year[10,30,31], which is

comparable with the ones of CdTe and CIGS. What really strikes out in these cells is the large diffusion length and high mobility paired with a low recombination rate at surface and at the grain boundaries. Fig.1.11. displays a schematic of a typical organic-inorganic perovskite cell device.

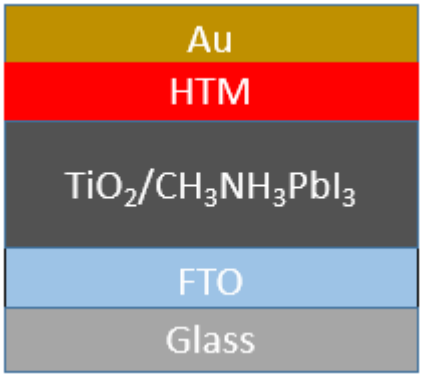

Fig.1.11. Schematic representation of an Organic-Inorganic perovskite solar cell

The results obtained for these devices are promising. However, several questions have to be answered before such cells penetrate the PV market. Firstly, the toxicity and environmentally dangerous lead can be detrimental for a wide use of the devices. Many researchers respond to this issue saying that the presence of lead is pretty small compared to other commonly used devices (i.e. cars batteries) and therefore this should not be a limiting factor. Secondly, the stability of the hybrid perovskites (as well as the organic compounds for Organic solar cells) is still a questionable point. Recent studies have pointed out the possible large stability of the material. Finally, the manufacturing steps of these cells are still mainly at the laboratory level, and it is far from an industrial pathway when compared to the other technologies.

The table 1.2. summarises the devices based on alternative PV technologies and their maximum reported efficiencies.

As reported in figure 1.8 (NREL chart above), multijunctions solar cells based on III-V materials for ultra-high efficiencies were also developed since many years. In theory, such devices formed by stacking 2 or more III-V semiconductors of different bandgaps can reach an optimal efficiency of about 60% under sun concentration. In practice, multjunctions solar cells with an efficiency approaching 46% has been reported from Fraunhofer Institute for Solar Energy Systems ISE, Germany However, the cell cost increases with increasing the number of

junctions so they have found applications mainly in space power generation or under sun radiation concentration higher than 1000.

Solar cell	Maximum PCE	References
DSSC	12.6%	Ren et al.[32]
Perovskite	22.1%	Yang et al.[33]
Organic	11.2%	Mori et al.[34]
Organic Tandem	12.50%	Li et al.[17]
Quantum Dots	13.4%	Sanehira et al.[28]

Table 1.2. Alternative solar cells technologies and their maximum reported efficiencies

Based on this short review of PV technologies and on data of figure 1.8 (NREL), It can be pointed out that there were continuous investigations over years either (i) by continuously improving the existing technologies by reducing the losses (optical and electrical) or by developing new cell architectures (PERC, PERT, Bifacial, HTJ…), or (ii) by proposing new absorbing semiconductors (organics, hybrids, QDs…) but still using the "junction" concept for charge carriers' separation.

This thesis' work is aiming at pursuing option (ii) and proposing inorganic perovskite oxides (POs) as absorbing material but with a completely different concept for charges separation and transport, thanks to the ferroelectric character of these POs.

1.2. Oxides materials for Photovoltaics

Oxide materials offers a wide range of different possible applications in electronics, memory, magnetoelectronics and even bioprocessing[35–38]. More recently, Oxides for photovoltaic is arising interest for their peculiar characteristics. In particular, Metal Oxides (MO) seems adequate to offer an alternative to the present photovoltaic structures, thanks to their chemical stability and non-toxicity and also easy fabrication. The most known MOs for photovoltaics are the transparent conducting oxides (TCO) which are already widely used in

several solar cell structures as front or bottom electrodes thanks to their specific properties (bandgap, work function, carrier mobility and resistivity) which allows an appropriate choice to build a device. The most common MOs are ITO, FTO, ZnO, AZO, SnOx[35]. For example, in CdTe- based solar cells, SnO_2 or ITO are frequently used as TCOs depending on the deposition temperature of the n-layer CdS. In case of lower temperatures used, FTO is used because of its better ratio between optical transmittance and sheet resistance. In most of the cases, the choice of the TCO is related to its work function which better matches the solar cell needs.

As for the MOs as solar absorbers, there are specific requirements that should be fulfilled: an oxide material with a bandgap compatible with the solar spectra as well as a high carriers' diffusion length within the material. Among potential PV oxide materials, Cu_2O was the most investigated since 1970 .[39,40] This oxide has a bandgap of 2.1 eV. It is expected that a solar cell based on materials with such a high bandgap can reach a theoretical maximum efficiency of around 23% under AM 1.5 illumination, which is quite reasonable. In practice the best solar cells based on Cu_2O have reached 6%[41] because of the difficulties in synthesizing very good material free of parasitic phases [42].Therefore, such material can rather be envisaged as a high bandgap material for applications in multijunctions consisting in a stack of three or more junction. Furthermore it can find applications in semi-transparent PV solar cells.

CuO (Cupric Oxide) has been also investigated as a photovoltaic absorber. This is an intrinsic p-type semiconductor because of the Cu vacancies which forms spontaneously. Its bandgap varies between 1.2 and 1.8 even if there are some controversy about whether it is a direct or indirect[43–46] bandgap. Despite its low bandgap, only cells with 0.1% efficiency have been reported in 2011 for CuO nanowires grown from a Cu foil with thermal oxidation and covered with a solution processed n-type ZnO[47], while a 0.25% efficiency was published in 2016 for heterojunction structure of glass/ITO/CuO/ZnMgO/Ag [48]. In addition to these Cu based oxides, few others MOs such as Bi_2O_3, Pb_xO_y [49], Co_3O_4 and Fe_2O_3 [42] were investigated as absorbers, but none of them was able to achieve striking efficiencies.

Within the family of functional metal oxides, Ferroelectric (FEOs) oxides are gaining more attention from the scientific community because of their peculiar characteristics that can be fitting the solar cells requirements. Moreover, it has been theoretically and experimentally shown that it is possible to overcome the Shockley-Queisser limit [50] which is opening the door for a possible higher efficiency-single layer solar cell. Different Ferroelectric oxide compounds

have been investigated in recent years such as $BiFeO_3$ (BFO), $BiMnO_3$ (BMO), $BaTiO_3$ (BTO), $LiNbO_3$ (LNO), $Pb(Zr,Ti)O_3$ (PZT) and Bi_2FeCrO_6 (BFCO).

One of the main problem for FEOs absorbers is the high bandgap found for most of these materials. As discussed earlier, an optimal gap of 1.34 eV is the target for an optimal matching with the solar spectra and to approach a high efficiency device. Bismuth Ferrite based oxide, one of the most studied material for Ferroelectric solar cell, shows instead a gap of 2.7 eV. The mechanism will be further discussed in chapter 2 but the low light absorption did not allow BFO based device to overcome 10% efficiency (fig.1.12).

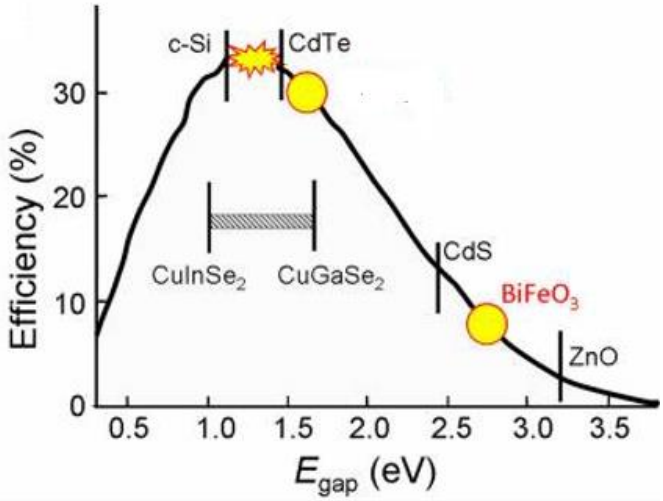

Figure 1.12. Bandgap and relative device's efficiency for solar cells[51]

In Fig.1.13 are reported some of the Inorganic oxide compounds by their bandgap and consequently the expected solar cell-based efficiencies according to SQ limit. The ferroelectric oxides exhibit a strong potential as materials to match the solar spectrum absorption. The recent efficiencies BMO/BMn_2O_5 come from the possibility to tune the bandgap. The same was done by introducing a controlled amount of Cr within the structure of BFO; this allowed Nechache et al.[52] to fabricate for he first time a solar cell with a remarkable 8.1% efficiency. Yet, there are several questions (growth models, order vs disorder, photovoltaic versus ferroelectricity ...) and hopefully solutions which open the route for developing a new type of solar cell that could potentially compete with conventional PV technologies. The present

thesis work is intending to contribute to master the synthesis of BFCO films, to get a deep insight on the carriers transport within such oxides and finally to design a FEO solar cell structure with appropriate electrodes for extracting the carriers under sun illumination.

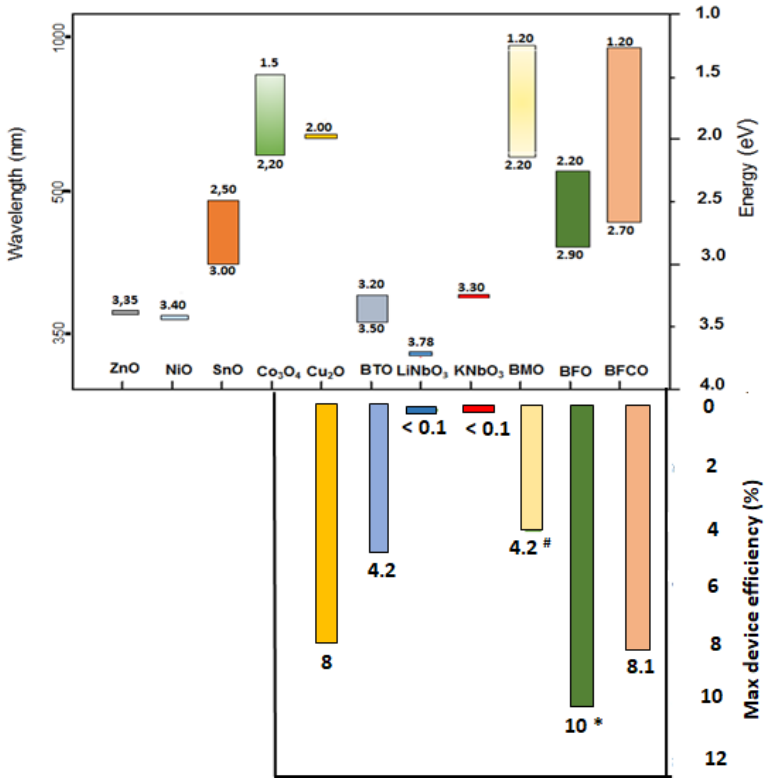

*illuminated by a bandgap wavelength diode

#BMO/BMn_2O_5 device

Figure 1.13. Bandgap of some metal oxides used in Photovoltaic Devices and reported maximum efficiency of the device

1.3.Summary

In this chapter, we first reported briefly on the principle of photovoltaic effect and discussed some basic principles. Then we presented an overview of the present photovoltaic materials and technologies, ranging from silicon based solar cells to thin films. The best efficiencies as recorded in literature are given and some technical and/or ecological limitations are given. Finally, the metal oxides for photovoltaics were introduced. The potential of ferroelectric oxides as absorbing materials for solar cells was discussed.

The next chapter will focus more deeply on the properties of the perovskite oxide and their potential for photovoltaics conversion.

References of Chapter 1:

1. Green, M. A. *Solar cells: operating principles, technology and system applications*. (Univ. of New South Wales, 1998).
2. Shah, A. Photovoltaic Technology: The Case for Thin-Film Solar Cells. *Science* **285,** 692–698 (1999).

3. Future Energy. (2018). Available at: https://futurenergyweb.es/en/solar-grows-by-30-in-2017-with-demand-set-to-rise-over-next-5-years/.
4. PVeducation. (2018). Available at: https://pveducation.org/.
5. *Solar cells and their applications*. (Wiley, 2010).
6. Bana, S. & Saini, R. P. A mathematical modeling framework to evaluate the performance of single diode and double diode based SPV systems. *Energy Rep.* **2,** 171–187 (2016).
7. Shockley, W. & Queisser, H. J. Detailed Balance Limit of Efficiency of *p-n* Junction Solar Cells. *J. Appl. Phys.* **32,** 510–519 (1961).
8. Byrnes, S. The Shockley-Queisser Limit and its Discontents. (2015). Available at: http://sjbyrnes.com/shockley_queisser_talk.pdf. (Accessed: 25th September 2018)
9. Ibn-Mohammed, T. *et al.* Perovskite solar cells: An integrated hybrid lifecycle assessment and review in comparison with other photovoltaic technologies. *Renew. Sustain. Energy Rev.* **80,** 1321–1344 (2017).
10. NREL best efficiency. (2018). Available at: https://www.nrel.gov/pv/. (Accessed: 28th June 2018)
11. Jackson, P. *et al.* Properties of Cu(In,Ga)Se $_2$ solar cells with new record efficiencies up to 21.7%: Properties of Cu(In,Ga)Se $_2$ solar cells with new record efficiencies up to 21.7%. *Phys. Status Solidi RRL - Rapid Res. Lett.* **9,** 28–31 (2015).
12. Shin, B. *et al.* Thin film solar cell with 8.4% power conversion efficiency using an earth-abundant Cu $_2$ ZnSnS $_4$ absorber: Cu $_2$ ZnSnS $_4$ solar cell with 8.4% efficiency. *Prog. Photovolt. Res. Appl.* **21,** 72–76 (2013).
13. Wang, W. *et al.* Device Characteristics of CZTSSe Thin-Film Solar Cells with 12.6% Efficiency. *Adv. Energy Mater.* **4,** 1301465 (2014).
14. Yoshikawa, K. *et al.* Silicon heterojunction solar cell with interdigitated back contacts for a photoconversion efficiency over 26%. *Nat. Energy* **2,** 17032 (2017).
15. Jackson, P. *et al.* New world record efficiency for Cu(In,Ga)Se2 thin-film solar cells beyond 20%. *Prog. Photovolt. Res. Appl.* **19,** 894–897 (2011).
16. Matsubara, H., Tanabe, T., Moto, A., Mine, Y. & Takagishi, S. Over 27% efficiency GaAs/InGaAs mechanically stacked solar cell. *Sol. Energy Mater. Sol. Cells* **50,** 177–184 (1998).
17. Li, M. *et al.* Solution-processed organic tandem solar cells with power conversion efficiencies >12%. *Nat. Photonics* **11,** 85–90 (2017).
18. Gresser, R., Hummert, M., Hartmann, H., Leo, K. & Riede, M. Synthesis and Characterization of Near-Infrared Absorbing Benzannulated Aza-BODIPY Dyes. *Chem. - Eur. J.* **17,** 2939–2947 (2011).
19. Kraner, S. *et al.* Influence of side groups on the performance of infrared absorbing aza-BODIPY organic solar cells: Performance of IR absorbing aza-BODIPY organic solar cells. *Phys. Status Solidi A* **212,** 2747–2753 (2015).
20. Bisquert, J. *Nanostructured energy devices: foundations of carrier transport*. (CRC Press, Taylor & Francis Group, 2018).
21. Li, C., Liu, M., Pschirer, N. G., Baumgarten, M. & Müllen, K. Polyphenylene-Based Materials for Organic Photovoltaics. *Chem. Rev.* **110,** 6817–6855 (2010).
22. Clarke, T. M. & Durrant, J. R. Charge Photogeneration in Organic Solar Cells. *Chem. Rev.* **110,** 6736–6767 (2010).
23. Hains, A. W., Liang, Z., Woodhouse, M. A. & Gregg, B. A. Molecular Semiconductors in Organic Photovoltaic Cells. *Chem. Rev.* **110,** 6689–6735 (2010).

24. Chu, T.-Y. *et al.* Bulk Heterojunction Solar Cells Using Thieno[3,4- *c*]pyrrole-4,6-dione and Dithieno[3,2- *b* :2′,3′- *d*]silole Copolymer with a Power Conversion Efficiency of 7.3%. *J. Am. Chem. Soc.* **133,** 4250–4253 (2011).
25. Peter, L. M. The Grätzel Cell: Where Next? *J. Phys. Chem. Lett.* **2,** 1861–1867 (2011).
26. Yella, A. *et al.* Porphyrin-Sensitized Solar Cells with Cobalt (II/III)-Based Redox Electrolyte Exceed 12 Percent Efficiency. *Science* **334,** 629–634 (2011).
27. He, F. & Yu, L. How Far Can Polymer Solar Cells Go? In Need of a Synergistic Approach. *J. Phys. Chem. Lett.* **2,** 3102–3113 (2011).
28. Sanehira, E. M. *et al.* Enhanced mobility $CsPbI_3$ quantum dot arrays for record-efficiency, high-voltage photovoltaic cells. *Sci. Adv.* **3,** eaao4204 (2017).
29. Kojima, A., Teshima, K., Shirai, Y. & Miyasaka, T. Organometal Halide Perovskites as Visible-Light Sensitizers for Photovoltaic Cells. *J. Am. Chem. Soc.* **131,** 6050–6051 (2009).
30. Liu, M., Johnston, M. B. & Snaith, H. J. Efficient planar heterojunction perovskite solar cells by vapour deposition. *Nature* **501,** 395–398 (2013).
31. Jeon, N. J. *et al.* Compositional engineering of perovskite materials for high-performance solar cells. *Nature* **517,** 476–480 (2015).
32. Ren, Y. *et al.* A Stable Blue Photosensitizer for Color Palette of Dye-Sensitized Solar Cells Reaching 12.6% Efficiency. *J. Am. Chem. Soc.* **140,** 2405–2408 (2018).
33. Yang, W. S. *et al.* Iodide management in formamidinium-lead-halide–based perovskite layers for efficient solar cells. *Science* **356,** 1376–1379 (2017).
34. Mori, S. *et al.* Organic photovoltaic module development with inverted device structure. *MRS Proc.* **1737,** (2015).
35. Lorenz, M. *et al.* The 2016 oxide electronic materials and oxide interfaces roadmap. *J. Phys. Appl. Phys.* **49,** 433001 (2016).
36. Chen, Y. Z. *et al.* A high-mobility two-dimensional electron gas at the spinel/perovskite interface of γ-Al2O3/SrTiO3. *Nat. Commun.* **4,** 1371 (2013).
37. Xu, X., Randorn, C., Efstathiou, P. & Irvine, J. T. S. A red metallic oxide photocatalyst. *Nat. Mater.* **11,** 595–598 (2012).
38. Padmavathy, N. & Vijayaraghavan, R. Enhanced bioactivity of ZnO nanoparticles—an antimicrobial study. *Sci. Technol. Adv. Mater.* **9,** 035004 (2008).
39. Iwanowski, R. J. & Trivich†dr, D. Enhancement of the photovoltaic conversion efficiency in Cu/Cu2O schottky barrier solar cells by H+ ion irradiation. *Phys. Status Solidi A* **95,** 735–741 (1986).
40. Herion, J., Niekisch, E. A. & Scharl, G. Investigation of metal oxide/cuprous oxide heterojunction solar cells. *Sol. Energy Mater.* **4,** 101–112 (1980).
41. Minami, T., Nishi, Y. & Miyata, T. Heterojunction solar cell with 6% efficiency based on an n-type aluminum–gallium–oxide thin film and p-type sodium-doped Cu_2O sheet. *Appl. Phys. Express* **8,** 022301 (2015).
42. Rühle, S. *et al.* All-Oxide Photovoltaics. *J. Phys. Chem. Lett.* **3,** 3755–3764 (2012).
43. Koffyberg, F. P. & Benko, F. A. A photoelectrochemical determination of the position of the conduction and valence band edges of *p* -type CuO. *J. Appl. Phys.* **53,** 1173–1177 (1982).
44. Hong, M.-J., Lin, Y.-C., Chao, L.-C., Lin, P.-H. & Huang, B.-R. Cupric and cuprous oxide by reactive ion beam sputter deposition and the photosensing properties of cupric oxide metal–semiconductor–metal Schottky photodiodes. *Appl. Surf. Sci.* **346,** 18–23 (2015).

45. Ray, S. C. Preparation of copper oxide thin film by the sol–gel-like dip technique and study of their structural and optical properties. *Sol. Energy Mater. Sol. Cells* **68,** 307–312 (2001).
46. Dimopoulos, T. *et al.* Photovoltaic properties of thin film heterojunctions with cupric oxide absorber. *J. Renew. Sustain. Energy* **5,** 011205 (2013).
47. Wang, P., Zhao, X. & Li, B. ZnO-coated CuO nanowire arrays: fabrications, optoelectronic properties, and photovoltaic applications. *Opt. Express* **19,** 11271 (2011).
48. Bhardwaj, R., Barman, R. & Kaur, D. Improved photovoltaic effect in CuO/Zn1−xMgxO heterojunction solar cell by pulsed laser deposition. *Mater. Lett.* **185,** 230–234 (2016).
49. Lira-Cantu, M. *The Future of Semiconductor Oxides in Next-Generation Solar Cells*. (2017).
50. Spanier, J. E. *et al.* Power conversion efficiency exceeding the Shockley–Queisser limit in a ferroelectric insulator. *Nat. Photonics* **10,** 611–616 (2016).
51. Zhang, J. *et al.* Enlarging photovoltaic effect: combination of classic photoelectric and ferroelectric photovoltaic effects. *Sci. Rep.* **3,** (2013).
52. Nechache, R. *et al.* Bandgap tuning of multiferroic oxide solar cells. *Nat.Photonics* **9**, 61-67 (2014)

Chapter 2.

Perovskite oxide based devices

There are several types of oxide materials that differentiates often by the number of cations, which results in different structures and compositions. The most typical structure of complex or mixed oxides consists simply in two or more different cations with different oxidation states, ionic radii and coordination numbers. This diversity creates a large variety of complex structures which reflects on different properties of these oxides. Among the most known structures are the spinel structures (AB_2O_4) which are well considered for their magnetic properties. In the most typical case, the A site is a six-folded coordinated ion while a sixfold-coordinate cation occupies the B-site. Eventually, in the most complex cases, a mixing of ion and cation in the A and B site occurs. For this reason, these materials result in a large variety of complex structures and different properties. In this chapter, we will report on oxide compounds, especially those with perovskite crystallographic structure, looking to their characteristics and how they can find application in photovoltaics.

2.1. Structure of perovskite oxides

Perovskites are a family of materials with typical chemical composition ABO_3 where A and B are two different cations. They were named so after the discovery of the first crystal, $CaTiO_3$, in Ural Mountains in Russia. The chemical composition is similar to that of the ilmenite: in the ilmenites the A and B atoms are approximately of the same size (e.g. $LiSbO_3$) and occupy the octahedral site. Yet, ilmenites have different structures as compared to the perovskite ones. The family of Perovskites evolves a large number of structures. A typical structure consists in a large cation on the A site that is 12 coordinate and a smaller 6 coordinated ion on the B site.

As shown in figure 2.1, the ideal perovskite is a cubic lattice. However, due to different atoms that can take part in the structure, most of the perovskite compounds are distorted and presents a lower symmetry (e.g. orthorhombic or hexagonal), or just a slight distortion from the perfect cubic lattice.

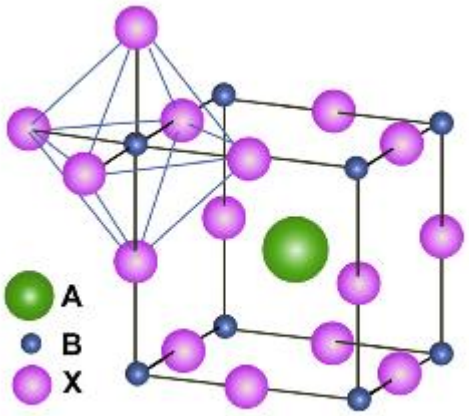

.

FIG.2.1. Simple cubic double perovskite with general formula ABX_3, A is the cation surrounded by a network of corner-sharing BX_6 octahedra[1]

The deviation from the ideal structure is estimated through a factor of tolerance *t* which is taken out from the perovskite oxide ABO_3 regarded as a purely ionic. In this way, the relation between the radii of the A atom, the B atom and the Oxygen is:

$$r_A+r_O=\sqrt{2}\,(r_B+r_O) \quad \text{(eq. 2.1)}$$

It is then possible to express the deviation from the ideal cubic structure by t_{IR} [2]:

$$t_{IR}=(r_A+r_O)/\sqrt{2}(r_B+r_O) \quad \text{(eq.2.2)}$$

The tolerance factor for maintaining a perovskite structure should be between 0.80 and 1.10. For smaller or larger *t*, the same compound would turn to the ilmenite structure.

In fig.2.2 are shown all the chemical elements which can form a perovskite structure. As can be seen, most of the elements, except the noble gases and few others, can form a perovskite. The stability of these structures relies not only on the ratio between the A and the B atoms but even on their nature. In fact, for the B atom, the bonds are highly covalent. In this sense, is not surprising that an oxide such as $BaGeO_3$ does not fit the perovskite structure in ambient condition, as the preferred coordination number for Ge is 4. An alternative is to form a perovskite $BaGeO_3$ structure by high pressure synthesis, as higher Ge coordination number starts to be preferred [3].

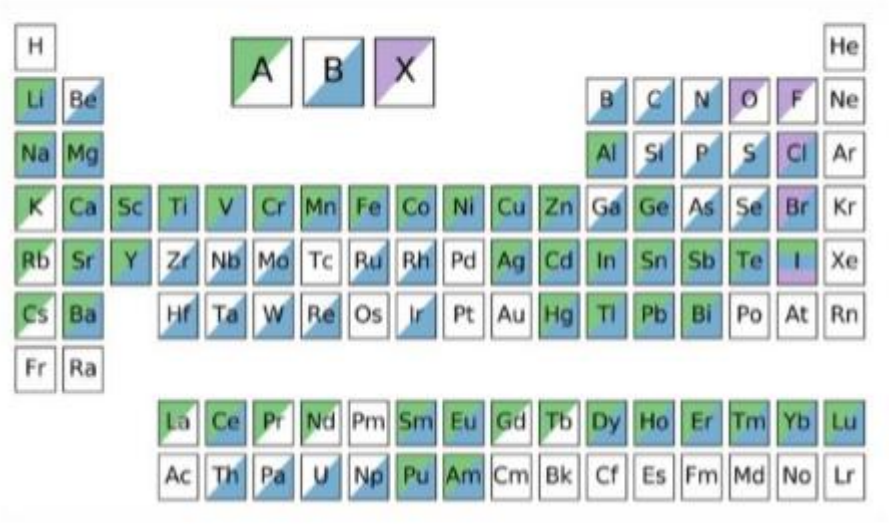

Fig.2.2. A map of the elements which occupy the A, B, and/or X sites within the 576 compounds experimentally characterized as perovskite or non-perovskite at ambient conditions and reported in [4–6]. The data set spans 77 elements, with 49 elements appearing at the A site, 67 at the B site, and 5 at the X site.

It is clear that the perovskite structure can be formed by a great number of atoms and therefore many materials are reported. In the table below are given some of them which exhibit different numbers of oxidation, consequently affecting the crystallographic structure as well as the quantity of oxygen related defects and therefore the final properties. The table gives the ideal A-O, B-O bond distances (d_{A-O}; d_{B-O}) and the ionic radii for several oxides.

Perovskites in $A^{3+}B^{3+}O_3$

	d_{A-O} (Å)	**d_{B-O} (Å)**	***Tolerance factor (t)***
$BiFeO_3$	2.607	2.015	0.915
$GdFeO_3$	2.578	2.015	0.904
$LaAlO_3$	2.685	1.876	1.012
$DyScO_3$	2.514	2.105	0.844
$NdGaO_3$	2.618	1.986	0.932
$BiMnO_3$	2.607	2.016	0.914

Perovskites in $A^{2+}B^{4+}O_3$

	d_{A-O} (Å)	**d_{B-O} (Å)**	***Tolerance factor (t)***
$BaTiO_3$	2.948	1.965	1.061
$SrRuO_3$	2.781	1.984	0.991
$SrTiO_3$	2.781	1.965	1.001
$PbTiO_3$	2.775	1.965	0.999
$CaTiO_3$	2.630	1.965	0.964

Perovskites in $A^{+}B^{5+}O_3$

	d_{A-O} (Å)	**d_{B-O} (Å)**	***Tolerance factor (t)***
$KNbO_3$	3.051	1.971	1.091
$NaWO_3$	2.722	1.975	0.983
KUO_3	3.051	2.142	1.007

Table 2.1.Ideal A-O, B-O bond distances and ionic radii calculated tolerance factor (*t)* for different perovskites of $A^{3+}B^{3+}O_3$ group, $A^{2+}B^{4+}O_3$ group and $A^{+}B^{5+}O_3$ group respectively [4]

2.2. Typical properties of perovskite oxides

As it has been mentioned above, the perovskite oxides can show a large variety of chemical composition and a variety of structures. It is thus not surprising to find that they possess a large number of properties and different applications. There are some applications which have been known since a long time such as ferroelectricity which can be considered somehow the stone of these family of perovskites. This is for instance the case for $BaTiO_3$. Another well-known property is the superconductivity like for $YBa_2Cu_3O_7$. Table 2.2 summarizes the main applications of some of the most known perovskites.

Typical oxide	Main Property
$BaTiO_3$, $PdTiO_3$	Ferromagnetic
$Pb(Zr,Ti)O_3$, $(Bi,Na)TiO_3$	Piezoelectricity
$SrFeO_3$, $LaCrO_3$, $LaNiO_3$	Electrical conductivity
$La_{0.9}Sr_{0.1}CuO_3$, $HgBa_2Ca_2Cu_2O_8$	Superconductivity
$CaTiO_3$, $BaZrO_3$, $BaCeO_3$	Ion conductivity
$LaFeO_3$, $LaMnO_3$	Magnetic property
$LaCoO_3$, $BaCuO_3$	Catalytic
$La_{0.6}Sr_{0.4}CoO_3$, $La_{0.8}Ca_{0.2}MnO_3$	Electrode

Table 2.2.Typical properties of perovskite oxides and some examples[7]

2.3. The double perovskite

Cation substitution is one of the ways to tune the properties of the perovskite oxide compound. The cation can take place both at A or B site and it can involve different amount of substitution. In the case of a substitution of half of the B site with a different cation, there is a possibility of ordered growth double perovskite of composition $A_2B'B''O_6$ where B' and B'' are the two different cations at the B site. A schematic representation of the double perovskite is given in fig.2.3.

The alternation of B and B' cations allow the creation of ordered or disordered structures, adding a degree of complexity in the structure and properties of these compounds, that can be engineered to obtain the desired properties.

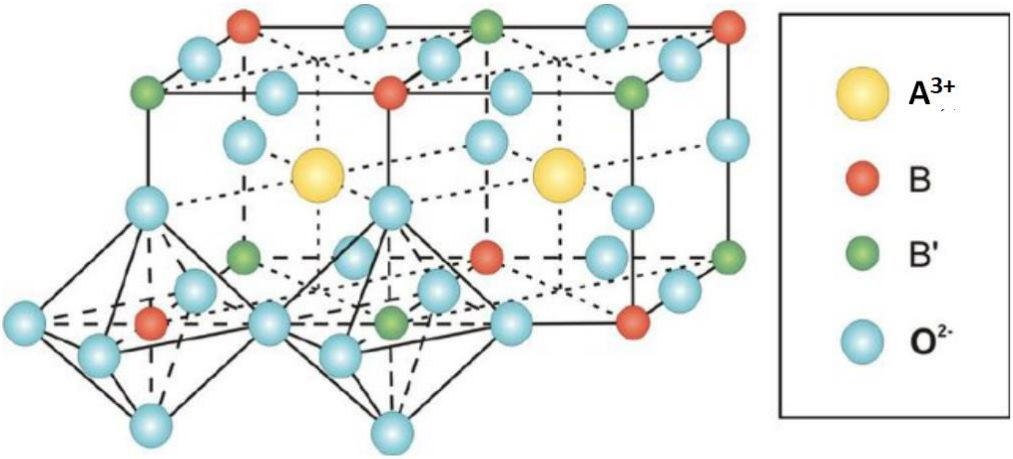

Fig.2.3. $A_2BB'X_6$, in the rock salt double perovskite structure where the A cations are surrounded by an alternating network of BX_6 and $B'X_6$ octahedra[8].

2.3.1 Ordering in double perovskite

The degree of order or disorder inside the double perovskite is of great importance as it controls many of the final properties of the resulting material. For example, the degree of order inside Sr_2FeMoO_6 strongly affects the magnetoresistance as well as the half-metallic properties of the film.[9,10] . Most of the double perovskites crystallize with a rock-salt order (more than 650 compounds have been reported to grow in this way) or just disordered (100 compounds). A third possibility of ordering resides on a "layered" order. It has been postulated that this type of order is only possible in a very narrow range of balancing properties: only 5 compounds have been reported to crystallize in this way[11–13] . The disorder inside the double perovskite can occur in different ways. The most common one is the antisite (AS) disorder, in which one cation just takes the place of the other inside the crystal structure. This type of order' defects happens mostly during the crystal growth because of the configurational entropy. Another common type of defect is the anti-phase boundary (APB). In this case, two ordered zone are divided by two inverted B' and B'' sites.

A schema of ordered and disordered crystal structures is given in fig.2.4.

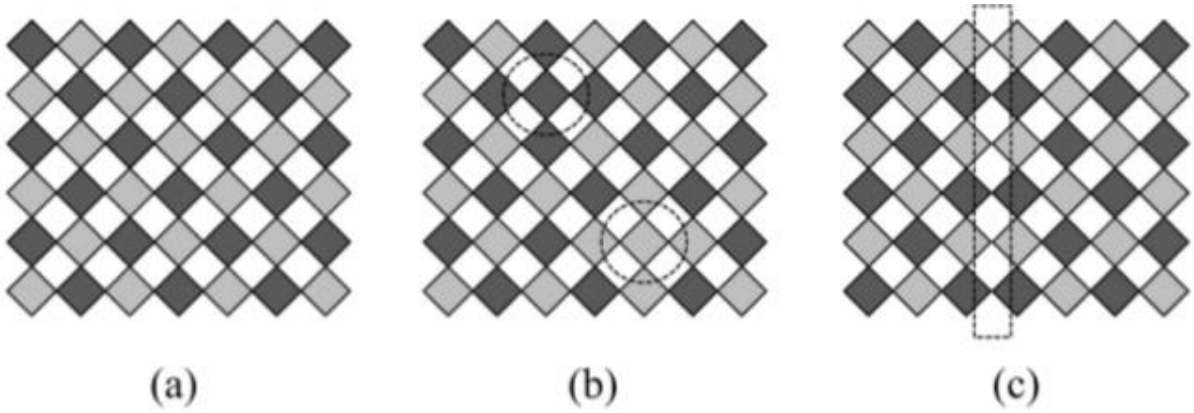

Fig.2.4. B-site cation disorder schemes: (a) completely ordered, (b) antisite disorder and (c) antiphase boundary. [14]

Since the ordering inside the double perovskite is essential for their applications, is important to understand how to study it. Most often, the study of ordering inside the double perovskite is done by diffraction analysis. The ordering and the doubling of the cell generate superstructures peaks which can be easily detected. On the other hand, because of distortion, octahedron tilting and cation ordering can make the results vary. Moreover, if B' and B'' are cations with close number of electrons, it can cause other difficulties in the ordering studies, and consequently it will be hard to distinguish between the two atoms. These problems have already been found in some double perovskite like La_2NiMnO_6 [15], Ba_2RTaO_6 [16] (R= lanthanide) and in some compounds in which B' and B'' have the same number of electrons like $A^{3+}{}_2Ca^{2+}Ti^{4+}O_6$; $A^{2+}{}_2Sc^{3+}V^{5+}O_6$ [17,18].

The degree of order inside the crystal depends on several factors and it's not straightforward to understand whether the film would crystallize in an ordered or disordered way. In fact, most of these compounds are expected to be highly disordered, as a first approximation, at least for energetic consideration[19]. Surprisingly however, many reports on these compounds show that they crystallize in a highly ordered state. One of the suggested reasons of ordering inside the double perovskite lies on the B-site cation' difference oxidation state, $\Delta Z_B=|Z_B''-Z_B'|$, where Z is the oxidation state of the B cation. Generally speaking, it is possible to say that when $\Delta Z_B<2$, the compounds crystallize in a disordered way, while if $\Delta Z_B>2$ the compounds are ordered [4,10,20–22]. Qualitatively speaking, it is possible to explain this effect by an unfavourable situation while placing two high charged B cations one close to the other. More specifically, a high increment of the Madelung energy (which calculates the electrostatic repulsion of an ion in a crystal by approximating the ion to a point charge) [23] is caused

by an increased charge difference[24]. It has been calculated that the Madelung energy ordering is proportional to ΔZ_B^2 which means that the ordering energy can become really important by a small change in the oxidation state. In that case, the repulsion energy overcomes easily the entropic energy and the crystal orders during the growth.[25,26]

The second common reason that provokes cation order is the difference in the radius between the cations. The more is the difference, which reflects in a larger factor $\Delta r_B = |r_B'' - r_B'|$ (where r is the radius of the B cation), the more probable is the ordered growth of the crystal. Making the similar assumption as before, it is possible to consider that larger is the difference Δr_B, more easily the lattice strain can overcome the entropic energy and so the cations are ordered. [26] The effect of ordering by changing the ionic radius of the two cations has been calculated in some different compounds containing M^{3+}/Nb^{5+} by Galasso and Darby in 1962 [27]. From their work, it has been established that a difference in the radii higher than 7% is already enough for cationic ordering. Vasala and Karpinnen, in their double perovskite review[14], summarized the ordering of the double perovskite by ionic radii as follows:

ΔZ_B	**Compound**	**Ordering**
0	$A^{2+}{}_2B'^{4+}B''^{4+}O_6$	Disordered with Δr_B<0.17 Å, ordered above
	$A^{3+}{}_2B'^{3+}B''^{3+}O_6$	Disordered
2	$A^{2+}{}_2B'^{3+}B''^{5+}O_6$	Disordered
	$A^{3+}{}_2B'^{4+}B''^{6+}O_6$	Ordered
	$A^{3+}{}_2B'^{2+}B''^{4+}O_6$	Most of the compounds are at least partially ordered
4	$A^{2+}{}_2B'^{2+}B''^{6+}O_6$	Mostly highly ordered
	$A^{3+}{}_2B'^{1+}B''^{5+}O_6$	Ordered
6	$A^{2+}{}_2B'^{1+}B''^{7+}O_6$	Ordered

Table 2.3. Ordering of known double perovskite by the difference of the oxidation state of B' and B'' cations[14]

2.4. Multiferroic perovskite oxide for Photovoltaics

As mentioned above some of the perovskite oxides can exhibit ferroelectric and ferromagnetic properties that can be interesting for the photovoltaic conversion. Before developing further, let's remind some basics of ferroelectricity, ferromagnetisms and finally multiferroicity effects.

2.4.1. Ferroelectricity

Ferroelectricity is a property that some materials have for which their spontaneous polarization can be switched by an external electric field. A ferroelectric (FE) material will remain polarized even if the external field is removed. Moreover, this polarization can be switched by applying a field larger than critical values (which depend on the materials) called coercive field, E_c. Fig. 2.5 shows a typical curve of polarization versus the electric field for a ferroelectric material. It is possible to distinguish between the thresholds for the coercive field, the remnant polarization and the saturated polarization.

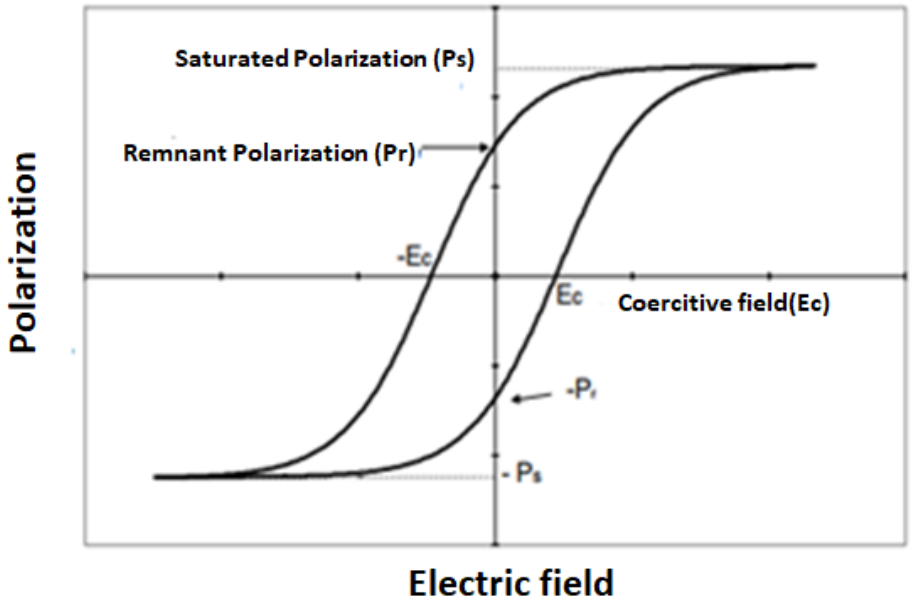

FiG.2.5. Typical curve of Polarization vs the Electric field for a Ferroelectric material. It is possible to distinguish between the Remnant polarization (Pr), the saturated Polarization (Ps) and the coercive field (Ec)[28]

The first discovery of this effect was made in 1921 in single-crystal materials (called Rochelle salt) and subsequently in other materials like perovskite ones (BaTiO3 (BTO) in 1940). In perovskites, 2 phases are possible: the paraelectric one when the crystal is centro-symmetric

and the ferroelectric one where the atoms are displaced along a specific direction showing a net dipole moment which responds to an external polarization. This shifting can occur for different causes. In the case of BFO, as an example, it occurs because the Bismuth in the perovskite structure presents a lone pairs (valence pair of electrons not shared with another atom) on the outer shell of the atom, which are high sensitive to the polarization.

2.4.2. Ferromagnetism

Ferromagnetism is a mechanism where an uncharged material forms permanent magnets. It is given by a certain number of atoms whose spins are aligned one to each other so that they create a net magnetic moment. Different types of magnetism are known in physics: Ferromagnetism and ferrimagnetism are the strongest types and are the most noticeable phenomena that are encountered in mostly everyday life. Other substances respond weakly with another type of magnetism, called paramagnetism, diamagnetism and antiferromagnetism. In fig.2.6 are shown the spins' orientations in each case.

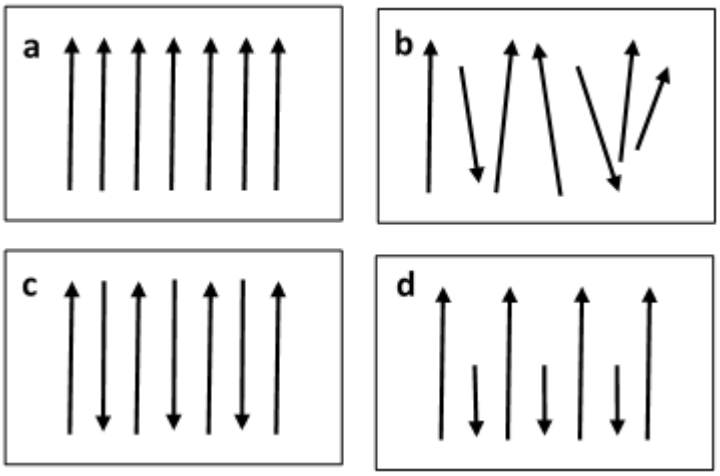

FiG.2.6. Spins representation in different material: a) Ferromagnetic; b) Paramagnetic; c) Antiferromagnetic; d) Ferrimagnetic

Figure 2.6 a shows a ferromagnetic effect, which has been already discussed. In figure 2.6 b a paramagnetic effect is shown; in this case, the material is weakly attracted by an external magnetic field and forms a little induced internal magnetic field as its spins tends to align to the external field. When the atom's spins are ordered antiparallel and can cancel each other there will be an antiferromagnetic order like in figure 2.6 c; when the order is antiferro but

the spin are not sufficient to cancel each other there is a ferrimagnet behaviour as in figure 2.6 d.

2.4.4. Multiferroicity

Multiferroics are a class of materials which shows at least two of the three order parameter (electrical, magnetical and mechanical) at the same time[29–31]. These type of materials, in which it would be for example possible to control magnetism and coupling are of strong interest for different potential application [32–34]. Fig.2.7 gives examples of multiferroic behavior.

Most of the compounds known which show a Multiferroic behaviour have a Curie temperature well below room temperature. The Curie temperature is the temperature at which a ferroelectric material loses its ferroelectric behaviour and starts to act as a paramagnetic one. For example, these MF materials have been investigated for tunnelling magnetoresistance (TMR) sensors or magnetic memories applications, which can in the late case be written electrically and read magnetically.

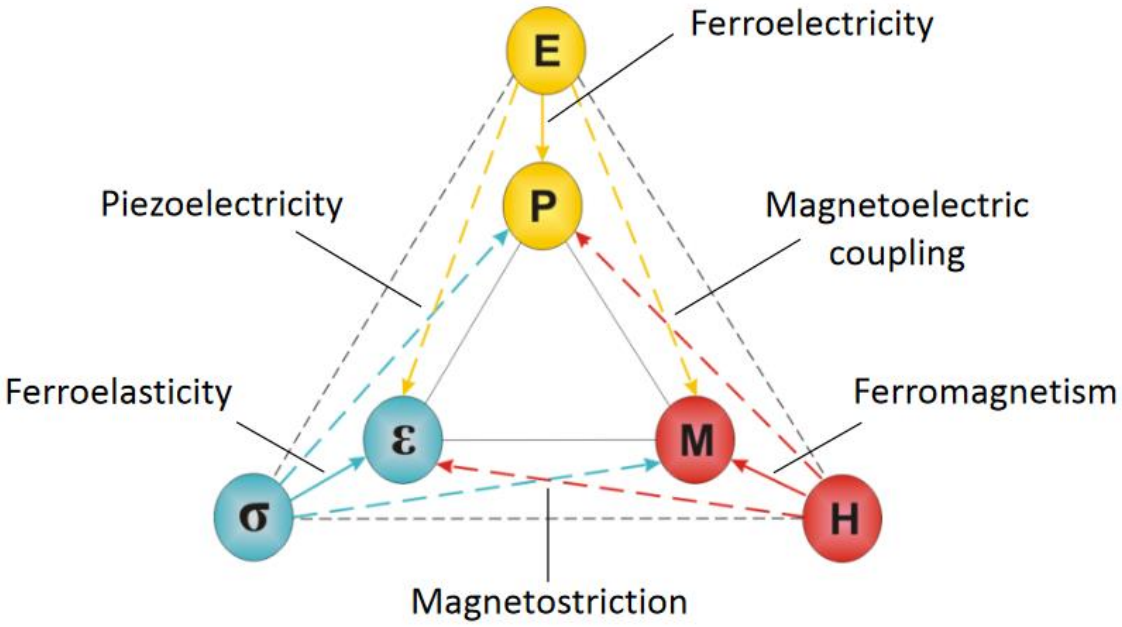

FiG.2.7. Summary of all the functionalities that multiferroic materials may offer. E and P stand for electric field and electric polarization, H and M stand for magnetic field and magnetization, and σ and εstand for stress and deformation, respectively[35]

It is generally difficult to obtain a multiferroic material since there are severe restrictions on the synthesis [30]. Therefore, most of them are complex oxide, as shown in fig. 2.8.

Thus, $BiFeO_3$ (BFO) [33] is a perovskite which has been studied for years since it exhibits ferroelectricity (T_c= 1083 K) [36] and ferromagnetism (T_N= 683 K) [37] at room temperature. Other compounds have been synthesized and demonstrated to have multiferroicity in this condition. Perovskites like BaTiO3 [38] or compounds like KBBNO [39] have also shown promising properties.

Among other oxides present at the interface of the red and green circles, there is the double perovskite Bi_2FeCrO_6 (or BFCO) that has attracted a great interest for several reasons which will be discussed below. For instance, Nechache et al.[40] were able to exploit this material for Photovoltaic (PV) applications to get an unprecedent high solar conversion efficiency of 8.1%.

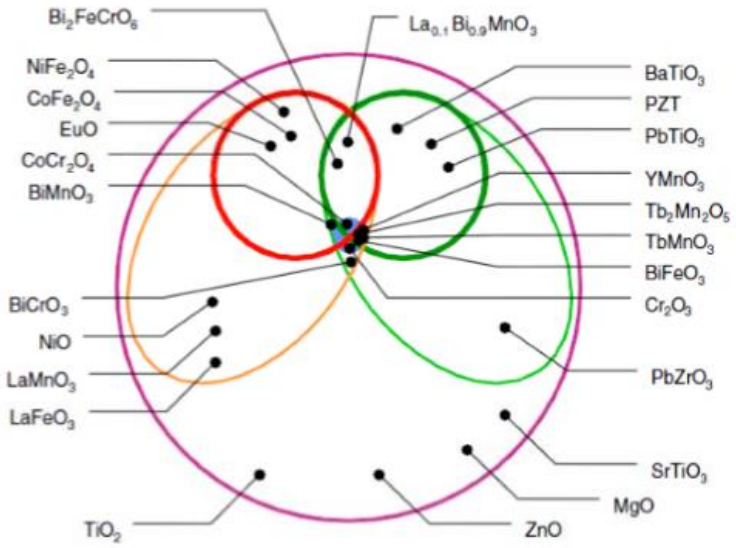

Fig.2.8: In the large circle are represented the insulating oxides of interest; within them there are those polarizable (green ellipse) and magnetically polarizable (orange ellipse). Inside the insert circles, depending on the ellipse, there are Ferroelectrics and Ferro/Ferri-magnets. At the intersections, there are different multiferroics[41]

2.4.5. The case of $BiFeO_3$ and Bi_2FeCrO_6

The closer structure to the one of Bi_2FeCrO_6 (labelled often BFCO) is $BiFeO_3$ (labelled BFO). The structure of BFO is characterized by two distorted perovskite which are connected along diagonal or the pseudocubic [111] direction, to build a rhombohedral unit cell. In this structure, the two oxygen octahedra of the cells connected along the [111] direction are rotated clockwise and counterclockwise around the [111] direction by ± 13.8° and the Fe-ion is shifted by 0.135 Å along the same axis away from the oxygen octahedron center position.

The reported lattice parameter are of a= 3.965 Å and a rhombohedral angle of α = 89.3°. The perovskite can be even described as a hexagonal structure with the c-axis parallel to the diagonals of the perovskite cube; in this case it will be: $[001]_{hex}//[111]_{pseudocubic}$ and , the lattice parameters would be a_{hex} = 5.58 Å and c_{hex} = 13.89 Å. It has been pointed out that BFCO is isostructural to BFO (fig.XX)

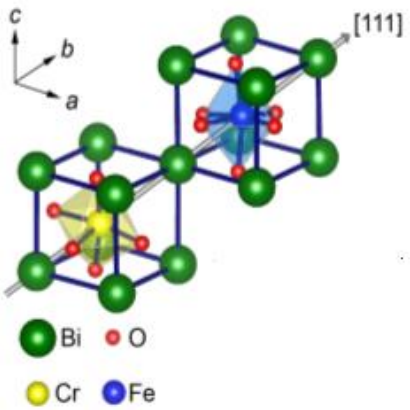

Fig.2.9. Schematic representation of BFCO double perovskite. From[42]

In fact, the Bi_2FeCrO_6 structure can be described by a R3 symmetry (the theoretical lattice parameters for the rhombohedral structures: a_{rh} = 0.547 nm; α_{rh} = 60.09°). This structure can also be approximated by a pseudo-cubic one. As shown in Fig.4.5, it is possible to see the double perovskite both as a pseudo-cubic and hexagonal. By the approximation to a pseudo cubic structure, it is possible to understand why BFCO grows in a 4-folded structure.

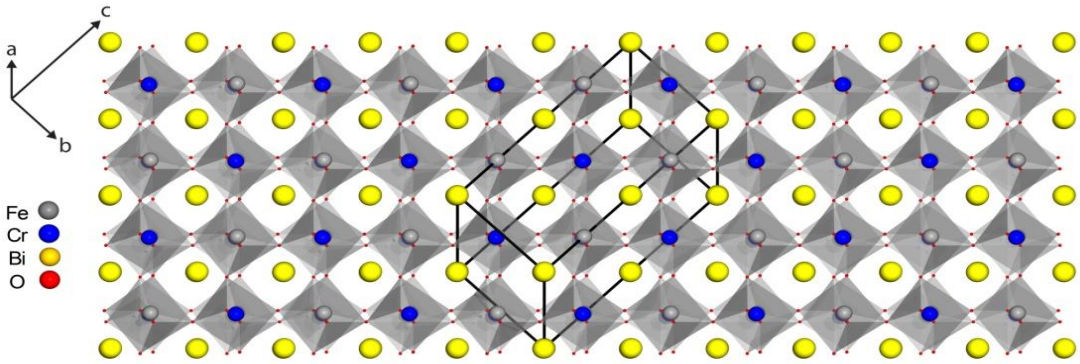

Figure 4.5. Sketch of the crystalline structure of BFCO which underlines the equivalency of the hexagonal and pseudo-cubic notification. The black lines are meant to visually enhance the structure.

It has been predicted to bring, in this long-range order configuration, a magnetic moment of 2 μ_B per formula unit (ca.160 emu/cm^3) at 110K and a ferroelectric polarization of 80 μC/cm^2. It is well known that in order to have a multiferroic material, the two ferroic orders should be brought from 2 different atoms in the crystalline structure.

For BFCO, the ferroelectricity is due to the 6s^2 lone pairs of the Bi^{3+} atoms (like in $BiMnO_3$ or $BiFeO_3$) while the ferromagnetism is linked with Fe^{3+} and Cr^{3+} ordering inside the crystal. Taking into account the Kanamori-Goodenough rules[43,44], ferromagnetism appears when:

- Two transition metal (TM) are ordered in a B'-O-B'' rocksalt structure
- One of these two TM presents e_g electrons while the other don't.

In the case of BFCO, a Fe^{3+} with configuration $t_{2g}^3e_g^2$ coupled with a Cr^{3+} that presents a configuration $t_{2g}^3e_g^0$ should produce a ferromagnetic crystal, while a coupling between Fe-Fe and Cr-Cr should results in antiferromagnetic coupling. This effect was well described by Villafuerte-Castrejon et al.[45] A schematic representation of magnetic domains in the BFCO crystal is given in fig.2.10.

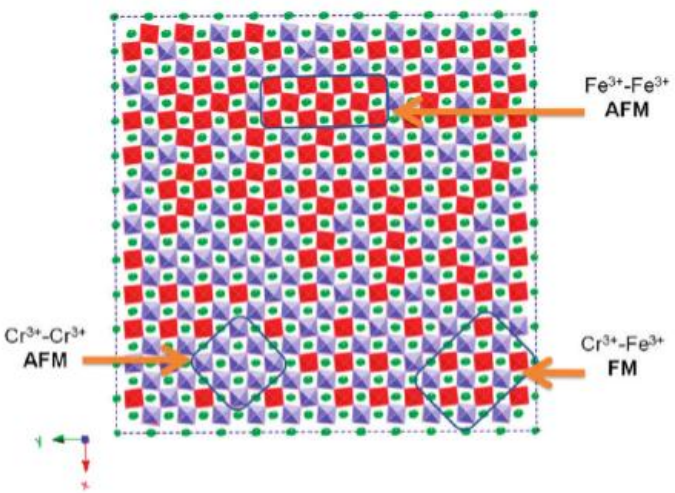

Fig.2.10. Representation of magnetic domains in the crystal, linked to $Fe^{3+}$and Cr^{3+} position[45]

From the synthesis point of view, Bi_2FeCrO_6 is not likely to grow along a specific order as the two atoms in B' and B'' position have similar ionic radii and are most stable in the same oxidation state (Fe^{3+}= 0.645 Å; Cr^{3+}=0.615 Å). As mentioned in section 2.3.1, the BFCO double

perovskite is expected to grow in a simple perovskite structure with Fe and Cr atoms randomly arranged in the crystal structure. First experimental reports of $Bi(Fe,Cr)O_3$ in bulk (ceramic) as well as epitaxial form proved that it is isostructural to $BiFeO_3$ with a rhombohedral distortion [46,47]. Yet, a high quality BFCO double perovskite phase was synthesized in 2009 using the pulsed laser deposition (PLD) method. It was claimed that the phase was stable only in a narrow range of temperature versus oxygen partial pressure, as summarized in Fig. 2.11.

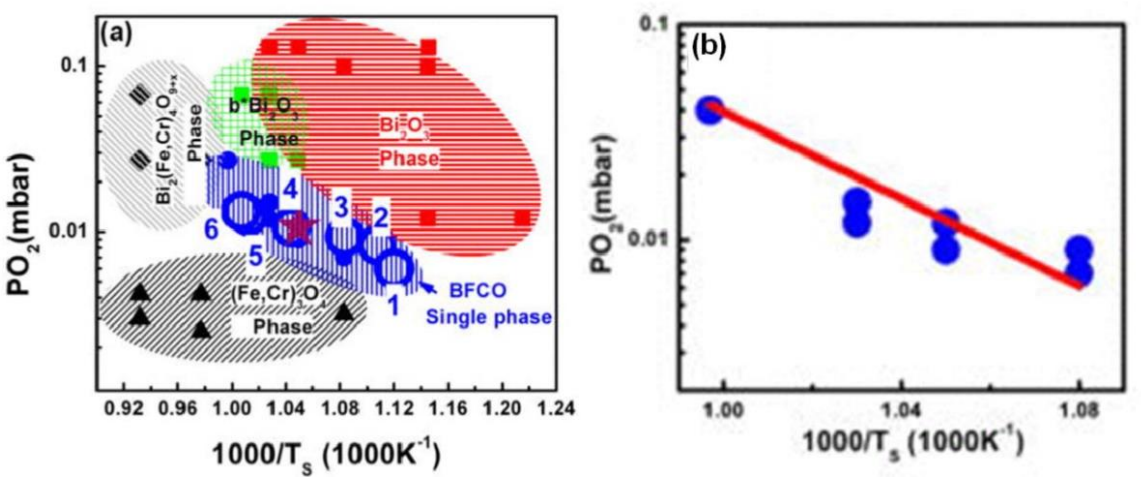

Fig.2.11. a) Temperature/pressure BFCO phase formation diagram shown the zone of stability of the BFCO phase b) central region of the Temperature/pressure diagram from[48]

Thus, Nechache et al. have shown that BFCO with a single phase can be synthesized only within a narrow range of combined temperature and oxygen partial pressure. The ferroelectric properties were also investigated by this group, and the result is shown in Fig. 2.12.

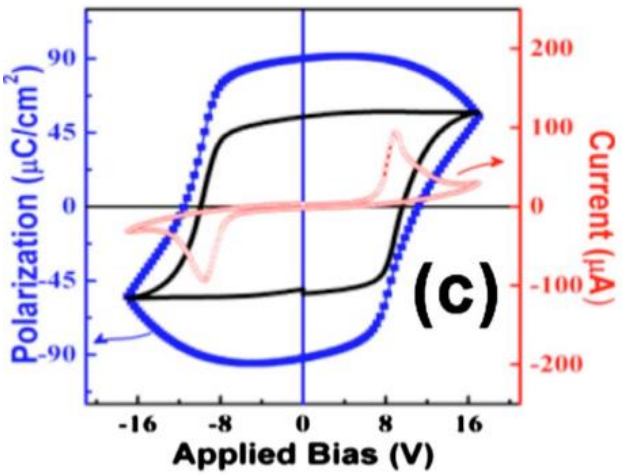

Fig.2.12. Ferroelectric Properties of BFCO Films, from [48]

The black solid line is the polarization after subtracting the leakage contribution. It is worth noticing the reached value of the polarization of 55μC/cm^2 which is close to the theoretical value as predicted by the calculations of Baettig et al.[49] This behaviour was well explained by means of long-range molecular electric field, such as that already found in $BiMnO_3$[31] , Bi_2NiMnO_6[50] and Bi_2CoMnO_6[51]

2.4.6. Tuning the Bandgap

There are great interests to look for new ways to engineer oxide crystals in order to obtain the desired bandgap while maintaining the ferroelectric behaviour as it open paths for several applications, including photovoltaics. For the latest, the limited PV performances of the oxides is mostly due to their high bandgaps (generally above 3 eV). These wide bandgap exceed by far the optimal bandgap value that gives the maximum efficiency for an ideal solar cell [52]. Lowering the bandgap of the oxides is a must. This happen to occur in double-perovskite oxides. In these materials, with a composition $A_2B'B''O_6$, B' and B'' alternates in $B'O_6$ and $B''O_6$ octahedra.[49,53] Just as multiferroic perovskites, ferromagnetism (or antiferromagnetism) is driven by the octahedral $B'O_6$ site while the Ferroelectricity is due to the distortion of the structure by the large A cation. In this case, however, the bandgap is controlled by the interaction of B' and B'' cations passing by O atoms, as in the case of Bi_2FeMnO_6[54]. In other words, manipulating the order of the perovskite allows to obtain perovskites with the same stoichiometric composition but of different bandgaps.

Different double perovskites have been proved to have ferroelectric effect (Bi_2MMnO_6 [55,56] (M=Ni,Co) ; La_2NiMnO_6 [57]). Among them, only Bi_2FeCrO_6 (BFCO) has been established as the one with the more interesting characteristic of bandgap engineering and carriers mobility. . Let's first give some insights on the potential of the ferroelectric perovskite (FEP) based solar cells.

2.5. Photovoltaic Effect in Ferroelectric Perovskite

The ferroelectric photovoltaic effect was discovered about half a century ago in a variety of ferroelectric photovoltaic materials without a centre of symmetry in which a steady photovoltaic response (photovoltage and photocurrent) can be generated along the polarization direction[58,59]. The photovoltaic effect in ferroelectric perovskite oxides is

fundamentally different from the conventional p-n junction based one. In ferroelectrics, only a single material is needed to separate the charges instead of relying on two different doped regions in the same material (homojunction) or in different materials (heterojunction). The main effect relies on the non centro-symmetry of the crystal, i.e. breaking of the strong inversion symmetry, which allows these FE materials to set up a strong internal field which allows charges' separation. What is even more interesting is that the ferroelectric behaviour allows the control of the internal electric fields and injection barriers, mechanism on which Photovoltaic effect relies[60]. In fact, the ferroelectricity generates an internal-induced electric field which can separate the photo-excited charges induced by the light absorption. This effect is even enhanced by the already existing electric field which is created by the Schottky barrier at the interface Ferroelectric/electrode. Another effect which has been usually noticed in FE oxides is the generation of a very high photovoltage (higher than their bandgap in some cases) but low photocurrent. Understanding the FE mechanism is extremely important for the fabrication of a solar cell based on these oxides.

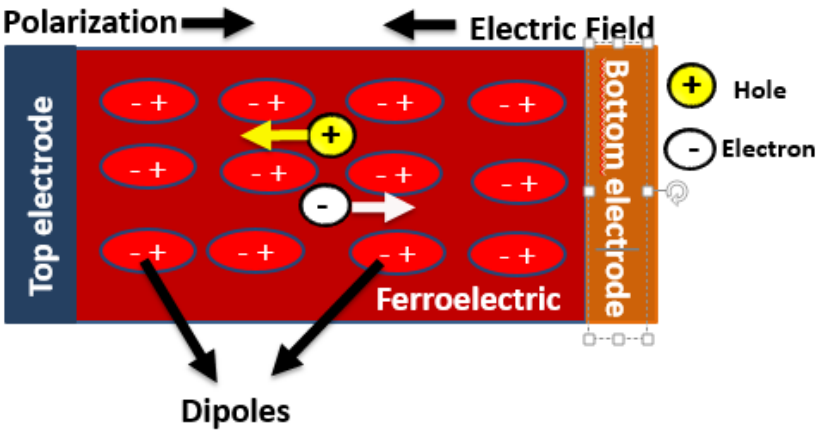

Figure 2.13. Separation of charges mechanism in FE solar cell

2.5.1. Bulk Photovoltaic Effect

PV effect of undoped single crystal oxides like $LiNbO_3$, $BaTiO_3$, $Pb[Zr_xTi_{1-x}]O_3$ has been reported to be originating from bulk photovoltaic effect. When such material is illuminated, the electrons take one direction without crossing other materials as in a common p-n semiconductor. This effect, linked to the asymmetric nature of the crystal, was discussed a lot by researchers who tried to explain it with some models. Firstly it was explain by means of asymmetric carrier model [61,62] which is briefly described in fig 2.14 a where the random diffusion creates a net photocurrent[63]. This model, proposed by Butler et Shurman.[62], assumes

that in a medium which contains randomly located wedges, which are identically oriented, will give rise to a net current (local and short living) only because of inelastic scattering probability calculations.

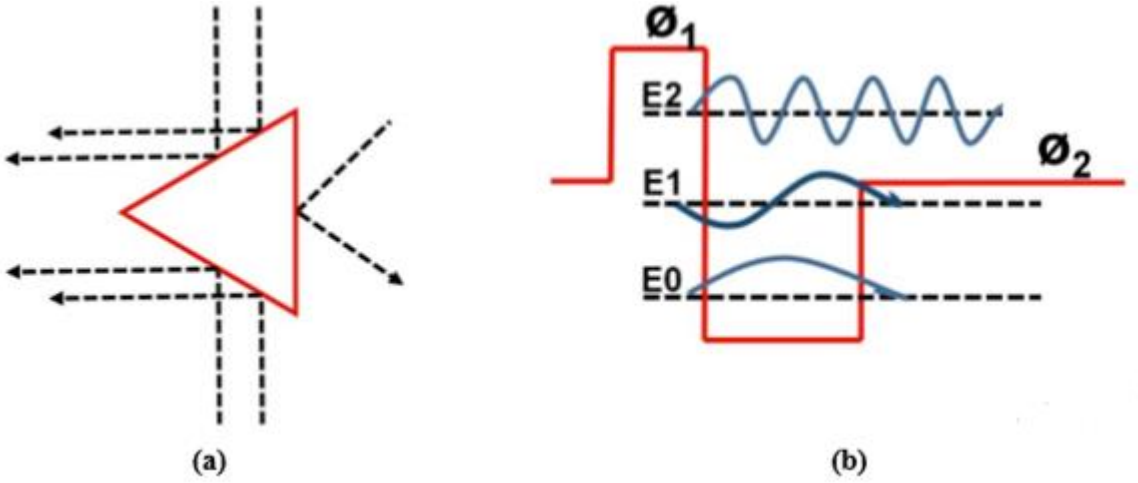

Figure 2.14. Sketch of the two hypothetical mechanism for BPVE source

The asymmetric potential is another model proposed to explain the effect and relies on the asymmetry of the potential at the light absorbing centres developed by the electrical polarization. In the presence of light, the carriers are excited from the ground energy state to state at higher energy E1 and E2 which have a potential energy less than Φ_1 and Φ_2, as described in fig.2.11 (b). From the figure, is possible to see that if the incoming energy in the E1 is less than the potential Φ_1, the electron would be trapped in the potential well while if it is higher than the potential Φ_2, the electron diverges isotropically and the net current will be lower. If the incoming energy is between the potential Φ_1 and Φ_2, the electron is free to reach the end of the well. Eventually, the last possibility would be the tunnelling through the potential barrier Φ_2 .[64]

The precedent models were not able to predict formally the high voltage shown by Ferroelectric materials. Instead, it was proposed another theory, *the shift current*, which has been proved to be a good model to predict the large photovoltage found in non-centro symmetric materials[58,65,66]. This theory was developed after the discovery of BPVE effect in $BaTiO_3$ crystals[67]. In this crystal, in fact, a photocurrent dependence on the light polarization and photon energy was found as well as a BPVE but not strictly linked to the polarization[68]. In these systems, the non-centrosymmetry of the crystal creates an asymmetry in the

momentum distribution of light generated carriers which creates a steady state current. The electrons are excited by the interaction with the monochromatic light changing their momentum, which allows the current to flow from the asymmetry of the potential. The shift current is created by the "shift" of the electron's position at each photon absorbed due to a real-space shift of carriers during interband excitation. The change in position of electrons creates then an internal electric field which is the main contributor to the high photovoltage shown in these materials. Figure.2.15 shows a schematic illustration of the phenomenon. The electron in position A can shift right side in the position B by the absorption of one photon (red arrow), then go from B to C by releasing many photons (black arrow) which creates a net shift current.

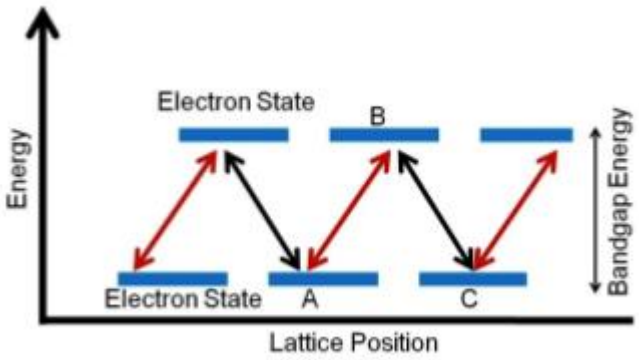

Figure 2.15. Sketch of the mechanism of the shift current

After the first discovery in BaTiO3 crystal, the shift current BPVE has been observed in many other materials systems including ferroelectrics[69–71], quantum wells[72], organic crystals[73] and two-dimensional interfaces[74]. After these discovery, Young and Rappe[75] reformulated the theory to enable the calculation from the first-principle and provided the first comparison of experimental BPVE data with shift current theory. In the subsequent first-principle studies on the shift current in ferroelectric materials, it has been demonstrated how this is the main contributor to the BPVE effect[76–80]

There are other effects which take part in the ferroelectric solar cell working mechanism. For example, under a higher voltage, the polarization can be in principle reversed. From the device side, it has been proved [81,82] that controlling the polarization with an external field allows

electrical tuning of charge transport and hence unidirectional electric conduction. It is therefore interesting to see what other parameters can influence the polarization.

2.5.2. Domain Walls

Photovoltaic in Ferroelectric materials took a new light after an interesting experiment in 2009 on $BiFeO_3$ single crystal which exhibit a switchable behaviour[83] as well as on BFO thin film[81]. As it is possible to see from fig.2.16, illumination with a 28.5 mW/cm^2 white light two different electrodes configuration led to two different photovoltaic responses from the device:

Case a) ➔ above bandgap photovoltage (Voc = 16V) and in-plane photovoltaic current of ≈ 120 $\mu A/cm^2$

Case b) ➔ No Photovoltaic Effect

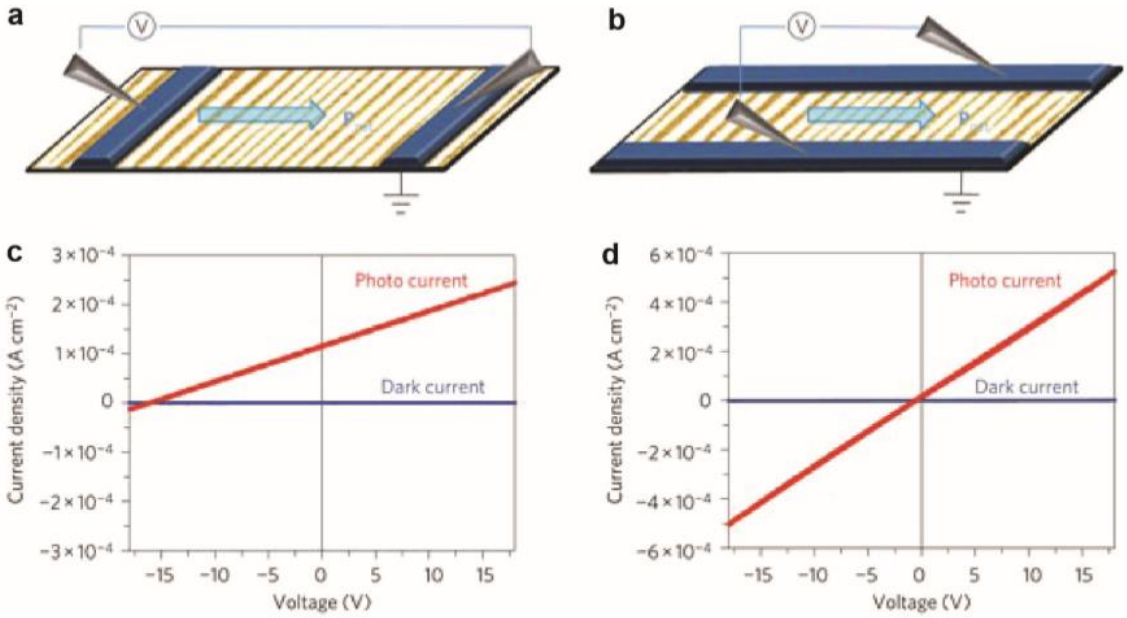

Figure 2.16. a) Bulk photovoltaic effect in BFO with electrodes parallel to domain walls; b) No photovoltaic effect with electrodes perpendicular to the domain walls source

The authors of this work studied the films by PFM in order to confirm the epitaxial growth as well as the presence of the walls. The presence of two type of Domain Walls (DW) and a net polarization in the sample have been proved as shown in Fig.2.17.

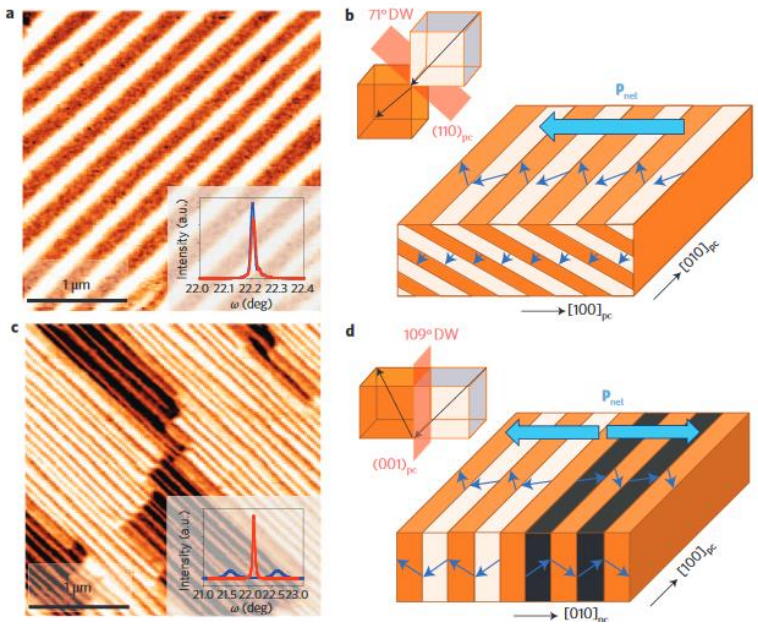

Fig.2.17. Architectures of the domain-wall: a) PFM image of the 71° domain walls. The inset shows X-Ray rocking curves along the two orthogonal axes which confirms the quality of the films. b) Schematic representation of the DW system at 71°. The small arrows marks the components of the polarization (in plane and out of plane) while the big arrows shows the net polarization in the sample. C) and d) show the same for 109° DW[81]

In order to put new light on this experiment and others[84–86] , a new theory linked on domain walls has been established. Domain walls are an extension of few microns inside the FE crystal linked to the spontaneous polarization vector. Each domain in the Ferroelectric, following the domain wall theory, is separated from another by a space of 1-2 nm called "Domain wall"[87]. In these crystal, there is a high probability to produce an excess of charges which accumulates at the interface because of the divergence of the polarization. The explanation given to this phenomena is that a drop in the potential occurs across the domain wall of the crystal, mostly because of the rigid rotation of the polarization, as shown in fig. 2.18.[88]

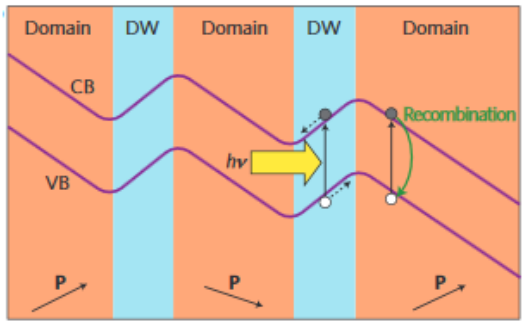

Fig.2.18. operation system for a Ferroelectric solar cell: the diagram shows the Conduction band (CB) the valence band (VB) and the bandgap. hv is the energy of an incident photon which excites the elementary charge (e). The polarization P is shown in the bottom. As it is possible to see , there is a band-bending in the domain wall.[88]

In the case reported above, BFO oxide is known to have domain walls at 71° and 109°. It has been shown that the drop in the polarization was largest for the 180° DWs (example b in fig.2.13), therefore there was no PV effect when metal contacts are disposed perpendicularly to the DWs. The drop was less for 109° DWs (which has been proved to have PV effect[89]) while the least drop is given for 71° DWs. A model was proposed[81,90] based on the assumption that the drop of the potential creates an high electric field in the DW which is able to separate the photogenerated carriers. On the other hand, the charges will experience a lot of recombination in the domain as the electric field is not strong enough. Therefore, it makes sense to compare a Domain Wall with a p-n junction: the DW separate the charges which accumulates into the interface from where they will diffuse.

2.5.3. Ferroelectric Photovoltaic Evaluation

For ferroelectric absorbers (like BFO in fig.2.13), a general phenomenology has been set, which differentiates from the one of a typical p-n junction. In this case (whether the polarization is pointing up or down), the current density scales linearly with the voltage so that it can be expressed as:

$J = -J_{ph} + \sigma F$ (eq.2.1)

Where F is the internal electric field, J_{ph} the photocurrent and σ the total conductivity, which is a combination of dark conductivity σ_d and photoconductivity σ_{ph}:

$\sigma = \sigma_d + \sigma_{ph}$ (eq.2.2)

In the equation 2.1, the internal electric field F, is directly linked to the applied Voltage and internal Voltage, so that the equation 2.3 can be written like:

$J = -J_{ph} + \sigma(V - V_{bi}) / d$ (eq.2.3)

where V_{bi} is the built-in voltage due to the polarization and d is the distance between the electrodes. Thus, the open circuit voltage can be extracted at J=0:

$V_{oc} = V_{bi} + (J_{ph}d)/ \sigma$ (eq.2.4)

The short circuit current depends on the polarization history as well as it scales linearly with the photogeneration rate G:

$J_{sc} = -K.G - J_d$ (eq.2.5)

And from the previous equations:

$J_d = \sigma_d V_{bi}/d$ and $J_{ph} = K.G - \sigma_{ph} V_{bi}/d$ (eq.2.6)

The final equation for current density is therefore:

$J = -J_d - K.G + \sigma V/d$ (eq.2.7)

These relations are valid for many ferroelectrics such as $BaTiO_3$[91].

From these equations, we can get some insight of the photovoltaic response of Ferroelectrics:

- The current depends linearly on the internal induced electric field (which is modulated by different factors, Schottky barriers at interfaces metal/semiconductor, oxygen deficiency, distance of the electrodes…);
- The open circuit voltage depends linearly on the distance of the electrodes which explains why the contact geometry is important to exhibit a BPVE (i.e. BFO in fig.2.16);
- The polarization history has a fundamental role in modulating the photocurrent

2.5.4. Working Mechanism of Ferroelectric Solar Cell

The photovoltaic performances of different ferroelectric solar cells are controlled by the wide properties of the absorbing material and the combination with top and bottom electrodes which should work in a beneficial way for the cell. Different aspects should be taken into consideration while studying the working mechanism as polarity and ferroelectricity can affect it, as discussed later. What should be noticed is that they affect the overall energy diagram by means of bending the surface barriers. From Fig. 2.19 it is possible to see the energy diagram

of an insulator capacitor with asymmetric contacts, which can be related to a primitive solar cell.

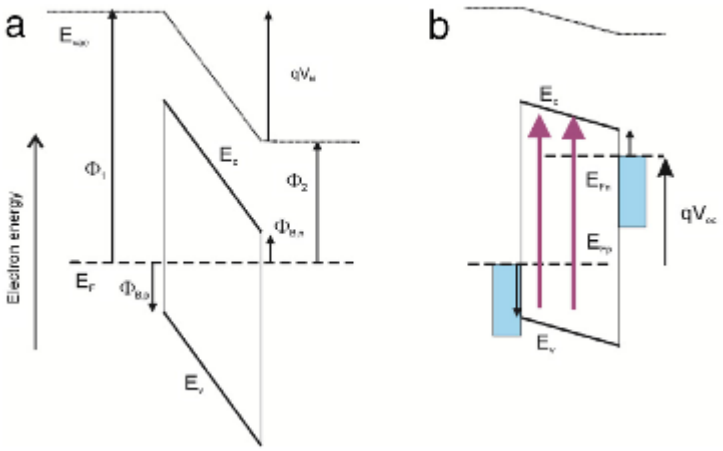

Fig.2.19. Diagram of the energy level for a Metal-Insulator. Energy diagram for a MIM after contact of electrode materials, showing the built-in voltage given by the difference in work functions between both metals [60]

At the equilibrium, the charges are present at the surface (and which are due to bound-polarization charge at the interface metal-ferroelectric) so that σ_{pol}= P. These charges are at least partially compensated from the free charges from the contacts and accumulate at the interface with a density of $\pm\sigma_f$. A schematic representation is given in fig. 2.20:

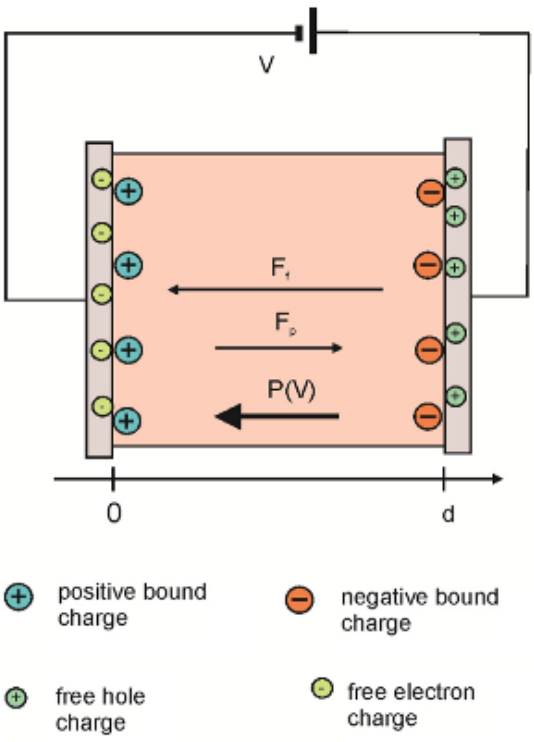

Figure 2.20. Separation of charges mechanism in FE solar cell [60]

2.5.5. The role of the electrodes

The effect of charge compensation due to external contacts is of extreme importance in the PV effect for ferroelectrics, primarily affecting the height of the energy barriers of the solar cell. When applying the polarization, this one has a primary role on charge balance as soon as the voltage is high enough to overcome the coercive field. If considering a simple system with a ferroelectric sandwiched between two electrodes with the same work function, the vacuum level would be tilted after the polarization of the central ferroelectric layer, as shown in fig.2.21 (a). When the system reaches the equilibrium the Fermi level will flatten because of charge compensation from the electrodes, so no electric field will be applied. As remarked by Pintilie and Alexe in 2005[92], the polarization bound is located at a distance δ from the electrode (which can be even of atomic scale) and which means that the ferroelectricity is not suppressed abruptly at the contact interface. These consideration leads to the conclusion that a surface dipole should be formed which changes the injection barrier Φp, as shown in fig 2.21 b.

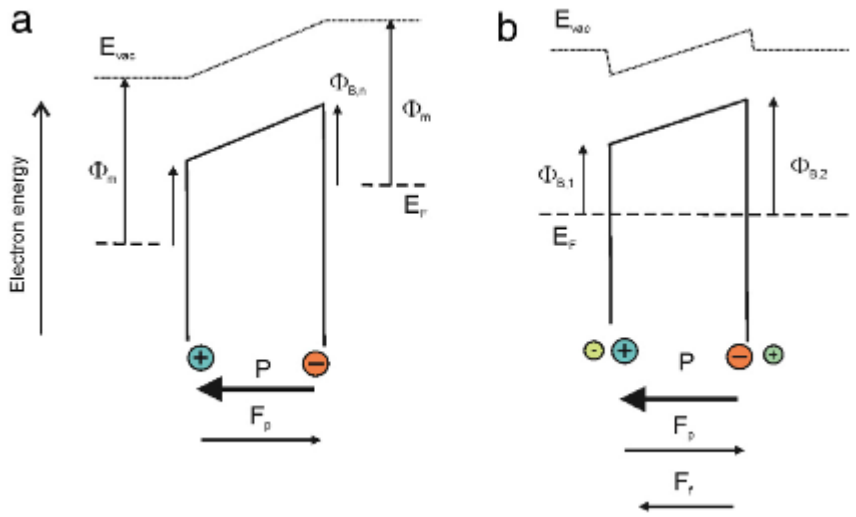

Fig.2.21. Diagram of the energy level for a Metal-Insulator. Energy diagram for a MIM after the application of the polarization (a) ; diagram considering the polarization decrease due to electrode response to polarization (b)[60]

Thus, considering the electrodes form a Schottky barrier at the interface of the Ferroelectric [92–95], it will be possible to change the height of the barrier between the semiconductor and the second contact by playing with the polarization of the ferroelectric material by a factor:

$$\Delta\Phi_P = \pm\,(P/\varepsilon_0\varepsilon_r)\,\vartheta \qquad \text{(eq.2.8)}$$

depending if the polarization P is pointing toward the electrode (-) or away from it (+) [92,94]; ε_r is the dielectric constant of the ferroelectric and ϑ the spatial extent of the spatial layer. As a consequence, the original built-in voltage Vp linked to the different metal work functions is modified by the polarization at each spatial layer. It is known that the built-in potential of the Schottky barrier in the equilibrium state is given by the difference of work function between the metal Φ_m and the one of the semiconductor Φ_{sc}:

$$Vp = (1/q)(\Phi_m - \Phi_{sc}) \qquad \text{(eq.2.9)}$$

Where q is the positive elemental charge. This formula considers the vacuum level alignment after the formation of the interface.

When the dipole is formed in a metal-semiconductor interface, eq.2.9 changes [96] to:

$$Vp' = (1/q)(\Phi_m - \Delta - \Phi_{sc}) = Vp - \Delta/q \qquad \text{(eq.2.10)}$$

Where Δ is the energy step formed at the metal-semiconductor interface.

In the case of a Ferroelectric solar cell with a Schottky barrier, the voltage will change according to eq.1:

$$Vp' = Vp \pm (Ps/\varepsilon_0\varepsilon_r)\ \vartheta \qquad \text{(eq.2.11)}$$

Where Ps takes into consideration the energy step and the charge

Reaching an efficient electron extraction in the device is a fundamental question to create a performing photovoltaic device. As shown, one can in principle imagine to control the polarization induced electric field to control the charge extraction in the device. On the other hand, how the Schottky barrier influence the ferroelectric behaviour is still an open question, as the change in the barrier can be even caused by oxygen vacancies in the layers or some photoinduced effect at the interface. Therefore, in order to have a working FE device, one should take in account all these factors to study the workfunctions of the material and the electrodes aiming at an efficient charge extraction being sure that the effect is not related to other factors.

2.5.6. Current Switching

What's really interesting in Ferroelectrics is the possibility to control the direction of the forward current by changing the polarization direction. Current switching can occur in different manners. One is intimately linked with the Schottky junction at the interface ferroelectric/metal[93,97,98]. In fact, as already mentioned before, choosing a contact with a proper work function, a Schottky barrier is then formed. Changing the polarization direction changes the injection through the barrier and the polarity of the diode can be reversed. Normally one can play with the barrier height at the interface in order to achieve current switchability at a certain coercive field. If the barrier is too high, switching will hardly happen. Another switching process can occur because of internal ferroelectric polarization. In this case, one of the best example has been given by Lee at al.[99] in 2011, who demonstrated that the switching is linked with ferroelectricity. They were using a metal-ferroelectric-metal system (MFM) consisting of 400nm BFO sandwiched between a top Pt electrode and a bottom SRO deposited on STO substrate. In this device, it was shown that the photovoltaic current perfectly superimposed to the polarization hysteresis loop, as it can be seen from fig.2.22.

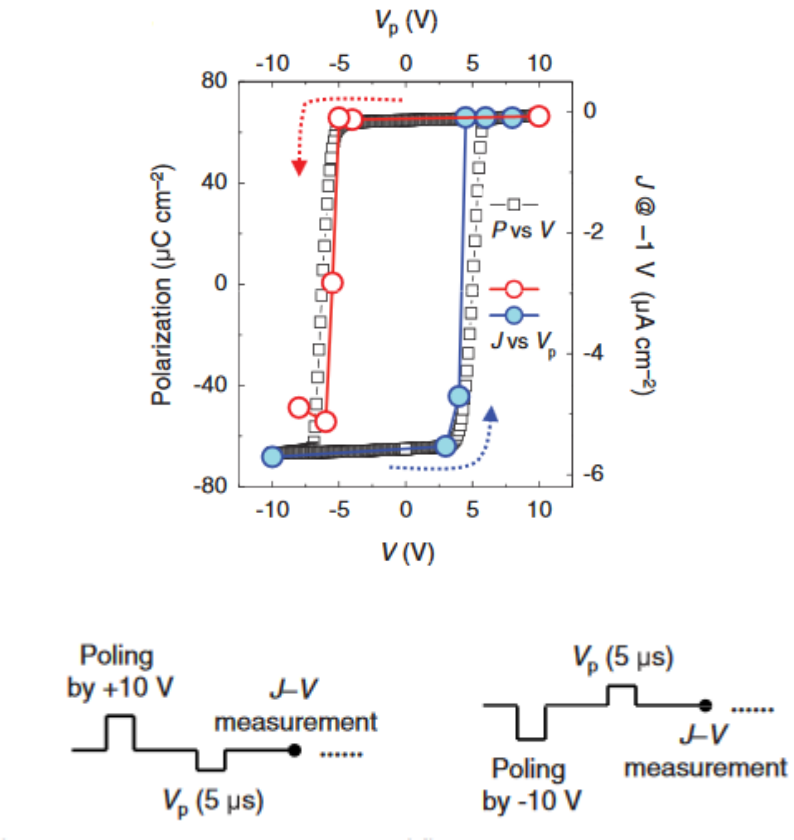

Fig.2.22. The photovoltaic current direction which follows the hysteresis loop in Pt/BFO/SRO device source

After this discussion, It becomes evident how it is possible, with a proper choice of the contacts, to affect the transport properties forming a high resistance contact zone or to exploit the contacts as an advantage for the cell. This effect is extremely important in order to reach switchability of the device: a high Schottky barrier at the interface will be detrimental for the polarization to be switched. Yang et al. [98] have demonstrated how changing the number of charges at the interface by growing epitaxial BFO in the [001] or [111] direction can make the difference between a non-switchable or a switchable device.

The switching effect was also reported in other papers, which regarded not only BFO[82] but also other ferroelectric material like WO_3-doped PLZT[100]. Thanks to these effects, a practical switching memory has been created in the same way than for BFO, where a current density of 0.1 μA/cm^2 was reversed after illumination of 10 mW/cm^2.

2.5.7. Other effects

An internal electric-field is generated not only by the electrodes at the barrier but also from oxygen vacancies. It has been shown for example [99] that in $Pt/BiFeO_3/SrRuO_3$ thin film, it was possible to reach switchability only by removing oxygen vacancies when applying a bias higher than the coercive field. Clearly, defects can be detrimental or helpful for the device: oxygen vacancies can in fact increase conductivity, increase absorption or create a screening field [101]. As an example, in a $BiTiO_3/Si$ [102] device, it has been showed how it was possible to obtain a noticeable photocurrent only with samples grown in poor oxygen atmosphere. This has been explained with the formation of a p-n junction at the interface between the space charged layer of oxygen vacancies in BTO and the p-doped Silicon.

2.6. Summary

In this chapter, we have presented the structure of the perovskite oxides, their properties and potential applications. We have highlight how different factors can engender order or disorder within the crystal and how this is reflected on the properties of the material. We have also shown why the properties of multiferroic oxides can be possibly a path for the next generation of solar cells.

Moreover, we have given an overview of the bulk photovoltaic effect. We have shown how the Domain Walls theory fits well on Ferroelectric oxides to prove the effect. We have in particular highlights what are the conditions to maximize the efficiency of the solar cell based on FE oxides. The main parameters seem to be the thickness of the material, the oxygen vacancies and the type of electrodes. The conditions of current switching were also discussed.

In the following chapters, we will describe the properties of BFCO double perovskite as grown by two different methods. Chapter 3 will focus on the properties of BFCO made using a wet method (sol-gel) while chapter 4 will deal with BFCO grown by a physical method, namely the pulsed laser deposition technique. The structural, optical and electrical properties of the formed BFCO films will thoroughly presented.

References of Chapter 2

1. Park, N.-G. Perovskite solar cells: an emerging photovoltaic technology. *Mater. Today* **18,** 65–72 (2015).
2. Goldschmidt, V. M. Die Gesetze der Krystallochemie. *Naturwissenschaften* **14,** 477–485 (1926).
3. *High-temperature solid oxide fuel cells: fundamentals, design and applications*. (Elsevier, 2009).
4. Zhang, H., Li, N., Li, K. & Xue, D. Structural stability and formability of *AB* O $_3$ -type perovskite compounds. *Acta Crystallogr. B* **63,** 812–818 (2007).
5. Travis, W., Glover, E. N. K., Bronstein, H., Scanlon, D. O. & Palgrave, R. G. On the application of the tolerance factor to inorganic and hybrid halide perovskites: a revised system. *Chem. Sci.* **7,** 4548–4556 (2016).
6. Li, C. *et al.* Formability of *ABX* $_3$ (*X* = F, Cl, Br, I) halide perovskites. *Acta Crystallogr. B* **64,** 702–707 (2008).
7. *Perovskite oxide for solid oxide fuel cells*. (Springer, 2009).
8. *Perovskite: crystallography, chemistry and catalytic performance*. (Nova Publishers, 2013).
9. Serrate, D., Teresa, J. M. D. & Ibarra, M. R. Double perovskites with ferromagnetism above room temperature. *J. Phys. Condens. Matter* **19,** 023201 (2007).
10. Anderson, M., Greenwood, K., Taylor, G. & Poeppelmeier, K. B-cation arrangements in double perovskites. *Prog. Solid State Chem.* **22,** 197–233 (1993).
11. Anderson, M. T. & Poeppelmeier, K. R. Lanthanum copper tin oxide (La2CuSnO6): a new perovskite-related compound with an unusual arrangement of B cations. *Chem. Mater.* **3,** 476–482 (1991).
12. Azuma, M., Kaimori, S. & Takano, M. High-Pressure Synthesis and Magnetic Properties of Layered Double Perovskites Ln $_2$ CuMO $_6$ (Ln = La, Pr, Nd, and Sm; M = Sn and Zr). *Chem. Mater.* **10,** 3124–3130 (1998).
13. Kaimori, S., Kawasaki, S., Azuma, M. & Takano, M. High Pressure Synthesis of Ln2CuSnO6(Ln=La,Pr,Nd,Sm). *J. Jpn. Soc. Powder Powder Metall.* **44,** 127–131 (1997).
14. Vasala, S. & Karppinen, M. A2B'B"O6 perovskites: A review. *Prog. Solid State Chem.* **43,** 1–36 (2015).
15. Blasco, J. *et al.* Synthesis and structural study of LaNi1−xMnxO3+δ perovskites. *J. Phys. Chem. Solids* **63,** 781–792 (2002).
16. Saines, P. J., Spencer, J. R., Kennedy, B. J. & Avdeev, M. Structures and crystal chemistry of the double perovskites Ba2LnB'O6 (Ln=lanthanide B'=Nb5+ and Ta5+): Part I. Investigation of Ba2LnTaO6 using synchrotron X-ray and neutron powder diffraction. *J. Solid State Chem.* **180,** 2991–3000 (2007).
17. Cox, D. E. & Sleight, A. W. Crystal structure of Ba2Bi3+Bi5+O6. *Solid State Commun.* **19,** 969–973 (1976).
18. Zhou, Q. & Kennedy, B. J. High temperature structure of BaBiO3—a synchrotron X-ray powder diffraction study. *Solid State Commun.* **132,** 389–392 (2004).
19. Choy, J.-H., Park, J.-H., Hong, S.-T. & Kim, D.-K. Competition of Covalency between CrIII-O and TaV-O Bonds in the Perovskites Ca2CrTaO6 and Sr2CrTaO6. *J. Solid State Chem.* **111,** 370–379 (1994).
20. King, G. & Woodward, P. M. Cation ordering in perovskites. *J. Mater. Chem.* **20,** 5785 (2010).

21. Woodward, P., Hoffmann, R.-D. & Sleight, A. W. Order-disorder in A2M3+M5+O6 perovskites. *J. Mater. Res.* **9,** 2118–2127 (1994).
22. Setter, N. & Cross, L. E. The contribution of structural disorder to diffuse phase transitions in ferroelectrics. *J. Mater. Sci.* **15,** 2478–2482 (1980).
23. *Encyklopädie der Mathematischen Wissenschaften mit Einschluss ihrer Anwendungen*. (Vieweg+Teubner Verlag, 1921). doi:10.1007/978-3-663-16030-4
24. Katz, L. & Ward, R. Structure Relations in Mixed Metal Oxides. *Inorg. Chem.* **3,** 205–211 (1964).
25. Rosenstein, R. D. & Schor, R. Superlattice Madelung Energy of Idealized Ordered Cubic Perovskites. *J. Chem. Phys.* **38,** 1789–1790 (1963).
26. Cussen, E. J. & Battle, P. D. The influence of structural disorder on the magnetic properties of Sr2Fe1 – xGaxTaO6 (0 ≤ x ≤ 1). *J. Mater. Chem.* **13,** 1210–1214 (2003).
27. Galasso, F. & Darby, W. ORDERING OF THE OCTAHEDRALLY COÖRDINATED CATION POSITION IN THE PEROVSKITE STRUCTURE. *J. Phys. Chem.* **66,** 131–132 (1962).
28. Liang, L., Kang, X., Sang, Y. & Liu, H. One-Dimensional Ferroelectric Nanostructures: Synthesis, Properties, and Applications. *Adv. Sci.* **3,** 1500358 (2016).
29. Ramesh, R. & Spaldin, N. A. Multiferroics: progress and prospects in thin films. *Nat. Mater.* **6,** 21–29 (2007).
30. Hill, N. A. Why Are There so Few Magnetic Ferroelectrics? *J. Phys. Chem. B* **104,** 6694–6709 (2000).
31. Kimura, T. *et al.* Magnetic control of ferroelectric polarization. *Nature* **426,** 55–58 (2003).
32. Vopson, M. M. Fundamentals of Multiferroic Materials and Their Possible Applications. *Crit. Rev. Solid State Mater. Sci.* **40,** 223–250 (2015).
33. Wang, J. Epitaxial BiFeO3 Multiferroic Thin Film Heterostructures. *Science* **299,** 1719–1722 (2003).
34. Scott, J. F. Multiferroic memories: Data storage. *Nat. Mater.* **6,** 256–257 (2007).
35. Spaldin, N. A. MATERIALS SCIENCE: The Renaissance of Magnetoelectric Multiferroics. *Science* **309,** 391–392 (2005).
36. *Physics of ferroelectrics: a modern perspective ; with 24 tables*. (Springer, 2007).
37. Catalan, G. & Scott, J. F. Physics and Applications of Bismuth Ferrite. *Adv. Mater.* **21,** 2463–2485 (2009).
38. Spanier, J. E. *et al.* Power conversion efficiency exceeding the Shockley–Queisser limit in a ferroelectric insulator. *Nat. Photonics* **10,** 611–616 (2016).
39. Grinberg, I. *et al.* Perovskite oxides for visible-light-absorbing ferroelectric and photovoltaic materials. *Nature* **503,** 509–512 (2013).
40. Nechache, R. *et al.* Bandgap tuning of multiferroic oxide solar cells. *Nat. Photonics* **9,** 61–67 (2014).
41. Béa, H., Gajek, M., Bibes, M. & Barthélémy, A. Spintronics with multiferroics. *J. Phys. Condens. Matter* **20,** 434221 (2008).
42. Shabadi, V. *et al.* Origin of superstructures in (double) perovskite thin films. *J. Appl. Phys.* **116,** 114901 (2014).
43. Kanamori, J. Superexchange interaction and symmetry properties of electron orbitals. *J. Phys. Chem. Solids* **10,** 87–98 (1959).
44. Goodenough, J. B. Theory of the Role of Covalence in the Perovskite-Type Manganites [La , M (II)] Mn O 3. *Phys. Rev.* **100,** 564–573 (1955).

45. Villafuerte-Castrejón, M. E. *et al.* New Fe^{3+} / Cr^{3+} Perovskites with Anomalous Transport Properties: The Solid Solution $La_x Bi_{1-x} Fe_{0.5} Cr_{0.5} O_3$ ($0.4 \leq x \leq 1$). *Inorg. Chem.* **50,** 8340–8347 (2011).
46. Suchomel, M. R. *et al.* High pressure bulk synthesis and characterization of the predicted multiferroic Bi(Fe1⁄2Cr1⁄2)O3. *Appl. Phys. Lett.* **90,** 112909 (2007).
47. Kim, D. H., Lee, H. N., Biegalski, M. D. & Christen, H. M. Large ferroelectric polarization in antiferromagnetic BiFe0.5Cr0.5O3 epitaxial films. *Appl. Phys. Lett.* **91,** 042906 (2007).
48. Nechache, R. *et al.* Epitaxial thin films of the multiferroic double perovskite Bi2FeCrO6 grown on (100)-oriented SrTiO3 substrates: Growth, characterization, and optimization. *J. Appl. Phys.* **105,** 061621 (2009).
49. Baettig, P., Ederer, C. & Spaldin, N. A. First principles study of the multiferroics Bi Fe O 3 , Bi 2 Fe Cr O 6 , and Bi Cr O 3 : Structure, polarization, and magnetic ordering temperature. *Phys. Rev. B* **72,** (2005).
50. Shimakawa, Y. *et al.* Direct Observation of *B* -site Ordering in Multiferroic $Bi_2 NiMnO_6$ Thin Film. *Jpn. J. Appl. Phys.* **46,** L845–L847 (2007).
51. Singh, M. P. *et al.* Anomalously large ferromagnetic Curie temperature of epitaxial Bi2CoMnO6 thin films. *Appl. Phys. Lett.* **92,** 112505 (2008).
52. Shockley, W. & Queisser, H. J. Detailed Balance Limit of Efficiency of *p-n* Junction Solar Cells. *J. Appl. Phys.* **32,** 510–519 (1961).
53. Ležaić, M. & Spaldin, N. A. High-temperature multiferroicity and strong magnetocrystalline anisotropy in 3 d - 5 d double perovskites. *Phys. Rev. B* **83,** (2011).
54. Choi, E.-M. *et al.* Interface-Coupled $BiFeO_3$ /$BiMnO_3$ Superlattices with Magnetic Transition Temperature up to 410 K. *Adv. Mater. Interfaces* **3,** 1500597 (2016).
55. Bhattacharjee, S., Eriksson, O. & Sanyal, B. First principles calculations of magnetism, dielectric properties and spin–phonon coupling in double perovskite $Bi_2 CoMnO_6$. *J. Phys. Condens. Matter* **24,** 295901 (2012).
56. Zhao, H. J., Liu, X. Q. & Chen, X. M. Density functional investigations on electronic structures, magnetic ordering and ferroelectric phase transition in multiferroic $Bi_2 NiMnO_6$. *AIP Adv.* **2,** 022115 (2012).
57. Jian Zhao, H. & Ming Chen, X. First-principles study on the differences of possible ferroelectric behavior and magnetic exchange interaction between $Bi_2 NiMnO_6$ and $La_2 NiMnO_6$. *AIP Adv.* **2,** 042143 (2012).
58. Chynoweth, A. G. Surface Space-Charge Layers in Barium Titanate. *Phys. Rev.* **102,** 705–714 (1956).
59. Baltz, R. von. The bulk photovoltaic effect in ferro- and piezoelectric materials. *Ferroelectrics* **35,** 131–136 (1981).
60. Lopez-Varo, P. *et al.* Physical aspects of ferroelectric semiconductors for photovoltaic solar energy conversion. *Phys. Rep.* **653,** 1–40 (2016).
61. Butler, K. T., Frost, J. M. & Walsh, A. Ferroelectric materials for solar energy conversion: photoferroics revisited. *Energy Env. Sci* **8,** 838–848 (2015).
62. Belinicher, V. I. & Sturman, B. I. The photogalvanic effect in media lacking a center of symmetry. *Sov. Phys. Uspekhi* **23,** 199–223 (1980).
63. A. Jalaja, M. & Dutta, S. Ferroelectrics And Multiferroics For Next Generation Photovoltaics. *Adv. Mater. Lett.* **6,** 568–584 (2015).
64. Lines, M. E. & Glass, A. M. *Principles and Applications of Ferroelectrics and Related Materials*. (Oxford University Press, 2001). doi:10.1093/acprof:oso/9780198507789.001.0001

65. Fridkin, V. M. Bulk photovoltaic effect in noncentrosymmetric crystals. *Crystallogr. Rep.* **46,** 654–658 (2001).
66. Fridkin, V. M. The possible mechanism for the bulk photovoltaic effect and optical damage in ferroelectrics. *Appl. Phys.* **13,** 357–359 (1977).
67. Koch, W. T. H., Munser, R., Ruppel, W. & Würfel, P. Anomalous photovoltage in $BaTiO_3$. *Ferroelectrics* **13,** 305–307 (1976).
68. Sturman, B. I. & Fridkin, V. M. *The photovoltaic and photorefractive effects in noncentrosymmetric materials*. (Gordon and Breach, 1992).
69. Auston, D. H., Glass, A. M. & Ballman, A. A. Optical Rectification by Impurities in Polar Crystals. *Phys. Rev. Lett.* **28,** 897–900 (1972).
70. Glass, A. M., von der Linde, D. & Negran, T. J. High-voltage bulk photovoltaic effect and the photorefractive process in $LiNbO_3$. *Appl. Phys. Lett.* **25,** 233–235 (1974).
71. Somma, C., Reimann, K., Flytzanis, C., Elsaesser, T. & Woerner, M. High-Field Terahertz Bulk Photovoltaic Effect in Lithium Niobate. *Phys. Rev. Lett.* **112,** (2014).
72. Bieler, M., Pierz, K., Siegner, U. & Dawson, P. Shift currents from symmetry reduction and Coulomb effects in (110)-orientated GaAs ⁄ Al 0.3 Ga 0.7 As quantum wells. *Phys. Rev. B* **76,** (2007).
73. Ogden, T. R. & Gookin, D. M. Bulk photovoltaic effect in polyvinylidene fluoride. *Appl. Phys. Lett.* **45,** 995–997 (1984).
74. Nakamura, M., Sawa, A., Fujioka, J., Kawasaki, M. & Tokura, Y. Interface band profiles of Mott-insulator / Nb : SrTiO 3 heterojunctions as investigated by optical spectroscopy. *Phys. Rev. B* **82,** (2010).
75. Young, S. M. & Rappe, A. M. First Principles Calculation of the Shift Current Photovoltaic Effect in Ferroelectrics. *Phys. Rev. Lett.* **109,** (2012).
76. Nastos, F. & Sipe, J. E. Optical rectification and current injection in unbiased semiconductors. *Phys. Rev. B* **82,** (2010).
77. Young, S. M., Zheng, F. & Rappe, A. M. First-Principles Calculation of the Bulk Photovoltaic Effect in Bismuth Ferrite. *Phys. Rev. Lett.* **109,** (2012).
78. PVeducation. (2018). Available at: https://pveducation.org/.
79. Wang, F., Young, S. M., Zheng, F., Grinberg, I. & Rappe, A. M. Substantial bulk photovoltaic effect enhancement via nanolayering. *Nat. Commun.* **7,** 10419 (2016).
80. Wang, F. & Rappe, A. M. First-principles calculation of the bulk photovoltaic effect in KNbO 3 and (K,Ba)(Ni,Nb) O 3 − δ. *Phys. Rev. B* **91,** (2015).
81. Yang, S. Y. *et al.* Above-bandgap voltages from ferroelectric photovoltaic devices. *Nat. Nanotechnol.* **5,** 143–147 (2010).
82. Wang, C. *et al.* Switchable diode effect and ferroelectric resistive switching in epitaxial BiFeO3 thin films. *Appl. Phys. Lett.* **98,** 192901 (2011).
83. Choi, T., Lee, S., Choi, Y. J., Kiryukhin, V. & Cheong, S.-W. Switchable Ferroelectric Diode and Photovoltaic Effect in $BiFeO_3$. *Science* **324,** 63–66 (2009).
84. Catalan, G., Seidel, J., Ramesh, R. & Scott, J. F. Domain wall nanoelectronics. *Rev. Mod. Phys.* **84,** 119–156 (2012).
85. Sluka, T., Tagantsev, A. K., Bednyakov, P. & Setter, N. Free-electron gas at charged domain walls in insulating BaTiO3. *Nat. Commun.* **4,** (2013).
86. Guyonnet, J., Gaponenko, I., Gariglio, S. & Paruch, P. Conduction at Domain Walls in Insulating Pb(Zr0.2Ti0.8)O3 Thin Films. *Adv. Mater.* **23,** 5377–5382 (2011).
87. Ho Sung, J. *et al.* Single ferroelectric-domain photovoltaic switch based on lateral BiFeO3 cells. *NPG Asia Mater.* **5,** e38–e38 (2013).

88. Huang, H. Solar energy: Ferroelectric photovoltaics. *Nat. Photonics* **4,** 134–135 (2010).
89. Seidel, J., Yang, S.-Y., Alarcón-Lladó, E., Ager, J. W. & Ramesh, R. Nanoscale Probing of High Photovoltages at 109° Domain Walls. *Ferroelectrics* **433,** 123–126 (2012).
90. Seidel, J. *et al.* Efficient Photovoltaic Current Generation at Ferroelectric Domain Walls. *Phys. Rev. Lett.* **107,** (2011).
91. Spanier, J. E. *et al.* Power conversion efficiency exceeding the Shockley–Queisser limit in a ferroelectric insulator. *Nat. Photonics* **10,** 611–616 (2016).
92. Pintilie, L. & Alexe, M. Metal-ferroelectric-metal heterostructures with Schottky contacts. I. Influence of the ferroelectric properties. *J. Appl. Phys.* **98,** 124103 (2005).
93. Blom, P. W. M., Wolf, R. M., Cillessen, J. F. M. & Krijn, M. P. C. M. Ferroelectric Schottky Diode. *Phys. Rev. Lett.* **73,** 2107–2110 (1994).
94. Pintilie, L. *et al.* Metal-ferroelectric-metal structures with Schottky contacts. II. Analysis of the experimental current-voltage and capacitance-voltage characteristics of Pb(Zr,Ti)O3 thin films. *J. Appl. Phys.* **98,** 124104 (2005).
95. Yuan, G.-L. & Wang, J. Evidences for the depletion region induced by the polarization of ferroelectric semiconductors. *Appl. Phys. Lett.* **95,** 252904 (2009).
96. Bisquert, J. *Nanostructured energy devices: foundations of carrier transport*. (CRC Press, Taylor & Francis Group, 2018).
97. Ahn, C. H., Triscone, J.-M. & Mannhart, J. Electric field effect in correlated oxide systems. *Nature* **424,** 1015 (2003).
98. Yang, S. Y. *et al.* Photovoltaic effects in BiFeO3. *Appl. Phys. Lett.* **95,** 062909 (2009).
99. Lee, D. *et al.* Polarity control of carrier injection at ferroelectric/metal interfaces for electrically switchable diode and photovoltaic effects. *Phys. Rev. B* **84,** (2011).
100. Yao, K., Gan, B. K., Chen, M. & Shannigrahi, S. Large photo-induced voltage in a ferroelectric thin film with in-plane polarization. *Appl. Phys. Lett.* **87,** 212906 (2005).
101. Paillard, C. *et al.* Photovoltaics with Ferroelectrics: Current Status and Beyond. *Adv. Mater.* **28,** 5153–5168 (2016).
102. Xing, J. *et al.* Photovoltaic effects and its oxygen content dependence in BaTiO3−δ/Si heterojunctions. *Appl. Phys. Lett.* **92,** 071113 (2008).

Chapter 3.
Properties of BFCO deposited by sol-gel technique

Among the chemical tools to fabricate materials especially as thin films, the sol-gel solution method is the most popular one. It is a low-cost technique which is commonly used for synthesising different compounds and it has been proved to be suited for the synthesis of magnetic and multiferroic compounds [1–5]. In particular, the synthesis of compounds such as $BiFeO_3$ and $BiCrO_3$ by sol-gel was already demonstrated but to date, there are not many information regarding the sol gel synthesis of BFCO films. The main problem resides on the fact that many Bi-based perovskites with the formula $Bi[B]O_3$ requires usually high pressure in order to obtain their perovskite form [6]. In principle, $BiFeO_3$ is one of Bi perovskite which does not require high pressure. It is therefore of great importance and challenging to obtain a single phase using the sol-gel solution and annealing under atmospheric pressure. In fact, the chemical stability of BFO is quite controversial: some groups showed a stability until 930 °C [7,8] and after it decompose into Bi_2O_3 and $Bi_2Fe_4O_9$ [9]; Others reported that it is only stable under 830 °C [10] or even at lower temperatures [11]. Thus, it has been pointed out from Lisnevskaya et al.[11] that the reaction proceeds at 80% conversion into BFO at above 700 °C but only keeping this reaction at this temperature many hours. Near 100% conversion have been obtained by firing at 850 °C for 5-10 min while longer treatment times lead to the formation of the two products mentioned above [12]. Complementary studies have also addressed the synthesis of these ceramic by sol gel method [13–15] and most of them have demonstrated difficulties for a 100% conversion into BFO. Since a BFO perovskite is already very difficult to obtain by sol-gel, it is expected to be more challenging for the double perovskite BFCO.

In this work, we have prepared the sol-gel solution containing the appropriate weight of elements of the BFCO; then the spun solution was thermally heated using either a conventional furnace (CTA or conventional thermal annealing) or a lamps assisted furnace (RTA or rapid thermal annealing) following the methodology published by Murari et al. [16] for $BiFe_{0.95}Cr_{0.05}O_3$ material.

3.1. Sol-gel solutions preparation:

Three solutions of the different metal chelates in propionic acid (Bi^{3+} , Cr^{2+} and Fe^{3+}) were provided by RBnano company. The concentration of the solutions depends on chelates

solubility and are ranging from 0.5mol/l to 1 mol/l. To prepare the final sol-gel solution we calculate the amount of each solution to be mixed and assuming densities close to 1 we weight the quantities of each solutions and poor then in the same recipient. The final mixture is used for spin coating and few grams are dried and preheated at 400°C to remove all organic moieties. This amorphous powder is used for DTA-TGA measurements.

3.2. Powder preparation and Thermo-Gravimetrical Analysis-Differential Thermal Analysis

Before starting sol gel deposition, some analyses have been carried on a powdered precursor produced by solution drying and preheating at 400 °C in order to eliminate the organic parts. It leads to an amorphous precursor of BFCO. The powder was synthesized by solid state method starting from Bi_2O_3; Fe_2O_3 and Cr_2O_3 taken in stoichiometric quantity; an excess of 10% of Bismuth was added in order to compensate the loss due to its volatility. The powders were mixed up and then grounded down into a mortar. Subsequently Thermo-Gravimetrical Analysis-Differential Thermal Analysis (TGA-DTA) were performed on the resulting powder.

Figure 3.1 shows TGA-DTA done on few milligrams of BFCO powdered precursor. Around 360°C a first reaction that regards residual organic compounds occurs. Between 360°C and 460°C, an endothermic reaction happens associated with a loss of weight. This can be due to the formation of CrO from reaction of native Cr_2O_3 with residual organic moieties

$Cr_2O_3 \rightarrow 2\ CrO + ½\ O2$

(as it can be noticed by a loss of weight and a broad peak in the heat flow).

This assumption is made as between the possible reducing atoms in the powder (Fe and Cr), Cr is the easier to reduct at this temperature (assuming the presence of some native carbon which can catalyse the reduction). If this assumption holds true, small gain of weight which starts at 580 °C can be related to a change of chromium valence from Cr^{II} to Cr^{III} (and a gain of oxygen which increase the weight) where CrO oxidises in Cr_2O3 and the reaction of BFCO phase formation takes place. The reaction holds on until the temperature increases around 750 °C and a degradation reaction occurs (notable as a fast loss of weight) corresponding to the sublimation of Bi_2O_3 close to melting temperature:

$Bi_2O_3 \rightarrow 2BiO + ½\ O_2$

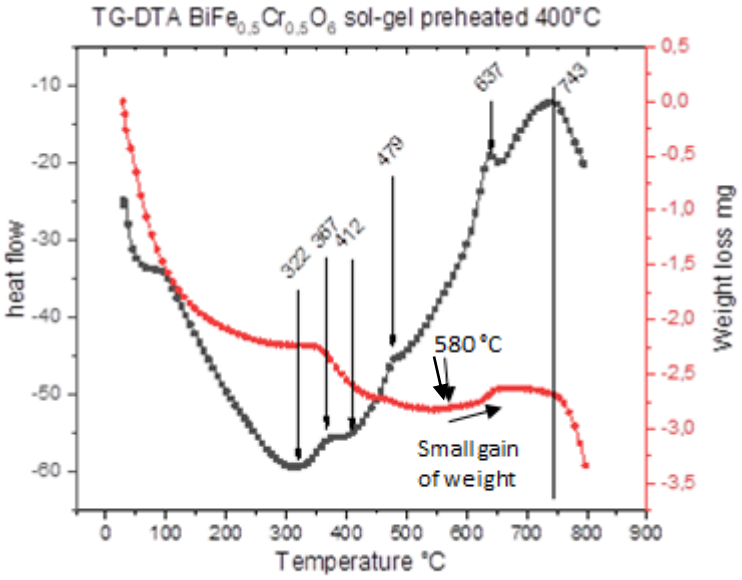

Fig.3.1: Fast TGA made on BFCO powder

From these preliminary analysis, it is possible to confirm that our powder is forming the phase at lower temperatures compared to the one predicted for BFO from Lisnevskaya et al.[11], which predicted a phase formation in a range of Temperature between 800 °C and 850 °C. In order to get a better idea on the reactions taking place in the compounds, XRD analysis on the powder were performed. In figure 3.2 are shown the XRDs made on the powder of BFCO at different temperatures: at 500 °C, when the BFCO phase formation should not have yet started; at 650°C corresponds to when the reaction have just started and at 750°C when the reaction is completed. The powders annealed at 500°C and 650°Cr were kept in the furnace with a heating rate of 5°C/min and kept in the oven to cool down. This treatment could have been a problem at 750 °C, as the ramp could have started some lower Temperature reactions without giving them the time to go to completion. To avoid reactions which could have interfeared, the powder was introduced in the furnace directly at a set temperature of 750°C and cooled down to room temperature which takes 6h

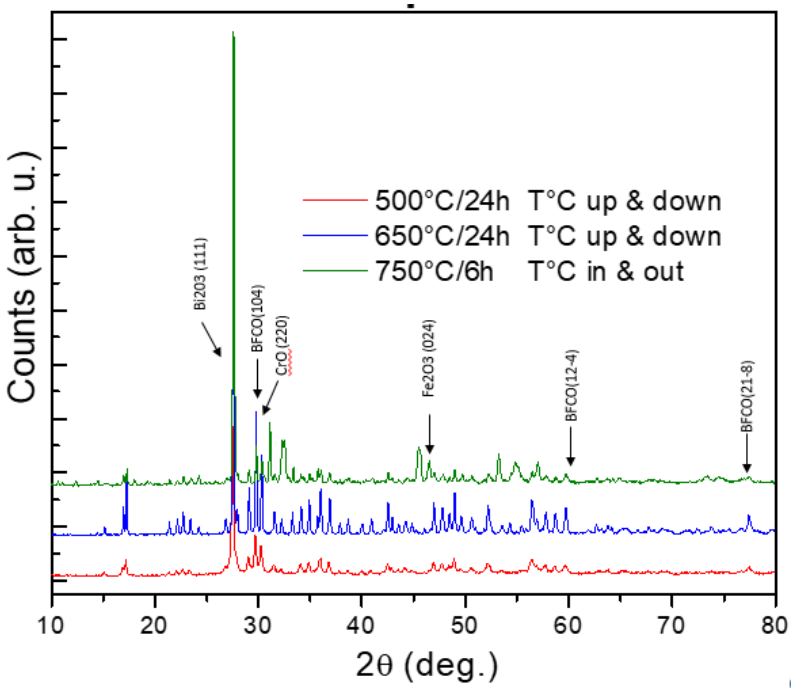

Fig.3.2: XRD of BFCO powder annealed at 500 °C (red); 650 °C (blue): 750 °C (green)

The first remark from figure 3.2 is that the phase of Bismuth oxide (Bi_2O_3) is always present in the powder at very high intensity. Iron and chromium oxides signatures are well present at 500°C, while they start to lower at 650°C and are very weak at 750°C. The BFCO phase within the powder is identified by taking into consideration the presence of the peak around 80°, which is also present for BFCO made by PLD deposition as it will be shown later. The double perovskite phase starts to appear at 650°C when the reaction has just initiated and it is also present at 750°C but the peak is at low intensity as the reaction ended and degradation reaction begins. This behaviour can be assigned to a long time of reaction (6h in this case). The main issue is still the formation of parasitic phases as witnessed by the presence of several peaks in Figure 3.2. To partially solve the problem, the powder was treated at an intermediate reaction temperature and kept in the oven only 60 minutes. The XRD results are shown in Figure 3.3 a. and b.:

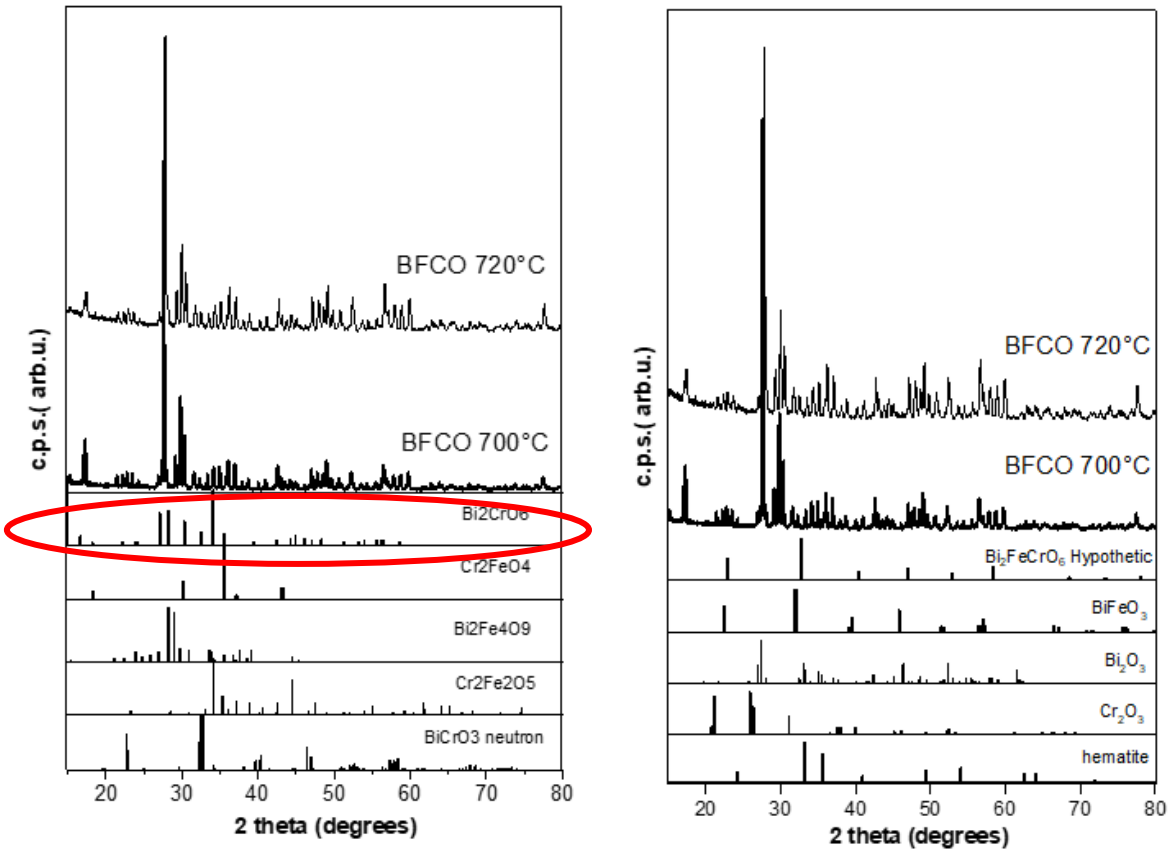

Fig.3.3: a) XRD of BFCO powder annealed at 700 °C for 60 min; and the JCPDS file of theoretical compounds.

By these analysis we even tried to understand more about the intermediate reactions of BFCO phase formation as well as its development by increasing the temperature. Figure 3.3 shows that a lower time of heating at 700°C still results in the formation of different phases in the powder.. It is worth to notice the presence of an amorphous phase visible at the low angle region of the diffraction spectra, which is more marked at 720 °C than at 700 °C. JCPDS files are shown at the bottom of the figures in order to prove the presence of different compouds in the films. The most probable phase will be the $Bi_2 CrO_6$ with a doping of Fe which made a shift to lower angles. We speculate that this is the consequence of some non-complete reaction, as the reaction ending point was not reached at 720 °C. It can be partially concluded from these investigations that our experimental procedure did not allow to grow BFCO with a

single phase of BFCO, as several parasitic phases are still present. Such results are in agreement with those of Lisnevskaya et al.[6] who claim that thermal annealing under only high pressures favours the formation of single phase compounds. Yet, we have pursue our studies to attempt forming BFCO thin films by the sol-gel method starting from the synthesized powders as a precursor.

3.3. BFCO layer deposition

The Sol-gel solutions were obtained from oxide powders with a jellying agent. A 10% excess of Bismuth was added to the solution in order to compensate the expected weight loss due to its volatility at high temperature. The as-formed solutions were stirred at 80 °C and cooled down, then deposited by spin coating on silicon or quartz substrates. Subsequently, the solutions were spun at different speed (1500, 2500, 3500 or 4500 rpm) for 60s. Then 2 different types of annealing have been performed, commont thermal annealing (CTA) and rapid thermal annealing (RTA). In the CTA annealing, the BFCO films on substrates were thermally treated in a conventional furnace in air at increasing temperature. The annealing time was varied from 1 h to 6 hours, depending on the experiment. In case of treatment in a RTA furnace, the samples were heated at 750 °C for 2 or 3 minutes under Nitrogen/ Oxygen flow (80:20 or 70:30).

3.3.1. CTA of sol-gel BFCO solutions

a) Films preparation

Prior to the deposition the <100> silicon substrates used for this experiment were cleaned in a HF/H_2O (1:10) solution for 90 s in order to eliminate the native SiO_2; then the silicon surface was etched with an oxygen plasma for 30 s to create Si-O zones and facilitates the wetting. Subsequently, the substrates were placed in a spinning equipment. On the other hand, the solutions were stirred at 80 °C and then cooled down. Later, few drops were deposited on the Si substrates and spun at a speed of 1500 rpms for 60s. The substrates with the fresh layer on top were preheated at 350 °C for 10 minutes in order to remove the organic compounds. Afterwards, they were CTA heated at temperatures from 500 to 800°C for 1 h as indicated in Table 3.1.

Samples	Temperature (°C)	Atmosphere	Time (min)	Layers*	Substrate
BFCO 500	500	air	60	1	Si
BFCO 550	550	air	60	1	Si
BFCO 700	700	air	60	1	Si
BFCO 750	750	air	60	1	Si
BFCO 800	800	air	60	1	Si

Table 3.1: BFCO films prepared by sol gel on Silicon substrate and CTA annealed in air

As for the film thickness, a deposition process of a film at a speed of 1500 rotation per minute (rpm) for 60 seconds and annealed at 700°C results in an average 90 nm thick film, as shown in SEM cross-section later (fig.3.8). This is an important information when it comes to the final application such as a photovoltaic device which requires an appropriate thickness for an optimal photon conversion.

3.3.2.Structural properties of the films

The XRD spectra of the BFCO sol-gel films on silicon and CTA treated in air as prepared above are reported in figure 3.4. In these spectra, most of the peaks were not labelled as the peaks exhibit low intensities. Yet, it is possible to make a comparison with figures 3.2 and 3.3 which concern the XRD spectra of the raw powder BFCO compounds.

As it can be seen from figure 3.4, only Bi_2O_3 phase is formed at 500 °C. A peak at 17.5° starts to rise at 550 °C but disappears completely at 800 °C. Taking in account the TGA analysis, this peak can be related to a secondary phase appearing during the formation of BFCO phase and disappearing when the degradation reaction starts. On the other hand, a secondary phase related to degradation reaction is visible at angle 22.5°. At 700°C a low intensity peak starts to appear and it become more intense until forming a doublet at 800 °C. Finally, a low intensity peak is observed at 78° for samples annealed at 700 and 750°C, which may indicate the formation a BFCO phase. This is consistent with the TGA analysis reported above which revealed that the BFCO phase can be formed in the range of temperature 700°C-750°C.

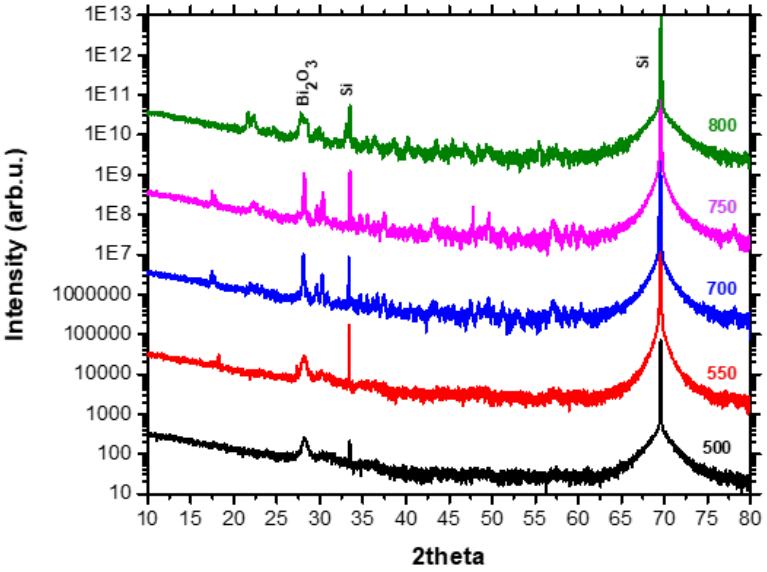

Fig.3.4: X-Ray diffraction spectra of BFCO films deposited by sol gel and heated at different temperatures in air ambient

To get more insights, Raman Spectroscopy analysis were recorded in the range 100 – 700 cm^{-1} for BFCO sol-gel films deposited on silicon substrates and annealed at different temperatures. The spectra are given in Figure 3.5 a. The typical peak of the crystalline silicon is clearly visible at 520 cm^{-1} for all samples. The spectra reveal that several features are present for the samples annealed at 700 and 750°C while none are found for the samples treated at 500°C and 800°C. For a comparison purpose, we show the raman spectra recorded on the BFCO deposited by PLD (fig.3.5 b) and a zoom of the raman on sol-gel in the zone (100-700 cm^{-1}). We also show the Raman spectra reported by Yin et al. [17] of BFO and BFCO films grown on Fluorine Tin Oxide (FTO) (fig.3.5 d). Their BFCO film contains also only a low amount of Chromium ($BiFe_{0.97}Cr_{0.03}O_3$). The presence of peaks in the region around 100-200 cm^{-1} is indicative of a signature of BFO-BFCO phases.

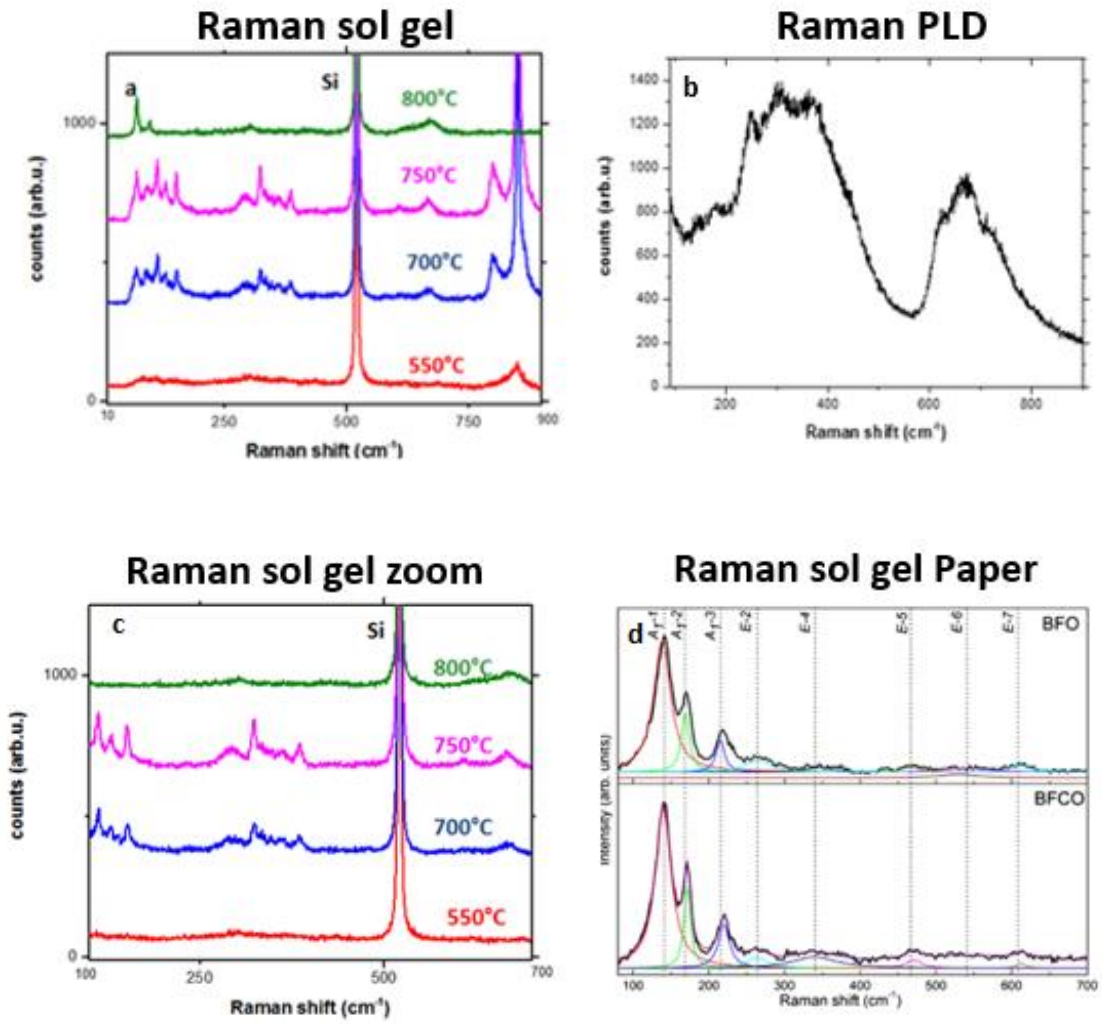

Fig.3.5: (a) Raman spectra taken from BFCO films deposited on silicon at different Temperatures; (b) Raman spectra obtained for BFCO deposited by PLD (chapt.4); (c) Zoom in the zone 100-700 cm^{-1} of the Raman made on sol-gel samples (d) Raman spectra of $BiFeO_3$ and $BiFe_{0.97}Cr_{0.03}O_3$ published by Yin et al.[17]

The Raman analysis of our samples confirm somehow the XRD results and the results from above. At 550 °C the reaction has still not taken place, so that no BFCO phase is formed; at 700 and 750 °C the BFO and BFCO phases are present (peak around 100 cm^{-1}). Yet, the presence of several peaks, which have not been identified at this stage, can probably be attributed to the formation of several other phases than the BFO and BFCO ones. The peaks in the film annealed at 750 °C are more intense in respect to the ones at 700 °C; this is a confirmation that the reaction has gone to completion, as suggested from TGA analysis. At

800 °C, the degradation reaction took place in the film and only low intensity peaks are present in the Raman spectra.

b) Optical properties of the films

To determine the optical properties of the BFCO sol gel films, the solutions were spun on quartz substrates. Prior to deposition, the substrates were cleaned in a bath of H_2O/HF (10:1) for 90 s in order to eliminate any trace of compounds on the surface that could alter the coating. Optical absorption spectra of the films annealed at 700°C and 800°C are shown in figure 3.6. A huge difference between the two absorption spectra is found. For BFCO annealed at 700 °C, a shoulder appears at a wavelength of about ≈400 nm. Nechache et al.[18] have attributed this behaviour to charge transfer excitation between Cr and Fe mixed *d* orbital Hubbard transitions that occur in ordered regions of the sample. This suggestion agrees with the spin-density functional theory calculations which has been demonstrated by the absorption spectra of the similar double perovskite La_2FeCrO_6 [19]. Though this effect is still not well understood, it can be considered as a good proof of the formation of a BFCO phase in the film annealed at 700 °C. This corroborated since by the fact that the feature is not anymore visible at 800 °C, temperature at which no BFCO phase is expected to be formed.

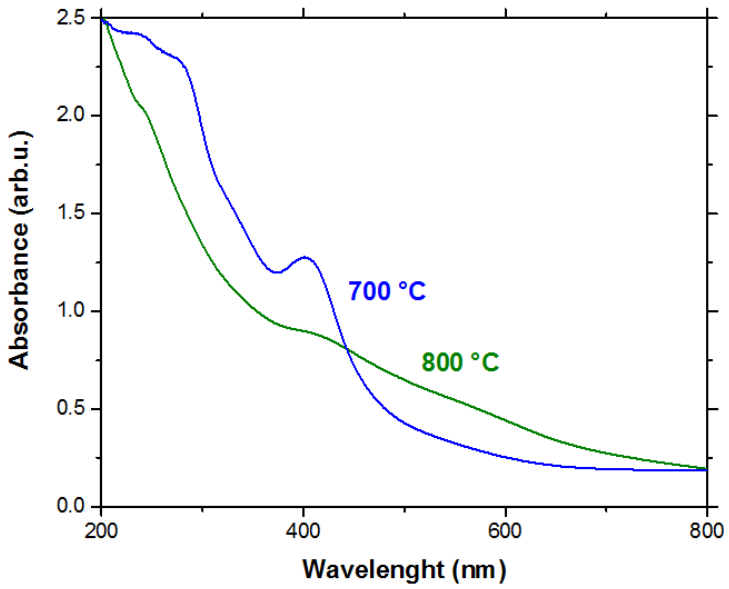

Fig.3.6: Absorption spectra of BFCO deposited at room temperature by sol gel on Quartz substrate and annealed at 700 °C (blue) and 800 °C (green) for 90 nm thick samples.

The absorption spectra were also used to extract the materials bandgap. The Tauc plot [20] method was used for this purpose. The coefficient α has been calculated following the steps:

$A = \log (I_o/I)$ *(eq. 1) and*

$I = I_o e^{\alpha L}$ *(eq.2) that gives:*

$\alpha = 2.303\ (A/L)$ *(eq.3)*

Where A is the Absorption of the film, I the intensity of the transmitted light, I_O the initial intensity and L the optical path.

The plot is shown in Figure 3.7 for the sample annealed at 700°C. The bandgap of the grown film was extracted taking in consideration the direct permitted transition for BFCO[18]. The linearization of the curve allowed to extract two bandgaps of 2.64 eV and 3.14 eV. The bandgap of 2.64 eV is close to that of $BiFeO_3$ (BFO) and $BiCrO_3$ (BCO) as reported by Nechache et al.[18]. The higher bandgap is speculated to be related to BFCO. Indeed, Pignolet et al.[21] has notified that a high bandgap can be related to a disordered phase of BFCO, in which Fe and Cr cations are randomly distributed at the B sites of the simple perovskite structure, corresponding to a solid solution of two perovskites, namely BFO and BCO. Thus, the high extracted bandgap (around 3 eV)[18] can be explained.

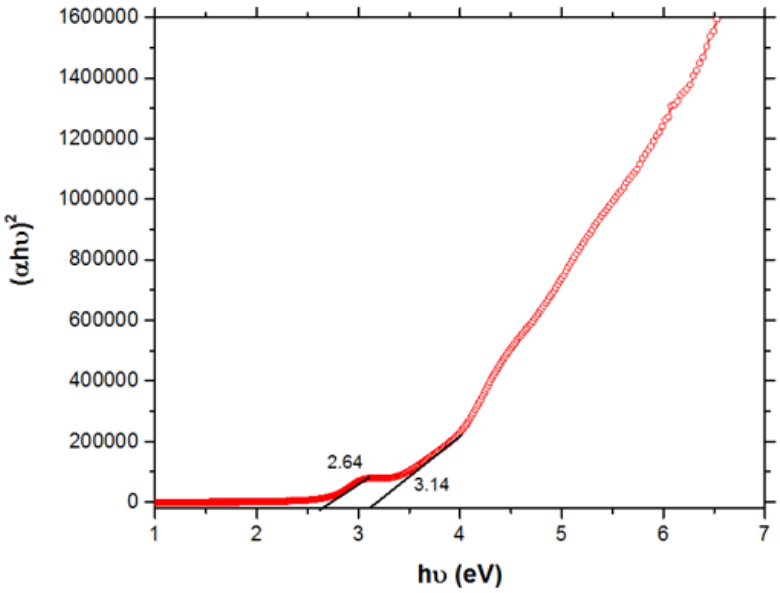

Fig.3.7: Tauc Plot of Direct allowed transition for BFCO deposited at 700 °C.

c) Morphology properties of the films

The films prepared at 550 °C and at 700 °C on silicon were observed by Scanning Electron Microscopy (SEM) (fig 3.10). The images were taken both in topography and composition mode. It is interesting to notice that the film annealed at 550 °C presents different cracks on the surface. This effect can be explained as a consequence of fresh layers of sol-gel solution will lose about 60% of their weight and high volume reduction. This weight loss can occur only from the top surface, while the volume reduction produces cracked surface as it can be seen on dry clay sediments. In contrast, the surface of the film annealed at 700 °C is flat and does not present large grains which is good news for a future application in photovoltaics, as presence of cracks would generate short-circuits. In the composition mode, the SEM tool differentiates between the different phases (which indicate different oxide compounds in our case) thanks to a scale of grey. Thus, dark grains are related to low atomic weight elements (iron and chromium) while bright grains are a signature of high atomic weight elements (e.g. Bismuth).

In the SEM image in composition mode of the film annealed at 550 °C, the scale of grey indicates different average atomic weights, which can suggest the presence of different phases in the film which can be related to bismuth oxide (well identified in the XRD spectra) and also the presence of iron and chromium oxides, as the BFCO compound is not formed yet. The interpretation is more complex for the film annealed at 700 °C, since the reaction of phase formation has started, so that many phases are present in the film, which are not only related to simple metal oxides but also to BFO, BCO, BFCO with different stoichiometry.

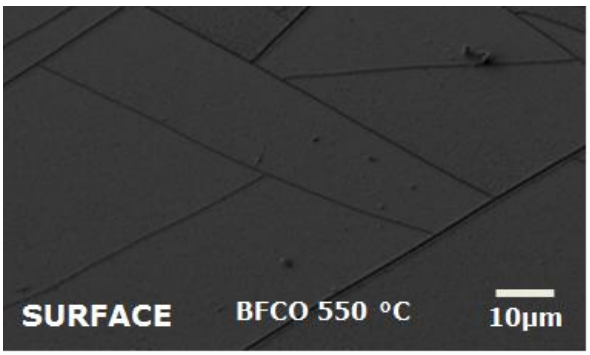

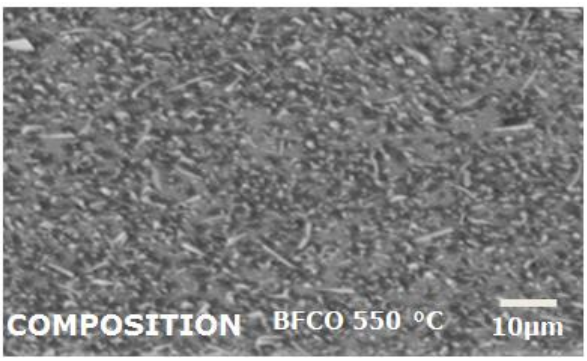

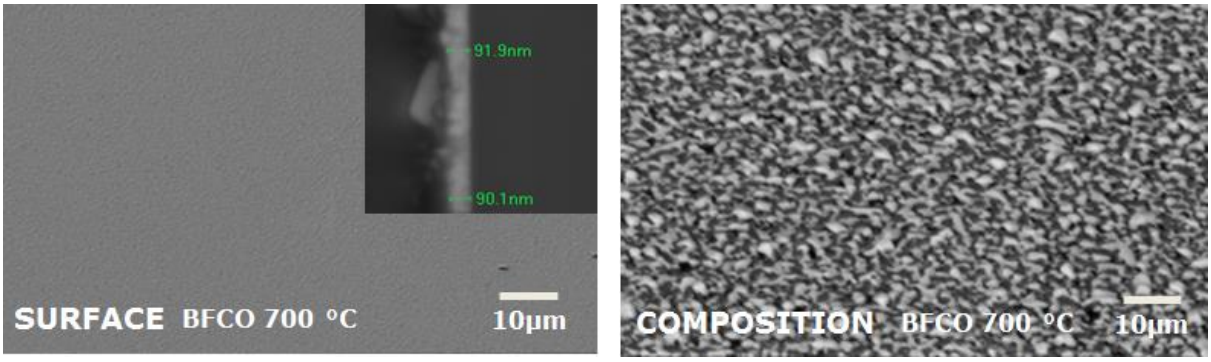

Fig.3.8: SEM analysis for BFCO films heated at 550 °C and 700 °C

Rutherford Backscattering Spectrometry analysis was carried out on the BFCO films heated at 550 °C and 700 °C. The purpose is to identify the composition of the films and to quantify the content. The extracted data of the $Bi_xFe_yCr_zO_t$ composition are given in Table 3.2. It is found that although the bismuth was used in an excess of 10%, its high volatility conducted to a bismuth' deficiency in both films. The same effect is observed for the chromium and iron elements. Oxygen is usually difficult to detect accurately with RBS method. Yet, the measured data shows a high oxygen intrusion during the reaction for both samples.

RBS	Bi	Cr	Fe	O
550	1.7 (2)	0.7 (1)	0.6 (1)	12 (6)
700	1.8 (2)	0.8 (1)	0.6 (1)	13 (6)

Table 3.2: Composition of the $Bi_xFe_yCr_zO_t$ films heated at 550 °C and 700 °C. In the brackets is indicated the expected value.

d) Reproducibility

In order to confirm the reproducibility of the experiments, a new solution of BFCO was prepared by sol gel technique and deposited on silicon substrates or quartz. Figure 3.9 compares the diffraction spectra of the sol-gel BFCO films as prepared from the first solution (blue) and from the second one (orange), deposited on silicon substrates and heated at 700°C. The XRD signatures are quite similar for the two solutions, meaning that the structural quality of the films is the same. On the other hand, Figure 3.10 exhibits the absorbance spectra of the former and new sol-gel BFCO films as deposited on quartz and heated at 700 °C. Despite a slight difference in the absolute absorbance values for the UV wavelengths, the two spectra match very well and both exhibit a bump at about 400nm. The slight variation in the

absorbance can be attributed to a difference in thickness of the films upon deposition and annealing.

From these results, we can be confident about the reproducibility of the sol-gel BFCO films.

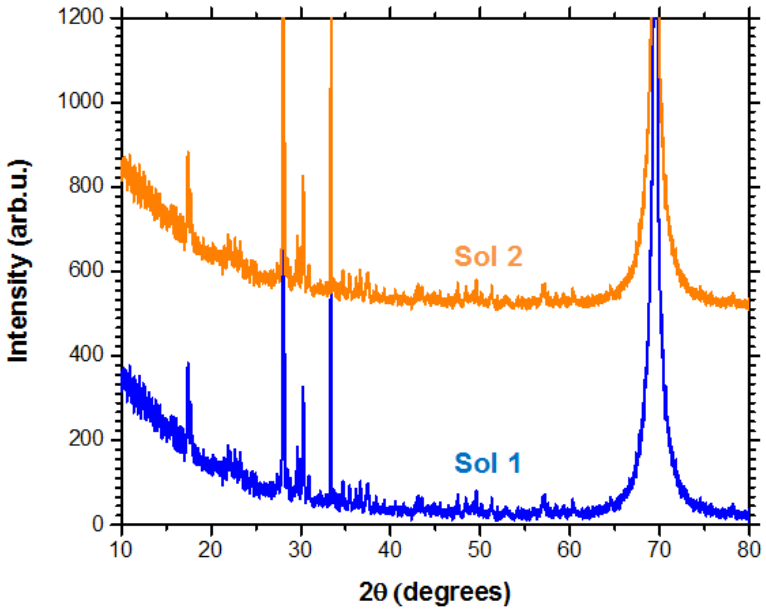

Fig.3.9: XRD spectra of BFCO deposited by sol gel and heated at 700 °C with the first solution (blue) and the second one (orange)

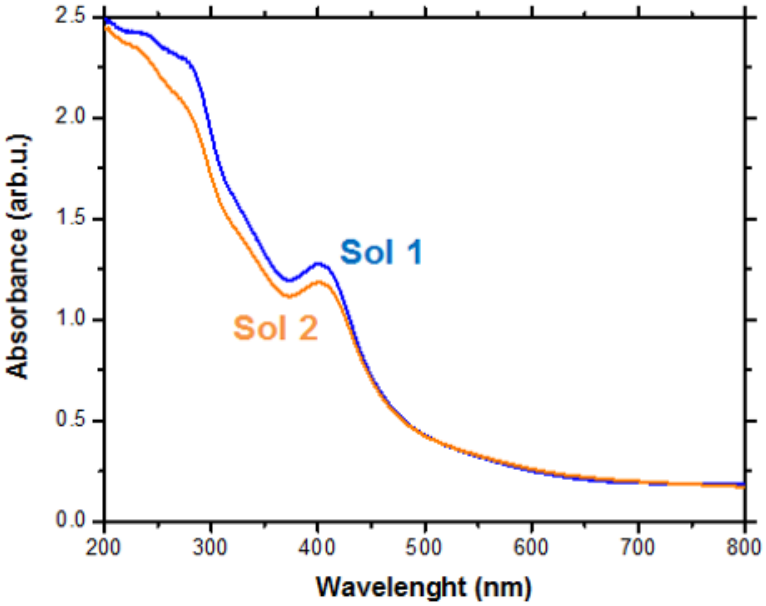

Fig.3.10: Absorption spectra of BFCO deposited at room temperature by sol gel on Quartz substrate and annealed at 700 °C by the first solution (blue) and the second one (orange)

3.3.3. RTA of sol gel BFCO films

a) Films preparation

The Rapid Thermal Annealing (RTA) process uses several halogen lamps as a heating source. It is characterized by a thermal profile consisting of a high heating rate (up to 150°C/s), a short plateau time (<120 sec) and a high cooling down rate (about 80°C/s). The annealing is carried out under an N_2/O_2 ambient. Table 3.3 presents the experimental conditions of the RTA process as applied to our sol-gel BFCO films prepared from different solutions : BFCO with the right stoichiometry, BFCO with an excess of iron and BFCO with an excess of chromium. All films consist in deposition of 2 layers on the silicon substrate. Each layer was spun at 2000 rpm for 60 s and sintered at 350 °C for 10 min in air. After deposition, the films were annealed by RTA for 120 s at 750 °C under different ambients.

Samples	Formula	Temperature (°C)	N2/O2	Time [RTA](s)	Layers	Substrates
RTA 08	Bi_2FeCrO_6	750	80/20	120	2	Si
RTA 09	$Bi_2Fe_{1.1}Cr_{0.9}O_6$	750	80/20	120	2	Si
RTA 10	$Bi_2Fe_{0.9}Cr_{1.1}O_6$	750	80/20	120	2	Si
RTA 11	Bi_2FeCrO_6	750	70/30	120	2	Si
RTA 12	$Bi_2Fe_{1.1}Cr_{0.9}O_6$	750	70/30	120	2	Si
RTA 13	$Bi_2Fe_{0.9}Cr_{1.1}O_6$	750	70/30	120	2	Si

Table 3.3: BFCO samples deposited by sol gel heated by RTA

a) Structural properties

The XRD measurements were recorded using the equipment D8 (Bruker) which is usually used for powders. In order to protect the detector, the signal of silicon was cutted. Figure 3.11 shows the XRD spectra of the samples deposited under N_2/O_2 : 80/20.

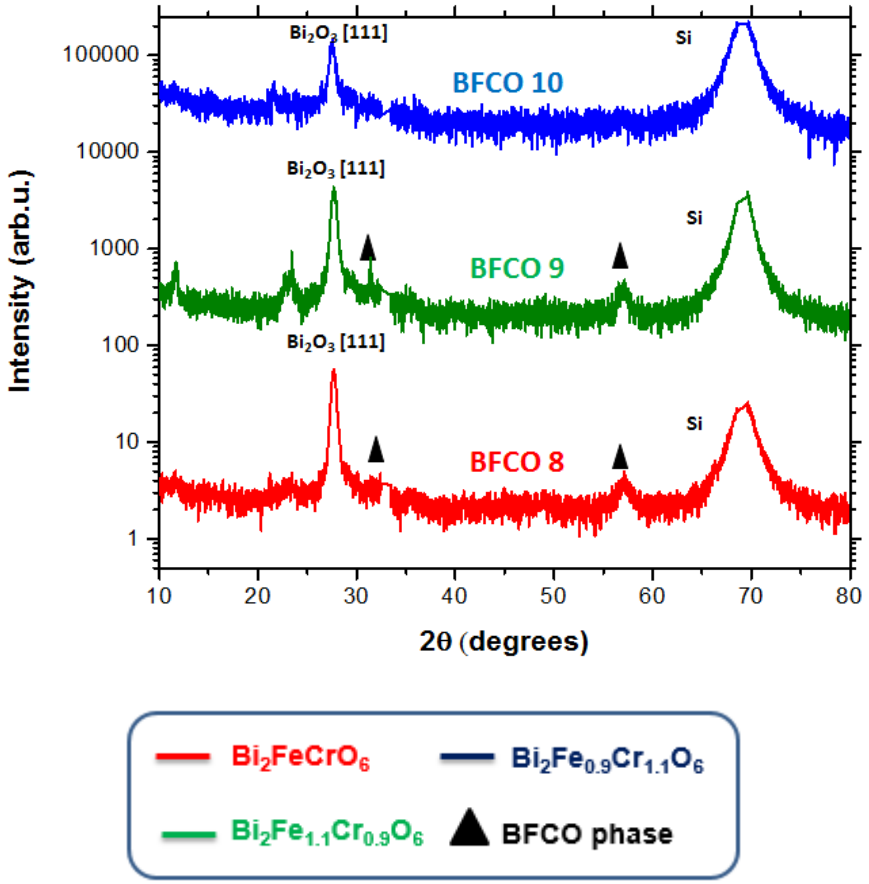

Fig.3.11: XRD spectra taken for BFCO films with different stoichiometry deposited under N2/O2 70/30 heated by RTA

In the figure, the triangles underline the positions of the phase of BFCO. The phase of Bi_2O_3 is found for all samples. For sample BFCO 8 which has Fe=Cr=1, the XRD presents only the phase of BFCO and bismuth oxide. For sample BFCO 9 with Fe/Cr= 1,2, the phase of bismuth oxide is well identified as the one of BFCO; other non identified phases are present as well. As for sample BFCO10 that has an excess of Chromium (Fe/Cr= 0.82), only the phase of bismuth oxide is visible.

For additional investigations, RBS analysis were performed on these samples. Figure 3.12 plots the experimental spectra and the modeled (simulation) one. The last considers a film of Bi_2FeCrO_6 of 200 nm free of defect on the surface

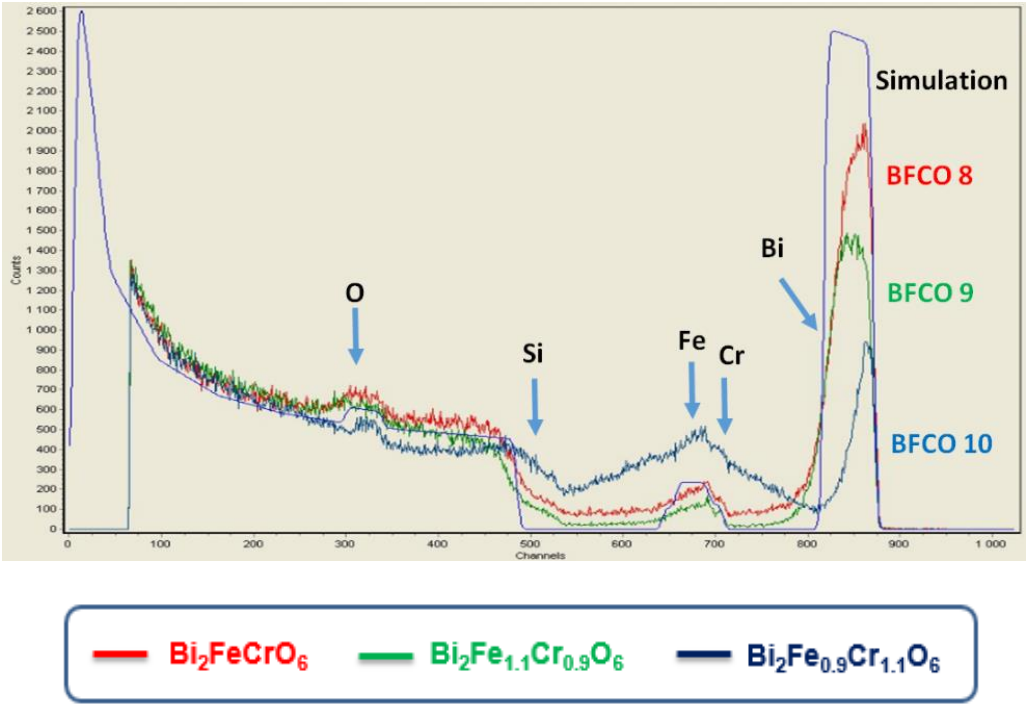

Fig.3.12: RBS spectra recorded for sol-gel BFCO films with different stoichiometry deposited under N_2/O_2: 80/20 heated by RTA

Thanks to their respective energy losses, the different elements in the compound BFCO were identified for each sample. The peak of Bismuth is well assigned between channel 800 and 900, while the presence of Iron and Chromium is forseen between channels 650 and 700.

It is found that Bi, Fe and Cr concentrations change drastically from a sample to another. Sample BFCO 8 contains a high concentration of Bi compared to the others and the concentrations of iron and Chromium are close to the theoretical values. Sample BFCO 9 exhibits a lower concentration of Bi but more uniformely distributed while the concentration of iron and Chromium are below the expected theoretical values. Sample BFCO 10 shows a lower concentration of Bi but well present mainly at the surface of the film while Fe and Cr concentrations are higher than those for the other samples. Such behaviour is not explained yet. While the excess of Cr can be understood, it is not clear why Bi has accumulated at the surface and there is much less in the film, and why more Fe is decteted in the sample. Additional analysis should be carried out, and especially using deposition on substrates such as FTO to avoid contamination by silicon from the substrate. Complementary analysis will be needed to further understand the complexity of the crystal.

A new set of sol-gel BFCO samples was prepared and RTA annealed under a higher flow of oxygen than above, namely N_2/O_2 : 70/30. The X-Ray Diffractions of these samples were recorded using Rigaku X-Ray Diffractometer (Bruker) with a source of Cu α : 0.154 nm. The spectra are shown in Fig 3.13:

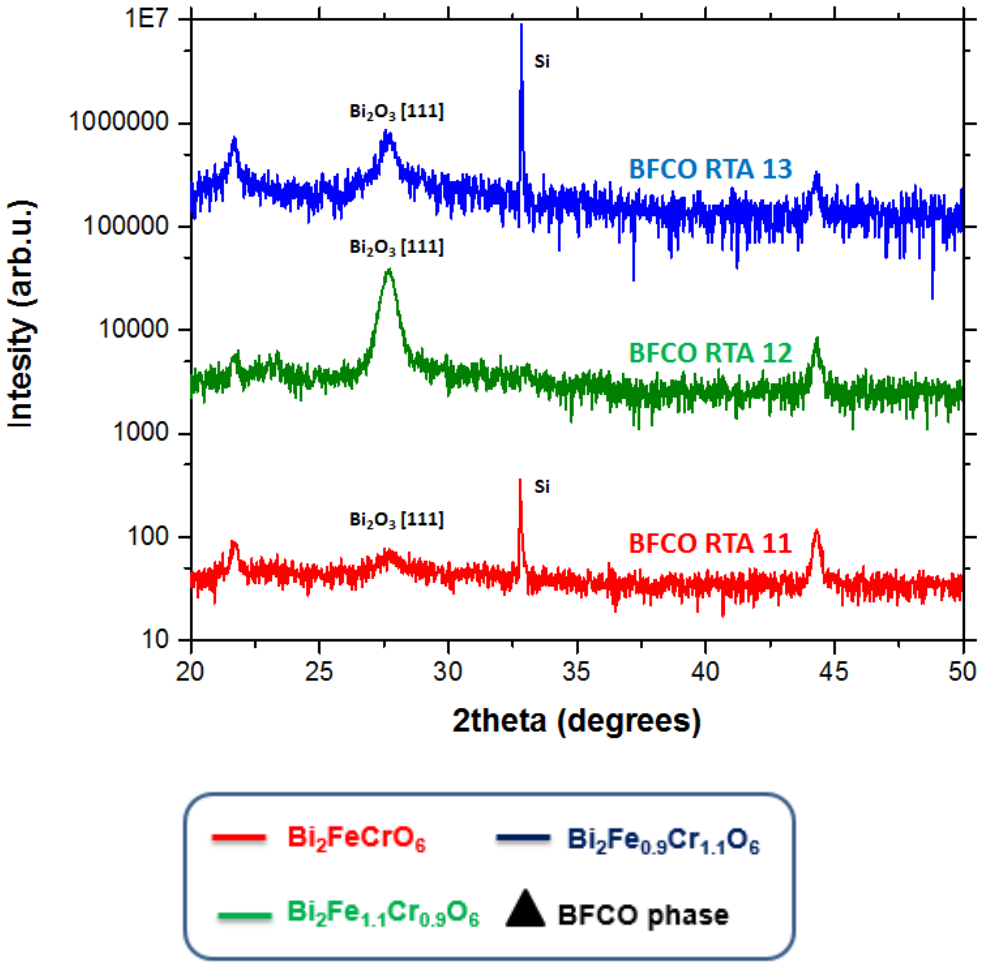

Fig.3.13: XRD spectra taken for BFCO films with different stoichiometry and annealed by RTA under N2/O2: 70/30

The XRD data show that the annealing under stronger oxidizing atmosphere inhibits the formation of a BFCO phase in the samples and results rather in the formation of the Bismuth oxide phase and other 1-2 phases which are most probably oxide compounds of iron or chromium.

3.4. Conclusions

In this chapter, we present our investigations attempting to synthesize BFCO films with a single phase using the sol-gel method. First, TGA analysis carried out on BFCO powders has shown that the reaction which forms BFCO phase starts at 640 °C and end at 750 °C. Lower annealing temperatures do not allow the formation of the double perovskite while higher thermal treatments lead to low quality products. In a second step, BFCO films were deposited from sol-gel solutions and thermally annealed in conventional (CTA) or lamps assisted (RTA) furnaces.

We have shown that heating the BFCO films in a CTA furnace led to uniform deposited films but also to the presence of too many phases as witnessed by XRD and SEM analysis. The determination of a bandgap value of the films which is found to be closer to the one of BFO confirms that it is still challenging to obtain a single phase BFCO material by sol-gel/CTA method.

We have also performed RTA on sol-gel BFCO films grown in different conditions of composition. Although some conditions such as those of samples BFCO 8 and BFCO 9 has revealed some proportion of BFCO single phase, most of the layers contains parasitic phases, in particular the Bismuth oxide phase. The presence of Bismuth Oxide within the films could be in principle detrimental to the fabrication of a photovoltaic device as it can influence the conduction of the material. Yet, as far as it is not a ferroelectric compound, it should not lower the multiferroic properties of the double perovskite.

References of chapter 3

1. Lisnevskaya, I. V., Bobrova, I. A. & Lupeiko, T. G. Synthesis of yttrium iron garnet from a gel based on polyvinyl alcohol. *Russ. J. Inorg. Chem.* **60,** 437–441 (2015).
2. Lisnevskaya, I. V., Bobrova, I. A., Petrova, A. V. & Lupeiko, T. G. Low-temperature sol-gel synthesis of modified nickel ferrite. *Russ. J. Inorg. Chem.* **57,** 474–477 (2012).
3. Yan, S., Yin, J. & Zhou, E. Study on the synthesis of NiZnCu ferrite nanoparticles by PVA sol?gel method and their magnetic properties. *J. Alloys Compd.* **450,** 417–420 (2008).
4. Shobana, M. K., Sankar, S. & Rajendran, V. Structural and thermal studies of Ni0.25Mn0.75Fe2O4 composites by sol–gel combustion method. *J. Alloys Compd.* **472,** 421–424 (2009).
5. Mesilov, V. V. *et al.* Valence states of iron ions in nanostructured yttrium iron garnet Y3Fe5O12 studied by means of soft X-ray absorption spectroscopy. *J. Electron Spectrosc. Relat. Phenom.* **185,** 598–601 (2012).
6. Lisnevskaya, I. V., Lupeiko, T. G. & Bikyashev, E. A. Synthesis of multiferroics BiFe0.5B0.5O3. *Russ. J. Inorg. Chem.* **60,** 140–146 (2015).
7. Speranskaya, E. I., Skorikov, V. M., Rode, E. Y. & Terekhova, V. A. The phase diagram of the system bismuth oxide-ferric oxide. *Bull. Acad. Sci. USSR Div. Chem. Sci.* **14,** 873–874 (1965).
8. Maître, A., François, M. & Gachon, J. C. Experimental study of the Bi2O3-Fe2O3 pseudo-binary system. *J. Phase Equilibria Diffus.* **25,** 59–67 (2004).
9. Morozov, M. I., Lomanova, N. A. & Gusarov, V. V. Specific Features of $BiFeO_3$ Formation in a Mixture of Bismuth(III) and Iron(III) Oxides. *Russ. J. Gen. Chem.* **73,** 1676–1680 (2003).
10. Koizumi, H., Niizeki, N. & Ikeda, T. An X-Ray Study on Bi_2O_3-Fe_2O_3 System. *Jpn. J. Appl. Phys.* **3,** 495–496 (1964).
11. Lisnevskaya, I. V. & Petrova, A. V. Low-temperature synthesis of the multiferroic compound BiFeO3. *Inorg. Mater.* **45,** 930–934 (2009).
12. Chen, F. *et al.* Sol-gel derived multiferroic BiFeO3 ceramics with large polarization and weak ferromagnetism. *Appl. Phys. Lett.* **89,** 092910 (2006).
13. Ghosh, S., Dasgupta, S., Sen, A. & Maiti, H. S. Low temperature synthesis of bismuth ferrite nanoparticles by a ferrioxalate precursor method. *Mater. Res. Bull.* **40,** 2073–2079 (2005).
14. Chen, Y. Z. *et al.* A high-mobility two-dimensional electron gas at the spinel/perovskite interface of γ-Al2O3/SrTiO3. *Nat. Commun.* **4,** 1371 (2013).
15. Kumar, M., Yadav, K. L. & Varma, G. D. Large magnetization and weak polarization in sol?gel derived BiFeO3 ceramics. *Mater. Lett.* **62,** 1159–1161 (2008).
16. Murari, N. M. *et al.* Structural, electrical, and magnetic properties of chemical solution deposited Bi(Fe0.95Cr0.05)O3 thin films on platinized silicon substrates. *J. Appl. Phys.* **105,** 084110 (2009).
17. Yin, L., Liu, W., Tan, G. & Ren, H. Two-Phase Coexistence and Multiferroic Properties of Cr-Doped BiFeO3 Thin Films. *J. Supercond. Nov. Magn.* **27,** 2765–2772 (2014).
18. Nechache, R. *et al.* Bandgap tuning of multiferroic oxide solar cells. *Nat. Photonics* **9,** 61–67 (2014).
19. Andreasson, J. *et al.* Electron-lattice interactions in the perovskite LaFe 0.5 Cr 0.5 O 3 characterized by optical spectroscopy and LDA + U calculations. *Phys. Rev. B* **80,** (2009).
20. Tauc, J. Optical properties and electronic structure of amorphous Ge and Si. *Mater. Res. Bull.* **3,** 37–46 (1968).

21. Nechache, R., Harnagea, C. & Pignolet, A. Multiferroic properties—structure relationships in epitaxial Bi_2FeCrO_6 thin films: recent developments. *J. Phys. Condens. Matter* **24,** 096001 (2012).

Chapter 4.

Properties of BFCO grown by the Pulsed Laser Deposition Technique

Pulsed Laser Deposition (PLD) is one of the most used technique [1–3] for the epitaxial growth of inorganic oxide. PLD is employed to deposit different materials on various substrates which give birth to ordered films that show many interesting properties, from super-conduction[4–6] to magnetism[7–9]; In particular, several works already reported the possibility to deposit inorganic perovskites by PLD in order to obtain Ferroelectric films [10–12] and which exhibit the BPVE effect. In the case of BFO, the substrate of choice is normally $SrTiO_3$ (STO) and Nb:STO (NBSTO) thanks to the matching of their lattices and helps the epitaxial growth. On the other hand, BFCO films were reported to exhibit an epitaxial growth on STO and NBSTO substrates[13,14] . Although with very limited studies, ferroelectricity and photovoltaic effects were shown for BFCO films made by PLD[15,16].

In this chapter, we will report extensively on the growth of BFCO films by PLD. We will present the operational parameters which tune the oxides bandgap. We will show how the variation of the bandgap can be related to the degree of order within the crystal. This will be confirmed by theoretical modelling. We will also investigate the charges transport within the BFCO grown films, and in particular will show how it is be possible to modulate the current by playing with the memory of the polarization. Finally, we will present the performances of our BFCO based solar cells and will discuss the potentials and limitations of such devices.

4.1 Experimental procedure

Several BFCO films were grown by Pulsed Laser Deposition (PLD) on $SrTiO_3$ (STO) and 0.5% doped Nb:$SrTiO_3$ (NbSTO) (001) oriented-substrates. The pellet for the ablation was prepared by the solid-state method starting from the powder of Bismuth, Chromium and Iron Oxides. The powder was first mixed in right amount (stoichiometric quantity of Chromium and Iron oxides; a 10% excess of Bismuth oxides was added in order to compensate the Bismuth loss during the deposition due to its volatility. In order to produce the pellet, we proceed to a standard sintering procedure. The mixture was first pre-calcined at 800 °C for 12h; afterwards it was grounded down and calcined at 820 °C for 24h. The fine powder obtained has been

pressed into a pellet and heated at 840 °C for 24 hours. The pellet was found to be 83% of the theoretical density of the material. The pellet was afterwards aligned in front of a STO substrate in a PLD system and a vacuum of 10^{-7}-10^{-8} mbar was obtained with a turbomolecular pump.

The films were deposited using a KrF laser (248nm) with an energy of 26 mJ (corresponding in our technique to a fluency of 1,03 J/cm^2 for a laser spot of 2 mm^2) obtained with an attenuator. We adjusted the oxygen partial pressure, the deposition temperature, the laser fluence and the laser repetition rate in order to optimize the films for our application. In order to get a uniform deposition, the carousel on which the substrate was positioned was rotating during the experiment. After deposition, the samples were cooled down at 5 °C/min in oxygen atmosphere.

X-Ray Diffraction (XRD) and X-Ray Reflectivity (XRR) measurements were performed by means of a Rigaku SmartLab diffractometer equipped with a monochromatic source (Ge(220x2) delivering a $CuK_{\alpha 1}$ incident beam (45 kV, 200 mA, λ=0.154056 nm), in order to determine with accuracy phase purity, crystallite size and film thickness. Absorption measurements were obtained by a Perkin Elmer Lambda 950 UV/Vis Spectrometer while the optical bandgaps were extracted from spectroscopic ellipsometry (Horiba Uvisel) measurements. For the last, the dispersion model used is Adachi-New Fourouhi [17]. The magnetic properties were analyzed at room temperature using a MPMS SQUID-VSM (Quantum Design) magnetometer allowing a maximum field of 7 T. Piezoresponse Force Microscopy (PFM) measurements were performed on a Bruker Icon QNM using a 0.01-0.025 Ohm-cm Antimony (n) doped Si covered with conductive Diamond and a.c. voltage at 20 kHz.

4.2. Effects of the deposition conditions on structural properties

The experimental parameters for depositing the films were the temperature, the oxygen partial pressure and the laser energy. In the following, the properties of the grown films are reported versus the deposition parameters. The main purpose is to identify the best operational conditions to obtain an epitaxial BFCO film, without secondary phases.

4.2.1. Deposition Temperature

The BFCO films were first grown at a fixed Oxygen partial pressure of 10^{-2}mbar, a laser Energy of 26 mJ repetition rate of 10Hz, while varying the temperature. The deposition was carried out at 680, 750, and 800 °C. The XRD spectra of the BFCO grown films versus deposition temperature are shown in fig. 4.1. The BFCO films presents an epitaxial growth on STO only

for the temperatures equal or higher than 750 °C. At 680°C, the formation of secondary phases (bands at around 27°) is obvious and can be linked to oxygen deficient structures.

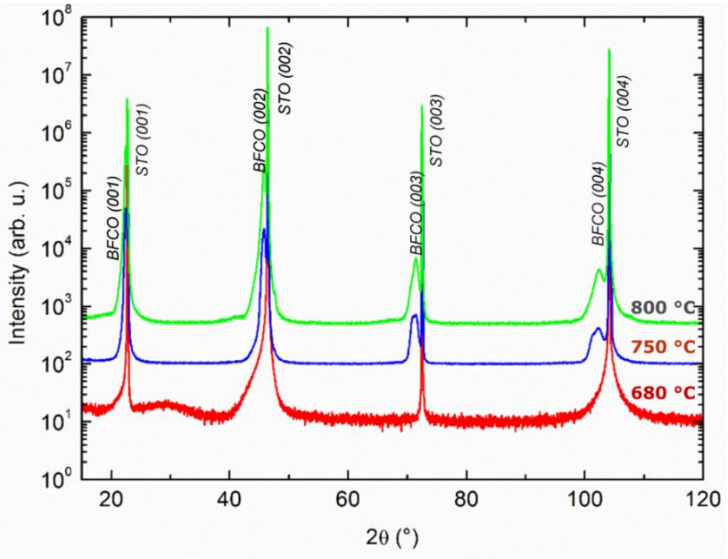

Fig.4.1.XRD of BFCO deposited at different Temperatures

4.2.2. Oxygen partial pressure

For this set of samples, the deposition was carried out at fixed temperature of 750 °C, a laser repetition rate of 10 Hz, a laser energy of 26 mJ and at two different pressures in the deposition chamber, namely 10^{-2} (black in fig.4.4.) and 10^{-3} mbar (red in fig.4.2.). For samples made with a pressure of 10^{-3} mbar, a secondary phase peak appears around 27° (black triangle in fig.4.2). Given this result, we fixed our deposition oxygen partial pressure to 10^{-2}mbar.

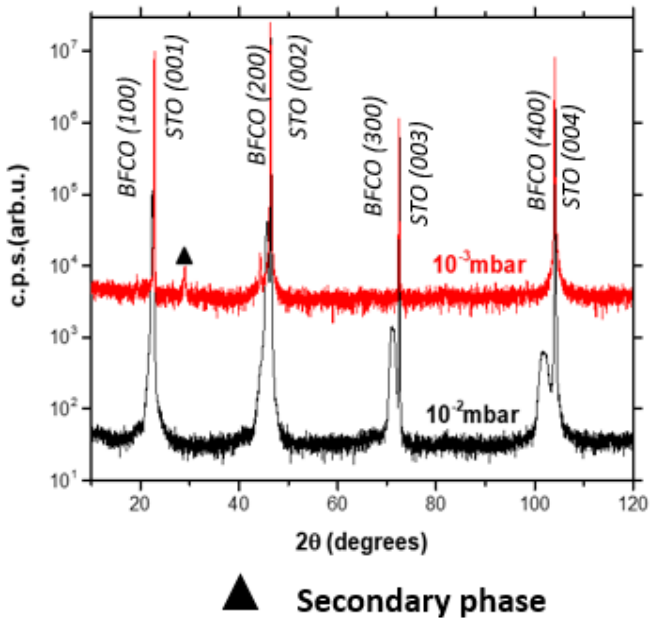

Fig.4.2.XRD of BFCO deposited at 10^{-2} and 10^{-3} mbar

4.2.3. Laser Energy

In order to check the effect of laser fluency on the growth of BFCO films, we performed PLD deposition by varying the laser energy at 20mJ, 26mJ and 40mJ. The results of the XRD analysis of the grow films are reported in figure 4.5. At the lower laser energy (20 mJ, 1,0 J/cm^2), the signature of the phase of BFCO is weak; In contrast, the phase at 27,5°, already seen in fig.4.2, is appearing together with a small peak at 57°. At 26 mJ, BFCO phase is present and no other phases are visible within the detection limits of our instrument. By increasing the laser energy (40 mJ, 2.0 J/cm^2), the phase at 27,5° is even higher than for 20 mJ case and in addition the peak at 57° is more clear and another phase around 30° is present. Further analysis on this phase should be performed to characterize it properly. From Figure 4.3, the best condition seems to be the BFCO deposition at 26 mJ.

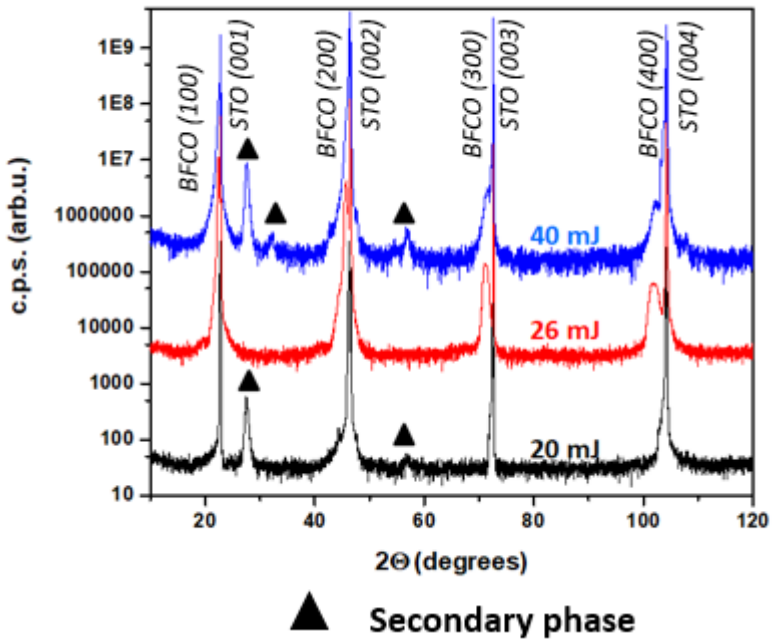

Figure 4.3. Θ-2θ scan of BFCO deposited by PLD at 20, 26 and 40 mJ

4.2.4. Laser repetition rate

Figure 4.4 shows θ-2θ scans for PLD deposited BFCO films on STO at different laser repetition rates. The rest of the parameters are fixed: laser energy 26 mJ, chamber pressure 10^{-2} mbar, temperature 750 °C. Only the pseudo-cubic phase of BFCO and the (00l) peaks of the substrate (STO) are present. The BFCO peaks are close to the one of STO which is explained by the close lattice parameters between the film (0.3930 nm) and the substrate (0.3906 nm). These were intentionally chosen in order to have a good epitaxial growth of BFCO on STO. These patterns also suggest that the films are grown epitaxially with out-of-plane (OP) lattice parameter c of the BFCO pseudo cubic phase oriented along the normal to the surface of the STO substrate. No secondary phases could be observed within the resolution limit of the X-ray diffraction technique.

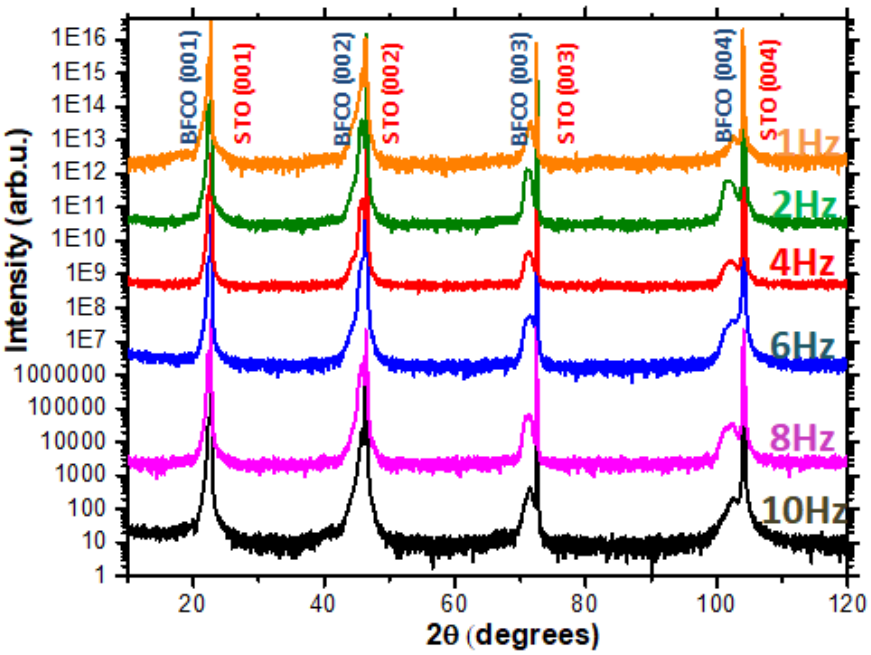

Figure 4.4. Θ-2θ scan of BFCO deposited by PLD for different repetition rates ranging from 10 Hz to 1 Hz.

The observed pseudo-cubic indexes are justified by the structure of the double-perovskite

In order to confirm the epitaxial growth of the BFCO film, a Φ scan was recorded along the (111) direction of STO and BFCO deposited at 2Hz (fig.4.6.a). It shows a cube on cube geometry without any other phase around the direction. Subsequently, we focused our attention on the atomic order of the two cations (Fe and Cr) inside the double perovskite structure. A θ-2θ measurements were carried out along the pseudo-cubic [111] BFCO direction (which is the direction growth of the double perovskite) by tilting the sample of 54.7° (fig.4.6.b). From the last, superstructures peaks (SP) are clearly identified at 19.6° and 61.2°, which can be a proof of chemical ordering of BFCO, that means Fe and Cr planes stacking along the [111] direction. It should be noticed that although it is known that superstructures peaks are characteristics of the presence of cation ordering inside the double perovskite, these peaks can also have another origin that can be cationic displacements which is common in ferroelectric oxides. [18].

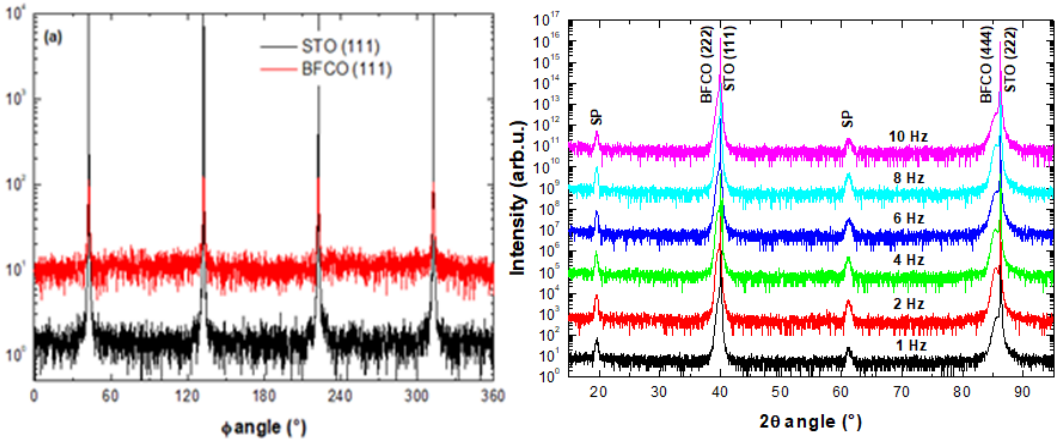

Figure 4.6. a) Φ scan of BFCO along the [111] direction b) θ-2θ scan of BFCO along the axis [111]

The thickness of the grown films at different laser repetition rate was estimated by X-Ray reflectivity (XRR) while the vertical and lateral coherence length were obtained by the θ-2θ (shown in fig.4.4) and rocking curves. The results are shown in fig.4.7. It is observed an increase of the thickness of the film when lowering the repetition rate. It should be noticed that the film grown at 1Hz was deposited at 7500 shots, instead of 30.000 otherwise the deposition duration would have been extremely long (around 8h). As a consequence, the thickness of this 1Hz film does not match with that of the others. The films do not present a columnar growth and show a lower concentration of defects as the repetition rate increases. Fig 4.7 also shows that the vertical correlation growth (or crystallite size, calculated by the Debye-Scherrer formula) is decreasing while the thickness decreases. Note that the crystallite size is always much smaller than the thickness. Another feature to notice is that the lateral correlation length is larger for thinner films. These results suggest that even if the film grows epitaxially on the substrate, it does not present a columnar growth mode and a larger number of defects is present in the film as the deposition frequency increases. Moreover, it is possible to assume that the substrate induces a strain into the films which starts to relax at higher thicknesses.

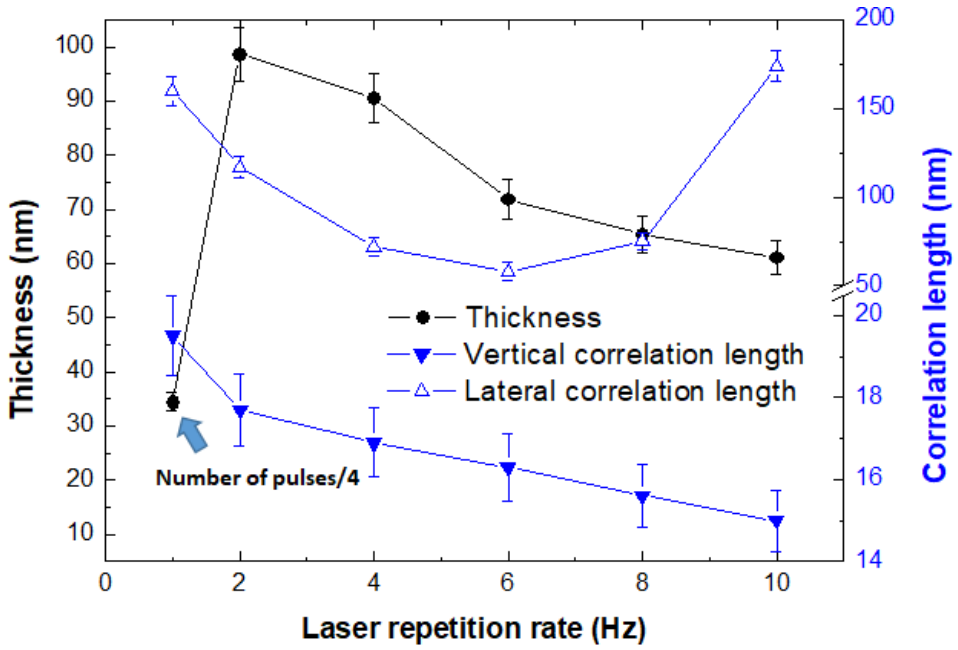

Fig.4.7. Variation of film thickness, vertical correlation length and lateral correlation length as extracted from reflectivity, θ-2θ and rocking curve X-ray diffraction measurements respectively.

In order to confirm the effect of the laser repetition rate on the deposition, we performed new deposition at a lower temperature, namely at 680 °C. The XRD spectra are shown in figure 4.8. No clear difference is observed between the two conditions. We can therefore consider that the repetition rate has the same effect on the sample whatever is the deposition temperature.

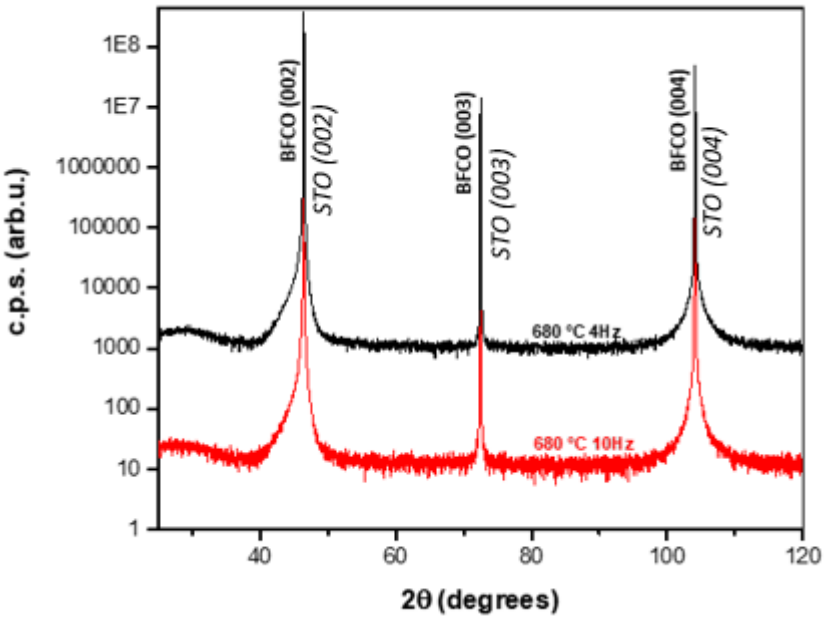

Fig.4.8.XRD of BFCO films at different frequencies.

The bandgap values of the BFCO films grow by PLD were extracted from ellipsometry measurements and fitting models. The results are showed in fig.4.9. The figures of merit related to chi-squared values were always better than 0.2. It should be noticed that the chi-squared is a value to measure the goodness of the fit. In ellipsometry experiment, a value $\chi^2 <$ 0.5 is considered a good fit. It is found that the bandgap increases from 1.9 to 2.6 eV when the deposition rate increases from 1 to 10 Hz while the crystallite size increases up to 6Hz and then slightly decreases. This observed effect has been already reported [13] and has been explained as Jahn-Teller distortion of the structure, taking advantage of the inverse relation between deposition rate and crystallite size in this type of materials. In this way, the distance between the atom B', B" and the Oxygen in the double perovskite are modified allowing us to engineer parameters like, for example, the bandgap and consequently the absorption of the material. Another effect that can produce changes in bandgap is the presence of defects in the material. The anti-site defect, which have been already introduced in chapter 2, can be usually identified by X-ray data. The defects concentration is proportional to the ratio of the intensity of the superstructure peak (I_{sp}) and the main peak ($I_{(222)}$ or $I_{(444)}$) of the double perovskite. Notice from fig.4.6.b that the (222) peak of BFCO is very close to that of STO (111) one so we preferred to use the intensity of the BFCO (444) peak in order to have a better

estimation. Fig.4.9 reports the variation of the ratio I_{sp}/I_{444} versus the laser repetietion rate calculated from figure 4.6 (zoomed in the inset fig.4.9).

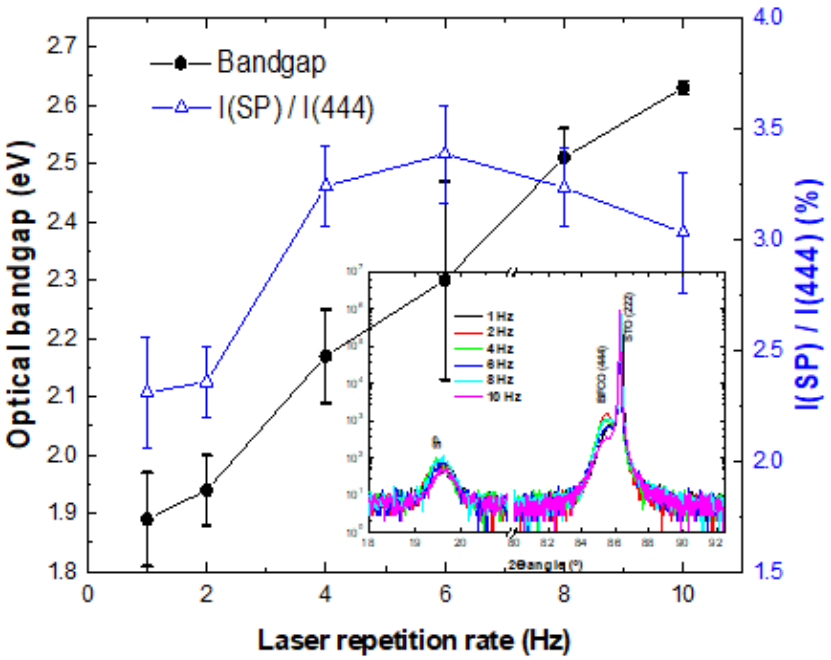

Fig.4.9. Bandgap variation with the laser repetition rate. The values are defined as the ratio between the intensity of the superstructure peak (SP) and the (444) peak of BFCO (zoomed in the inset)

Surprisingly, not a clear evolution is found for the ratio I_{sp}/I_{444} with increasing the repetition rate. This effect can be explained by suggestions taken from Shabadi[18] which reports that the SP of the structure are not a reliable factor of merit of Fe/Cr ordering as Fe and Cr have low scattering contrasts. Moreover, as already discussed in chapter 2, a higher value of ΔZ, where Z is the chemical valence, is known to bring order to the structure. It is therefore acceptable to conclude that an ordering in the structure should be accompanied by a change in the valence from Fe^{3+}/ Cr^{3+} to Fe^{2+}/ Cr^{4+}. Since the XRD analysis did not help that much to rise insights regarding the ordering within the crystal, we investigate the magnetic properties of the grown films. In fact, as discussed in chapter 2, cationic disorder inside the double perovskite should reduce strongly the magnetization because of antiferromagnetic interactions (Fe-O-Fe and Cr-O-Cr) appearing in the system. Fig.4.10 gives the magnetization loops as recorded for Bi_2FeCrO_6 films at room temperature and laser repetition rates of 2, 6 and 10 Hz.

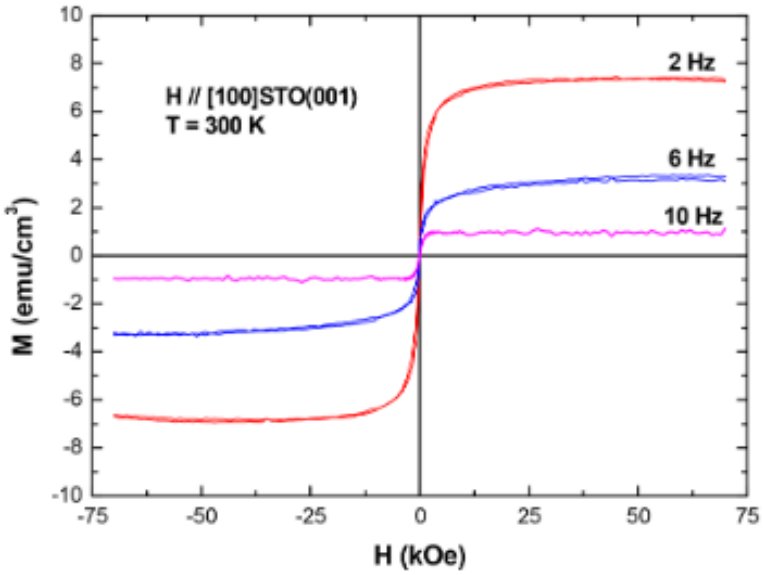

Fig.4.10 Room Temperature magnetization loop recorded for BFCO deposited at 2, 6, and 10 Hz.

Is it possible to notice that in our samples the magnetization (below 10 emu/cm^3, ≈ 0.12 μ_B) is much smaller than the one expected by other reported films (≈ 150 emu/cm^3) [19]. As discussed above, as a lowering in magnetization is related to a lower order in the crystal, we can make two assumption:

- Increasing the repetition rate lowers the ordering in our samples;
- Our samples present a low ordering degree.

We have shown how the increment of the repetition rate was related to an increment of the bandgap so we supposed that there should have been a correlation between disorder structure and bandgap change which allows a proper engineering of the bandgap by changing the repetition rate of deposition.

4.2.5. Thickness effect

BFCO films were deposited by PLD by varying the number of laser shots. For this series, the other parameters were kept constant: oxygen pressure of 10^{-2} mbar, a deposition temperature of 750°C, a laser energy of 26 mJ and a frequency of 2Hz. A larger number of shots is expected to give rise to thicker films. The θ-2θ spectra of the grown BFCO samples are shown in fig.4.11. It should be noticed that for the film of 7.5 nm, the phase of BFCO is visible only in the most intense peak, which is the (200) one. It is possible to notice a "shoulder" which identify the BFFCO phase.

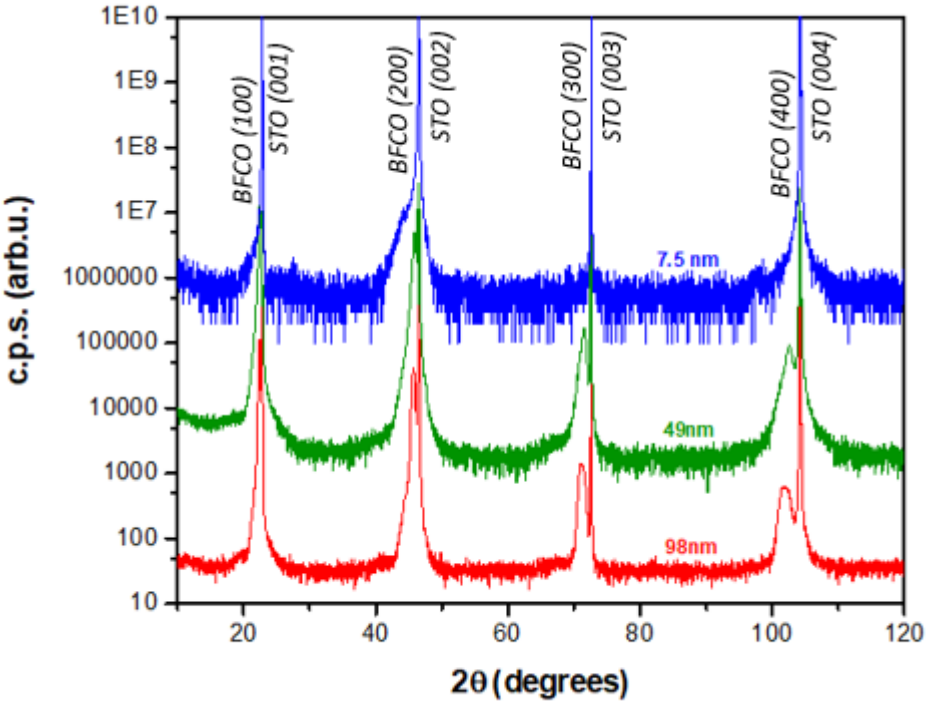

Figure 4.11. θ-2θ scan of BFCO films 98 (black), 49 (red) and 7.5 (blue) nm thick

We found that the crystal structure is not varying with the thickness. Especially we were able to reach an epitaxial growth along the axis (001) even for the 7.5 nm thick film. The XRD spectra clearly show the presence of the BFCO even though the intensity of the peak is reduced for the low thickness of the film. The aim of reducing the thickness is to obtain more conductive films. On the other hand, thinner films present a reduced absorption as shown in fig; 4.12. ±

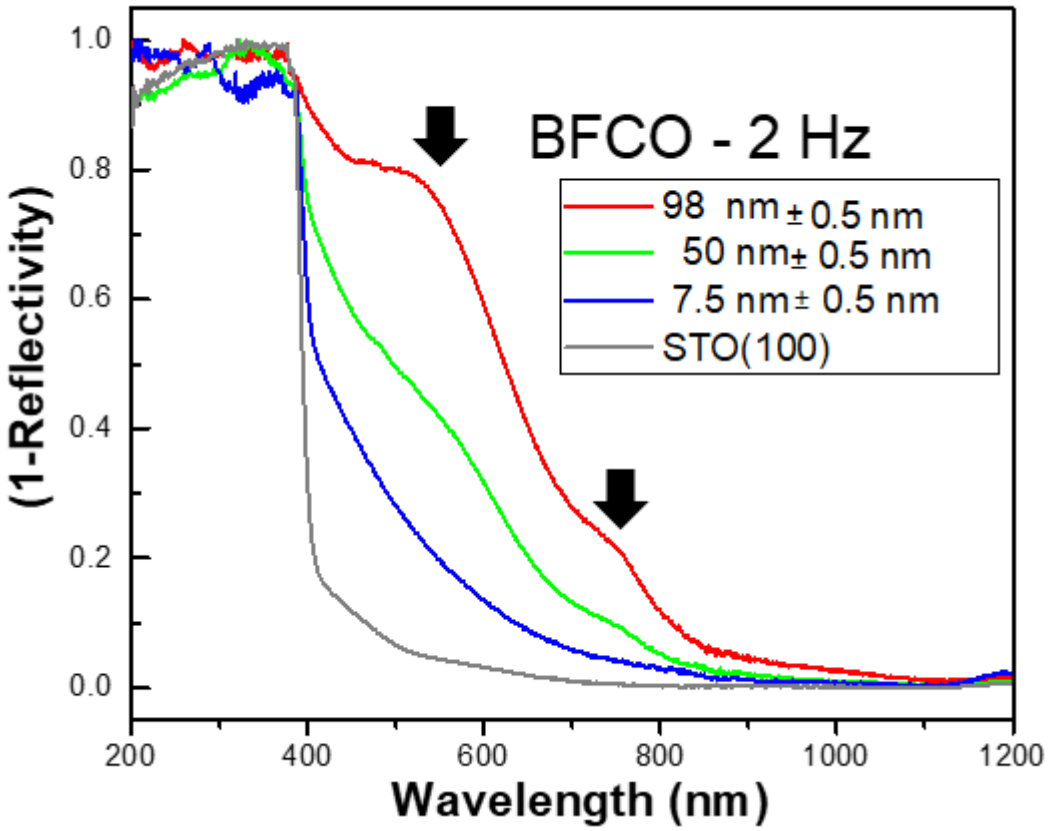

Fig.4.12: Normalized optical absorption spectra for 3 different thickness BFCO films. The flashes indicates the double peaked shape

In the figure, we plotted (1-Reflectivity) versus wavelength. The BFCO films were grown on STO substrates which inhibits to properly measure the transmittance. It is important to underline that a reduced absorption, which translates in a reduced number of light photons interacting within the film, affects directly the number of electron/holes couple formed and therefore generates a reduced photovoltaic current. There is a compromise to be found for thin films as they offer a high conductivity on one hand but a lower generation of electrons on the other hand. A trade-off is therefore mandatory. From fig.4.12 we can also notice the "double peaked" shape of the absorption curve for the 100 nm thick film. The same behaviour is still visible at 50 nm while it disappears at 7.5 nm. This effect can be linked to an electronic exchange between Fe and Cr in the crystal, as discussed in chapter 2, or to ordered and disordered zones in the crystal which have different bandgaps as we will discuss later on in this chapter.

4.3. AB Initio Calculations for the Order effect

To get more insight on the ordering effect within the structure and it is correlation with the electronic bandgap of the BFCO grown films, ab initio calculations were performed thanks to the collaboration with D. Stoeffler at CNRS-IPCMS. We adopted the R3 symmetry as previous reported work[20,21], which corresponds to a space group 146 for the BFCO unit cell. The primitive cell of BFCO was built starting from the trigonal cell of the $BiFeO_3$ (fig.4.13.a) in order to construct a trigonal cell as shown in fig.4.13.b which is used for full relaxation calculation. Starting from it we built the hexagonal cell (Fig.4.13.c) which contains three BFCO formula units with three Fe and three Cr sites (fig.4.13.d). This cell was used for modelling chemical configurations with exchanged Fe and Cr atoms and allows building three "disordered" configurations.

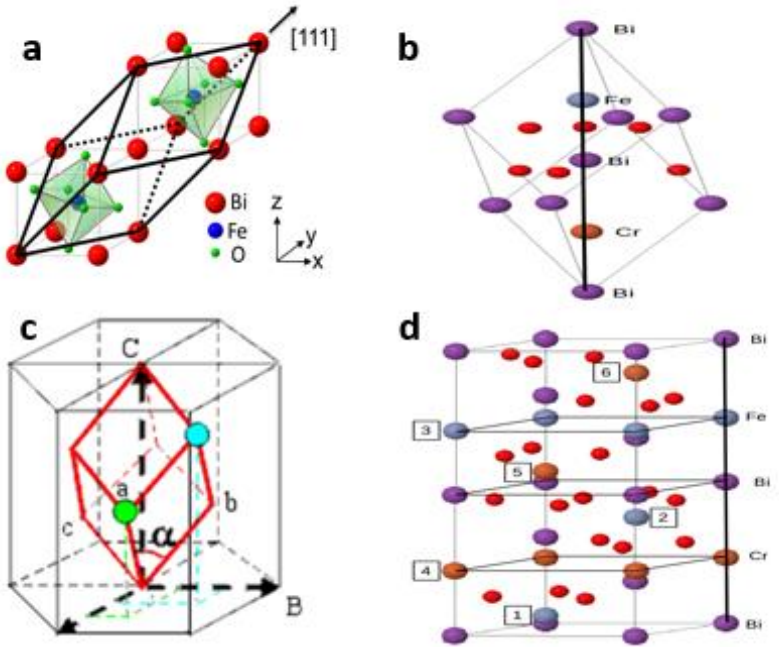

Figure 4.13. a**)** trigonal structure of BFO; b) trigonal structure of BFCO; c) from trigonal to hexagonal cell for BFCO; d) hexagonal cell containing 3 primitive BFCO cells

All calculations were performed using the Vienna Ab initio Simulation Package (VASP 5.4) [22,23]allowing accurate determination of the electronic structure and investigation of the magnetic properties of the considered system. It uses the so-called augmented plane waves and it is based on the projector augmented wave (PAW)[24] method using pseudopotentials to determine the wave function outside the augmentation region.

The HSE06 function[25,26] is used in order to extract the bandgap from the calculation without having to play with empirical parameters as in the GGA+U approach[27,28]. Moreover, we have checked that the bandgap obtained with the HSE06 function is recovered with the GGA+U method with so large U_{eff} values (around 7 eV) that the electronic structure is strongly distorted. All calculations are performed with a cutoff energy of 400 eV and k-point samplings of 4x4x4 for the trigonal cell and 5x5x2 for the hexagonal cell. After full relaxation, the lattice parameters and the internal structural positions of each atom were extracted and the values are reported in Table 4.2.

Atom	Coordinate	value
Bi1	**(x=y=z)**	**0**
Bi2	**(x=y=z)**	**0.4966**
Fe	**(x=y=z)**	**0.2253**
Cr	**(x=y=z)**	**0.7194**
O1	**(x,y,z) (z,y,x) (y,z,x)**	**(0.4010,0.5367,0.9395)**
O2	**(x,y,z) (z,y,x) (y,z,x)**	**(0.0353,0.8938,0.4419)**

Table.4.2. Structural data at reduced coordinates of the R3 symmetry of BFCO trigonal unit cell with a = 0.55135nm and α = 59.821°, obtained from the full relaxation calculation.

By building the hexagonal unit cells, we kept the atomic position fixed regardless the site of Fe and Cr was occupied by a Fe or a Cr atom. We built the "perfectly ordered" structure by using a hexagonal cell where Fe occupies the Fe site and Cr occupies the Cr site. In this way, the cell presents an alternate configuration of Fe and Cr (0001) planes. We then used the notation FCFCFC where F and C correspond to Fe and Cr (0001) planes in the stacking respectively. We have built three other slightly disordered configurations which are CFFCFC, FFCCFC and FFFCCC. The ordered configuration as well as the three disordered ones are presented in fig.4.14.

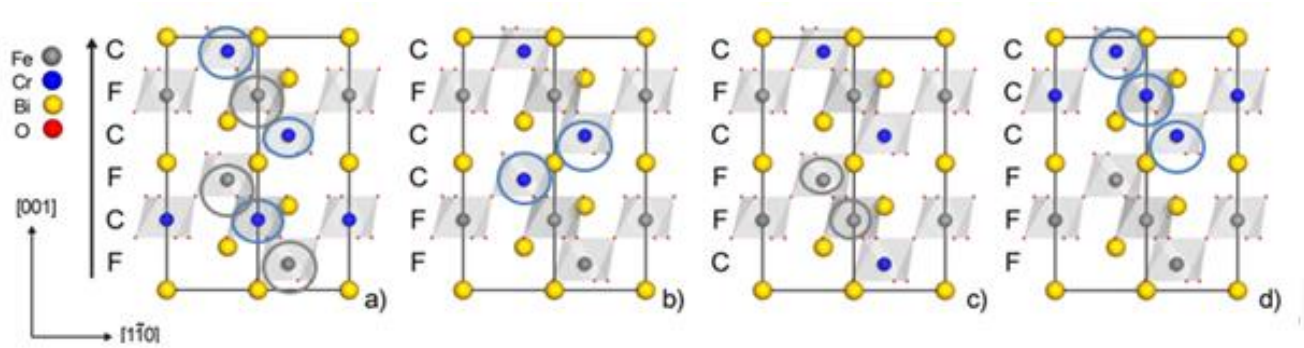

Figure 4.14. a) Ideal "fully ordered" and b-d) "disordered" crystalline structure used for ab initio calculation. "F" and "C" stands for Fe and Cr atomic planes respectively. The black lines represent the hexagonal unit cell.

The projected Density of States (DOS) of the total Fe and Cr atoms for the fully ordered and the three disordered configurations are displayed in fig.4.15 and 4.16, respectively.

These DOS results present several common features:

i) as HSE 06 was used, the results got affected by a strong localization which makes the Fe occupied energy states ranging always between -8 and -6.5 eV;

ii) the bottom of the conduction band is defined by the edged structure of the Fe unoccupied states;

iii) The range of Cr occupied states varies mainly between -1.5 and 0 eV and they are weakly hybridized with the Fe states;

iv) The minority spin energy band gap is included in the majority spin band gap.

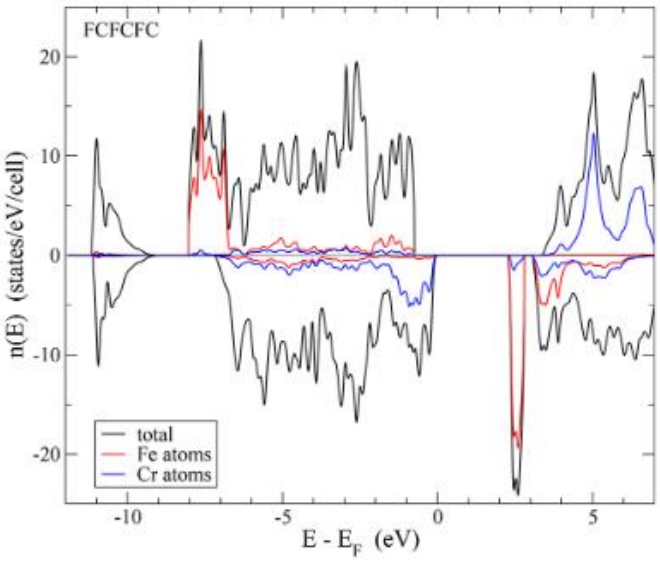

Figure 4.15. Total density of states (DOS)-Fe and Cr atoms projected-for the "perfectly ordered" configuration (FCFCFC) in the hexagonal cell. Positive and negative DOS corresponds to majority and minority spin states respectively.

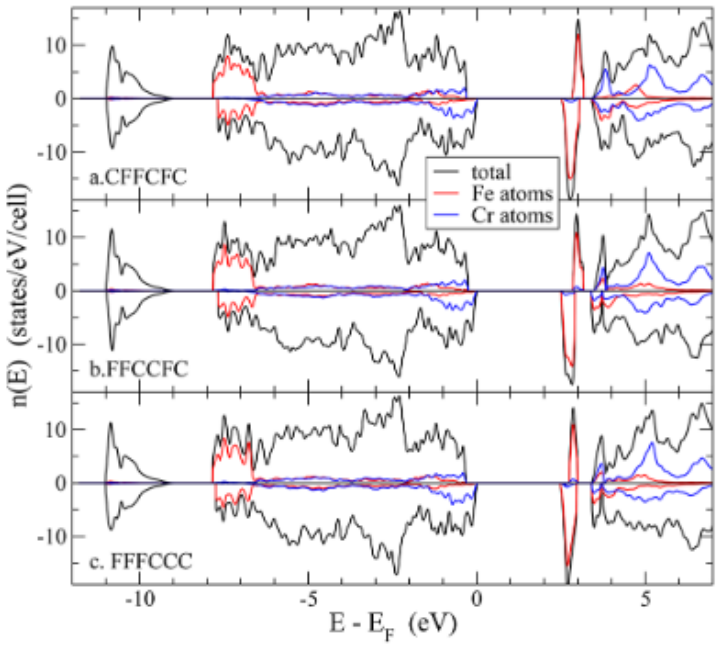

Figure 4.16. Total density of states (DOS)-Fe and Cr atoms projected-for the three "disordered" configuration in the hexagonal cell. Positive and negative DOS corresponds to majority and minority spin states respectively.

For the "perfectly ordered" configuration, which has the lowest total energy among all four cases, with all Fe (respectively Cr) sites being occupied by Fe (Cr) atoms, they carry a positive

(negative) magnetic moment of 4.21 μB (−2.76 μB) giving a total magnetic moment per cell of 6 μB (Table 2). For the "disordered" configurations, the Fe atom on a Cr site carries a negative magnetic moment and, reciprocally, the Cr atom on a Fe site carries a positive magnetic moment, so the total magnetic moment per cell is reduced to 2 μB (Table 4.3). The sign of the magnetic moment changes from one magnetic atomic layer to the next one whatever the nature of the magnetic atom is, which indicates that only antiparallel aligned magnetic moments are obtained for neighboring Fe/Fe, Cr/Cr, and Fe/Cr atoms. These results strongly support the reduced magnetization observed in fig.4.10. It is worth noticing that each atomic layer changes the magnetic moment in respect to the other which means that each neighbouring atomic couple (Fe/Fe, Cr/Cr, Fe/Cr) is displaced antiparallel.

Configuration	Local magnetic moment (μ_B)	Eg (up)/Eg (down) (eV)
FCFCFC	4.212/-2.760/4.212/-2.760/4.212/-2.760	4.15/2.30
FFCCFC	4.212/-4.168/2.807/-2.762/4.175/-2.804	3.12/2.52
CFFCFC	2.864/-4.126/4.164/-2.805/4.176/-2.808	3.13/2.55
FFFCCC	4.212/-4.167/4.163/-2.807/2.823/-2.762	3.08/2.50

Table 4.3. Local magnetic moment of the Fe and Cr atoms considered in the different configurations and the relative bandgaps

As shown in fig.4.15-16, the minority of spin gap (Eg (down)) is entirely included in the majority one, so that the bandgap corresponds to the minority spin gap. Consequently, the ordered configuration gives a bandgap of 2.30 eV while it reaches 2.50-2.55 eV for the disordered ones. The difference in the calculated bandgap is clearly less than the one we reported above for the experimental values (Fig. 4.9). The observed difference can be explained as follows: i) in our calculation the hybridization Fe-Cr is weak, and ii) we used an hexagonal cell which allows the "disorder" only in planes perpendicular to the c direction, thus limiting the disorder degree in the model. Yet, these theoretical calculations give a good support to the experimental results.

As we have seen, the degree of disorder inside the crystal depends on the valence between Fe and Cr. We have investigated this effect by means of theoretical calculations by computing the charges carried on by each atom. First, we performed the so-called "Bader charge

analysis"[29] by using a code developed by Henkelman et al.[30,31] which uses the minimum of potential energy between two atoms to separate them and calculate their charge independently. In this case the charge brought from each atom (Fe and Cr) was nearly equal (≈ 1.9 |e| for both of them) and did not change even if the sequence F-C changed. Based on some already reported works on Fe_3O_4 and $CaFeO_3$ systems[31] , we concluded that this method is not helpful for our model. We have found a better model in the work of Wang et al[32] which calculate the charge ordering by using the Born effective charge (BEC) carried on by each atom. By using this model, we were not bounded to a defined volume as we took in account the variation of the polarization around the considered atom. We first tried to make the calculation using HSE06 functional but it was too much computer time consuming so we used the approximation GGA+U with U=4eV. We were able to properly describe the occupied states and then the charge density even if the bandgap was found to be low (i.e. 1.6eV). This effect can be related to the fact that the polarization and the Born effective charge are calculated by summing over the occupied states. Furthermore, the BEC are obtained using a linear-response approach as implemented in VASP[33] and the polarization is calculated in the framework of the modern theory of polarization.

The charges obtained for the four considered configurations are given in table.4.4.

In the "perfectly ordered" structure, the Fe BEC are found 0.80 |e| larger than the Cr ones in clear contrast with the results of the Bader charge analysis.

For the three "disordered" configurations, depending on the sequence, there are huge ΔQ^*_{zz} variations:

i) For Fe atoms in a Cr-Fe-Cr, stacking values of ΔQ^*_{zz} are found to be equal to -0.05 and -0.02 |e| while for Cr in a Fe-Cr-Fe stacking they are found to be equal to +0.01 and 0.04 |e|.

ii) For Fe atoms in Fe-Fe-Cr or Cr-Fe-Fe stacking, the values are found to be equal to -0.19,-0.20,-0.09,-0.22,-0.18 and -0.17 |e| and for Cr atoms in Cr-Cr-fe or Cr-Cr-Fe stacking they are found to be +0.43, +0.15, +0.25, +0.26, +0.25 and +0.14 |e|.

iii) Finally, for the Fe atom in a Fe-Fe-Fe stacking the values are -0.33 |e| and for Cr in Cr-Cr-Cr are +0.40 |e|.

FCFCFC	Fe	Cr	Fe	Cr	Fe	Cr
Q*zz	+3.86	+3.06	+3.86	+3.06	+3.86	+3.06
FFCCFC	**Fe**	**Fe**	**Cr**	**Cr**	**Fe**	**Cr**
Q*zz	+3.67	+3.66	+3.49	+3.21	+3.81	+3.07
Δ Q*zz	-0.19	-0.20	+0.43	+0.15	-0.05	+0.01
CFFCFC	**Cr**	**Fe**	**Fe**	**Cr**	**Fe**	**Cr**
Q*zz	+3.32	+3.77	+3.64	+3.10	+3.84	+3.31
Δ Q*zz	+0.26	-0.09	-0.22	+0.04	-0.02	+0.25
FFFCCC	**Fe**	**Fe**	**Fe**	**Cr**	**Cr**	**Cr**
Q*zz	+3.68	+3.53	+3.69	+3.31	+3.46	+3.20
Δ Q*zz	-0.18	-0.33	-0.17	+0.25	+0.40	+0.14

Table 4.4. Born Effective Charge Q*zz on the fe and Cr atoms for the four cases considered with the variation Δ Q*zz calculated relative to the same atom in the "Perfectly ordered configuration

Within this approximation, the level of disorder is well shown by varying from 0.5 |e| to 0.15 |e| by lowering the grade of "disorder" in the crystal until the value of 0.07 for the extreme case of FFFCCC. In other words, the higher the disorder, the lower the difference in the charge between Fe and Cr, which is in agreement with the rules discussed in chapter 2. It should be noticed that the polarization is not affected in this last calculation as it has been found always about 0.57 µC/cm^2.

4.4. Electrical properties of the PLD BFCO films

4.4.1. Samples preparation

In order to perform the electrical measurements, a 100 nm thick film of transparent ITO layer was sputtered at room temperature on the BFCO films, providing both good electrical conductivity and high optical transparency (figure 4.17 a). The thickness was confirmed by the XRR measurements which gives a roughness of about 2 nm. The 1x1 mm^2 area of the electrode was then contacted with a copper wire using a conductive epoxy (figure 4.17 b). The current-voltage measurements were then performed using a precision LCR Meter (Agilent E4980A).

The electrical measurements were performed on BFCO produced in the following conditions: T=750 °C, pO_2= 10^{-2} mbar, E= 26 mJ, repetition rate= 2 Hz, t=98nm

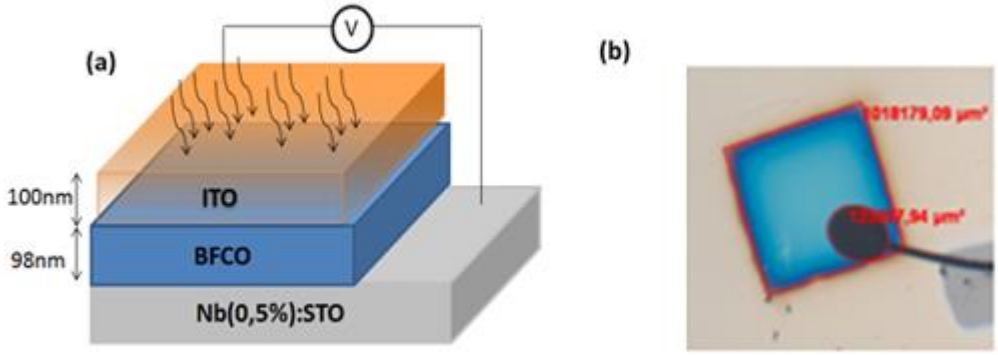

Fig.4.17: a) sketch of the Ferroelectric based device; b) zoom on the ITO contact and glued copper wire

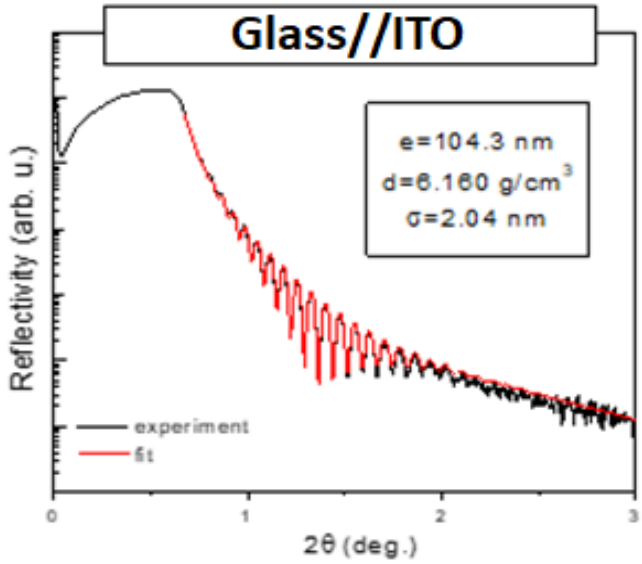

Fig.4.18: XRR measurement of the sputtered ITO. E is the thickness of the film; d is the average density while σ is the average roughness.

4.4.2. KPFM on ITO/BFCO/Nb:STO

Kelvin-Probe Force Microscopy (KPFM) measurements were used to determine the workfunctions of the film of ITO and BFCO films. These results were obtained in collaboration with the department of Materials Science and Metallurgy of the University of Cambridge. For the Nb:STO substrate, we assumed the standard values reported in literature. We used an

iridium coated Silicon point as a reference for the workfunction to measure. The results are shown in fig.4.19.

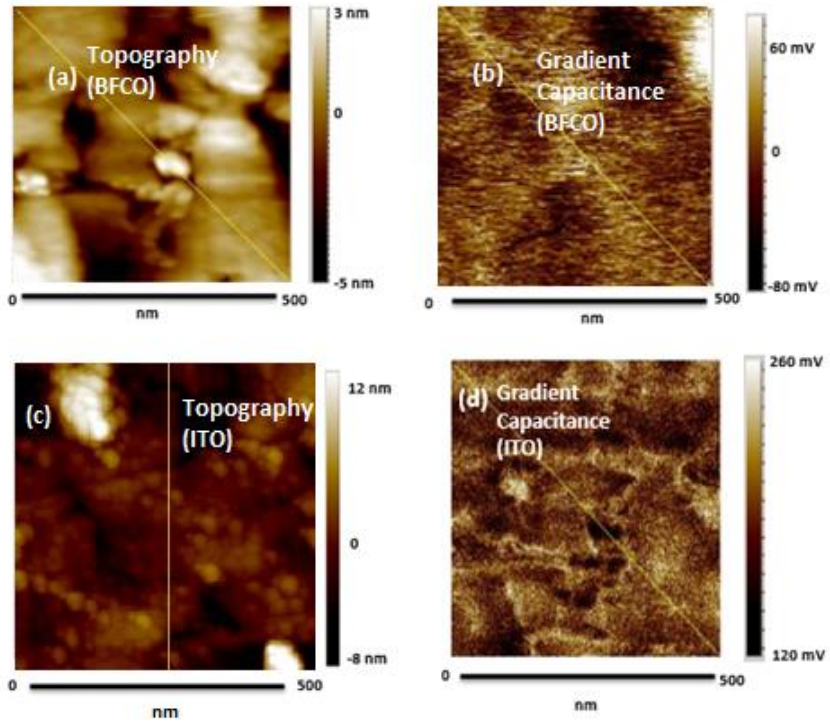

Fig.4.19: KPFM of ITO and BFCO

KPFM measurements show only a slight difference between the work functions of BFCO made at 2 Hz and that of ITO. This can be detrimental for a functioning device as such a low workfunction's difference will result in a low potential gradient between the two layers and therefore a weak charges extraction. Considering the Fermi Energy calculated by Nechache et al.[13] , we have drawn in fig.4.20 a schema of the energy levels of the device.

material	Workfunction (eV)
Nb:STO	4.100 (value from literature)
BFCO	5.445±0.001
ITO	5.465±0.001

Table 4.5: Workfunction values of the components of the BFCO based device.

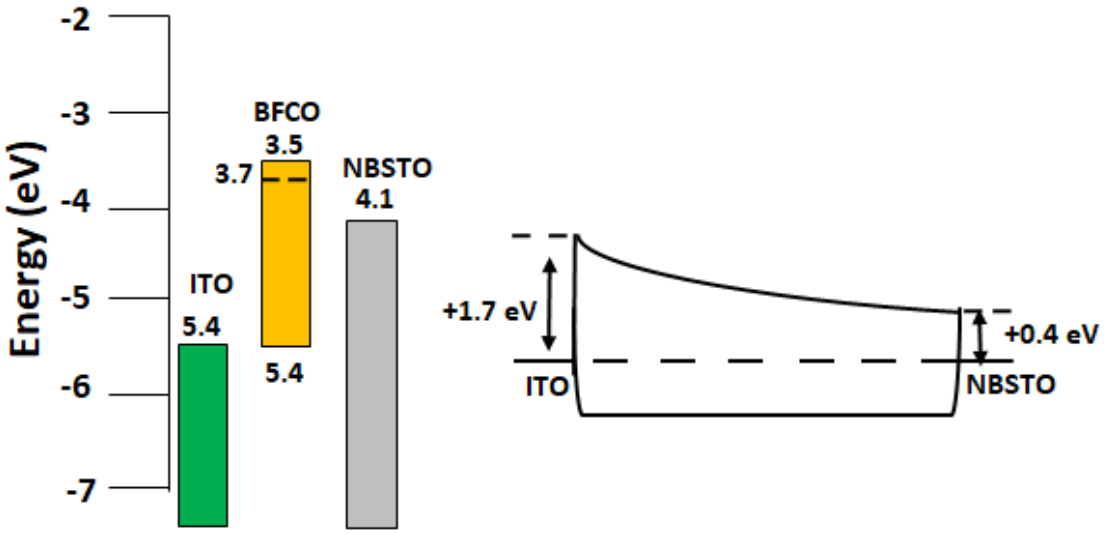

Fig.4.20. Schema of the energy levels of the device ITO/BFCO/NBSTO. The barrier formed at the interface is not able to produce an efficient electron extraction.

4.4.3. Ferroelectric properties of the PLD-BFCO films

The electrical measurements of the grown BFCO films were performed with a homemade quasi static current-voltage (I-V) tester. Figure 4.21 plots an I-V curve between -8V and 8V recorded in darkness conditions. At +6V, a clear peak originating from FE polarization reversal is clearly visible despite the high leakage contribution. This effect is more obvious in the inset of fig.4.21. It should be noticed that the ferroelectric peak does not appear for negative voltages due to a high ohmic conductivity. The FE coercive field of the order of 64 MV was extracted from the I-V characteristic, which is in a good agreement with the previous study[19]

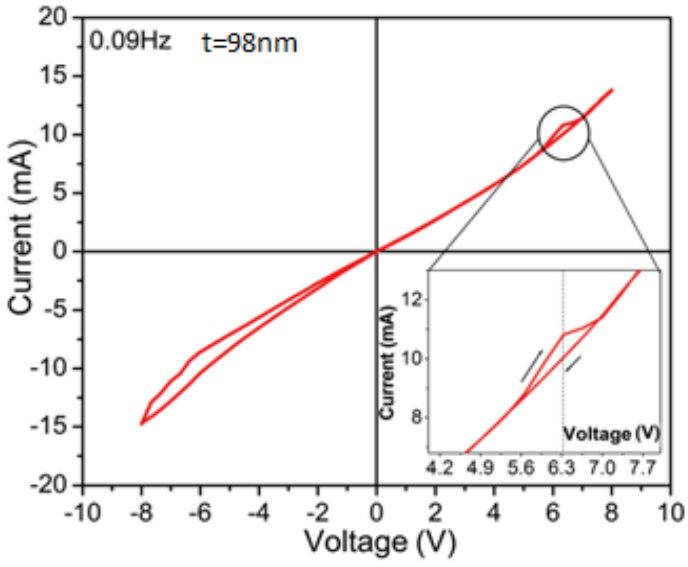

Figure 4.21: I-V loop of a Bi_2FeCrO_6 film under dark.

Subsequently, we performed capacitance-voltage measurements. Firstly, we performed the measurement in darkness (fig.4.22 a) by applying increased voltage loop each time. We started with 0/1V/-1V/1V loop (labeled as "1V" in the figure), then we made a second measure with 0/2V/-2V/2V loop (noted as "2V"). We used the same procedure for 3V and 4V. The curve of 1V is not exhibiting a ferroelectric effect since the capacitance data shows the conventional "banana loop" typical of insulating material (cf. chapter 2). As we increase the voltage, a ferroelectric shaped curve starts to appear. The effect is better visible for the 4V loop' curve especially around 4 V where the capacitance is highly increasing with a small change in the applied voltage. Since we obtained the best response at 4V, we performed the same loop under dark and under illumination using a laser radiation (fig.4.22 b). It is clear that the capacitance is enhanced under light illumination which is indicative that the generation of electro-hole pairs influences the polarization state of the BFCO sample. The capacitance is in fact related to the internal polarization due to the ferroelectric effect. An enhancement of the ferroelectricity translates into a change in the internal polarization, which can be favorable to enhance the electron/hole pair separation in the photovoltaic device

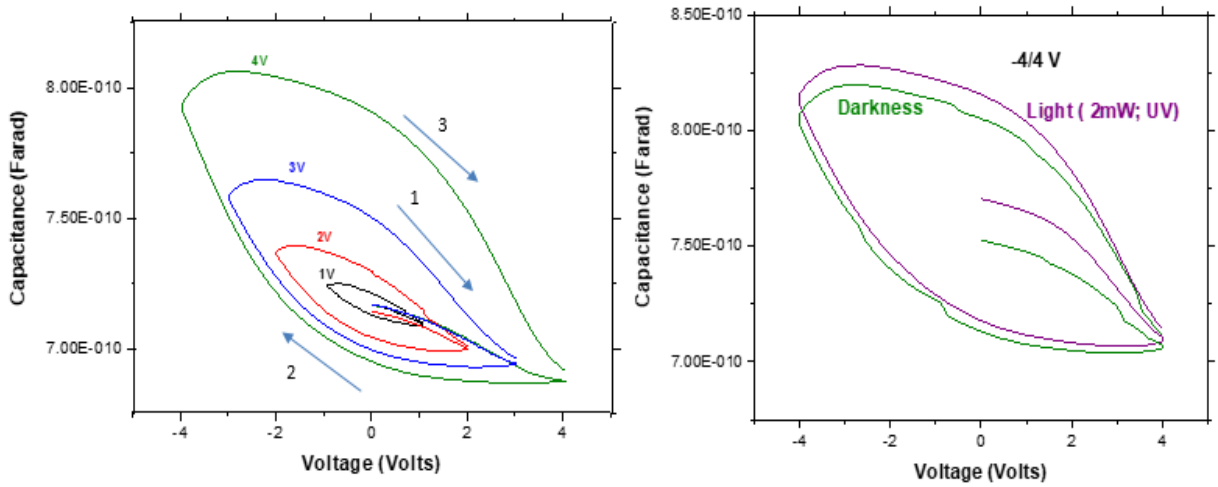

Figure 4.22: (a) C-V loop of a Bi_2FeCrO_6 film under dark at 1, 2, 3 and 4V; (b) C-V loop under dark and light at 4V

4.4.4. PFM Measurements on PLD-BFCO samples

In order to investigate more deeply the ferroelectric properties of the samples, we performed Piezoresponse Force Microscopy (PFM) measurements on BFCO/Nb:STO deposited at 2Hz, t=98nm. Figure 4.23 (a) shows that the polarization can be switched when applying an external

Voltage. Fig.4.23 (b) shows Amplitude and Phase loop characteristics of Ferroelectric behaviour. The loop is not centred at 0 V as the measurements are sensitive to different resistance and defects present in the sample.

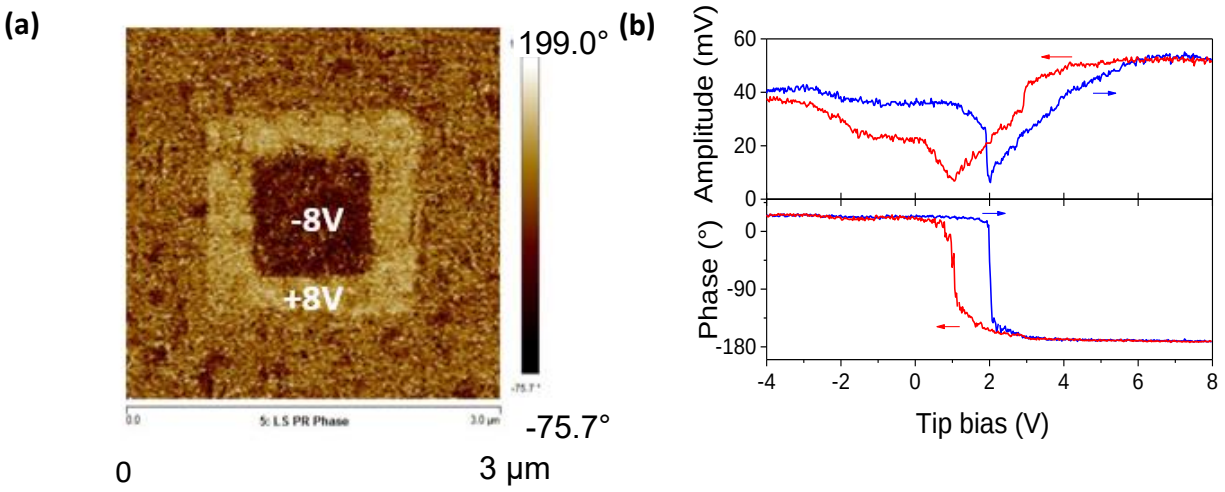

FIG.4.23: (a) PFM phase image after a writing process on the surface and (b) Ferroelectric loop for BFCO

The figure shows the ability to switch the current by applying a voltage higher than the coercitive field, which confirms the previous measurements. The amplitude and phase (which change behaviour from the different steps in PFM) (fig.4.23.b) proves that the writing in PFM mode is not related to a ferroelectric artefact. Subsequently we performed conductive AFM (c-AFM) measurements on the polarized square zone of fig.4.24. We used a 2V charged AFM point to collect the current from the polarized sample.

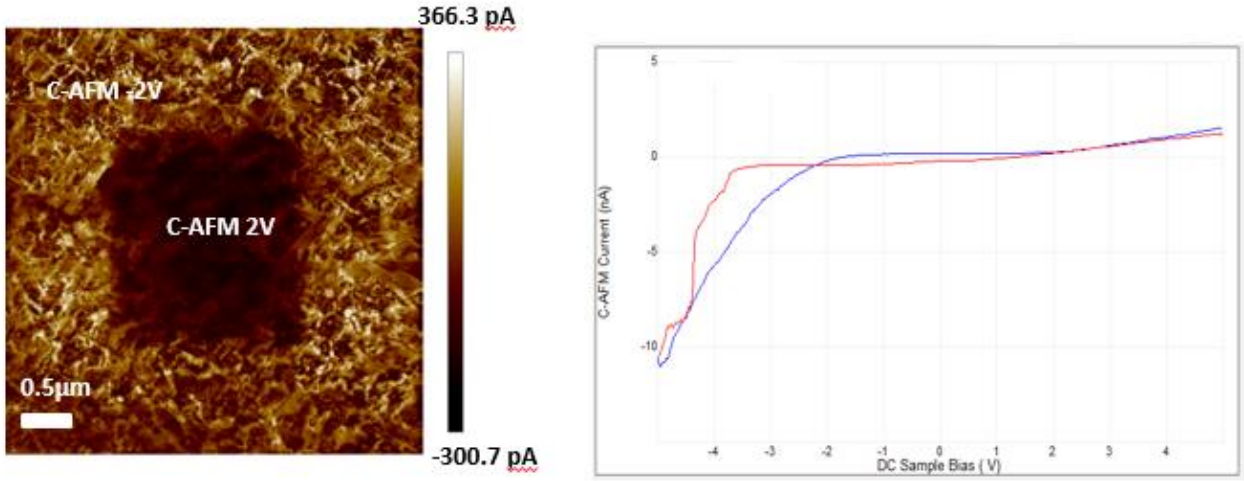

FIG.4.24: c-AFM of BFCO sample firstly polarized by PFM

c-AFM measurements show a very interesting behaviour: the polarized squares present a current of the opposite sign. This result suggests the possibility to reach a switching device which is a clear sign of the ferroelectricity effect (fig.4.24).

4.4.5. Photoelectric effect on BFCO films

Based on the preliminary result shown in figure 4.22, we investigated more deeply the effect of the light illumination on the BFCO films. We first performed impedance measurements for samples deposited at 2Hz having two different thicknesses: 49 nm and 98nm. Fig. 4.25 plots the difference in resistivity under dark and under light for an ITO/BFCO/Nb:STO device. Under dark, the thicker sample is about 30 times more resistive than the thinner one, especially at lower frequencies. This difference becomes less obvious under light. Let's remind that at low frequencies ($f<10^3$ Hz), the resistivity of the sample is linked to the polarization at the interface metal/films while at intermediate frequencies ($10^3<f<10^9$ Hz) the dipolar interaction in the crystal is becoming dominant. Therefore, for those samples the large difference is due to the dipole which forms at the interface between the film and the ITO. As already discussed in chapt.2, the choice of a proper metal is extremely important in order to get a good electron extraction.

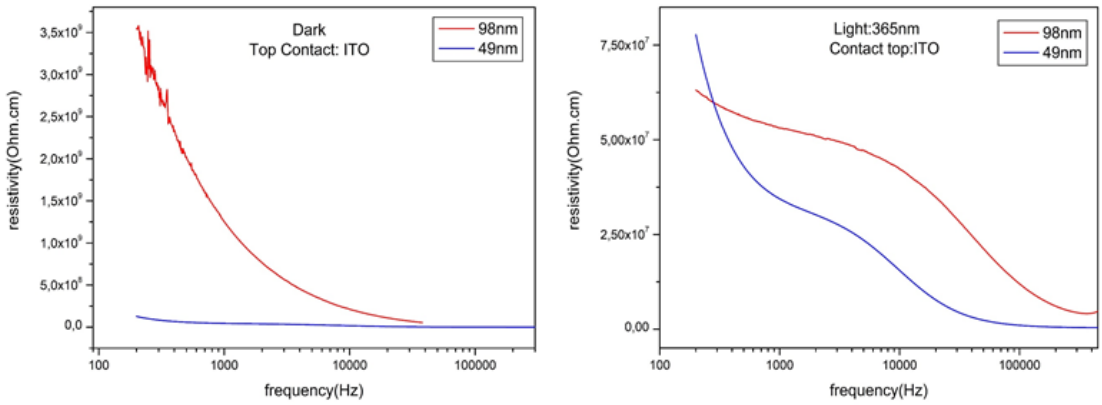

Figure 4.25 a) Impedance scan for BFCO at 98 and 49 nm measured under darkness and b) the same measured under light

In fig.4.26, we compare the measurements made under dark and under light for the two different samples. While for the thicker film, there is a significant reduction in the resistivity, for the thinner one the effect is less important. We could conclude that as the sample get thicker, a higher polarization establishes inside the sample and a higher number of charges

accumulate consequently at the metal/film interface. This effect facilitates the electrons move after the illumination as it lowers the resistivity.

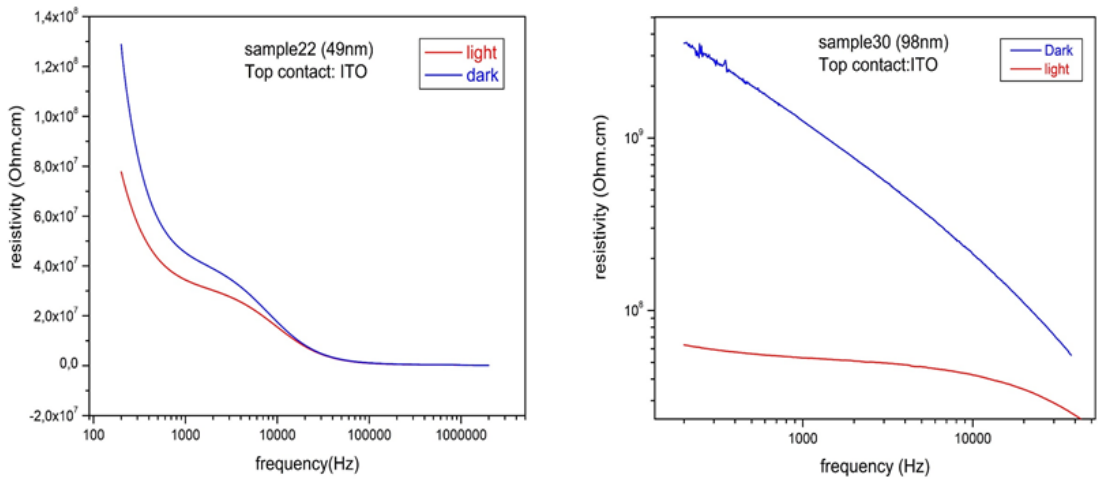

Figure 4.26 a) Impedance scan for BFCO at 98 nm measured under darkness and light and b) the same for BFCO 49 nm

In order to avoid any artefacts linked to hot carriers during illumination, we investigated the effect of temperature on the sample. Thus, we first illuminate the sample with a laser at 365 nm for 4 minutes, then we looked to the sample with a thermic camera in order to record the temperature variation. As it can be seen in fig.4.27, the irradiated zones (yellow-red zones) only shows a $\Delta T<2°C$ in respect to the non-irradiated ones (blue zone). The sample was afterwards heated in a cryostat and it was found that such heating induces a negligible contribution to the pyro-current and voltage changes compared to that observed after light illumination. These results give us confidence that hot carriers are not playing any role during our measurements.

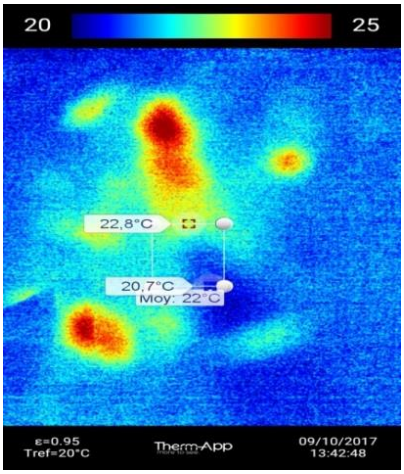

Figure 4.27. Thermic camera image of the BFCO film illuminated by a laser at 365 nm during 4 minutes

The whole ITO/BFCO/NSTO device was also exposed to different light excitation wavelengths and the corresponding photovoltage values were measured. All LEDs where calibrated against power to provide the same light intensity (≈ 8W/m^2). The results are reported in figure 4.28.

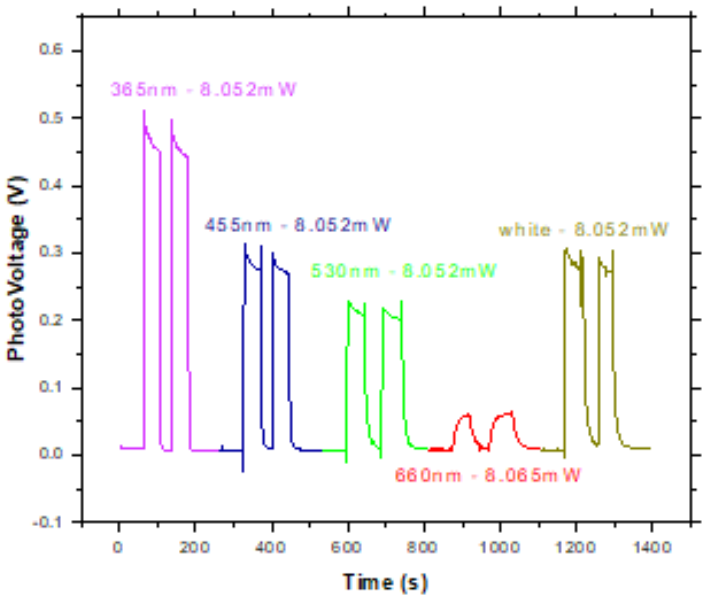

Figure 4.28. Photovoltage measured during illumination of an ITO/BFCO//NSTO device at different wavelengths.

It is obvious that the highest photovoltage is obtained for a laser excitation at 365nm, which corresponds to a high optical absorption range of BFCO. A value of about 500 mV is recorded. Exposure to white light illumination, which is used usually for photovoltaic characterization,

resulted in a 200 mV lower Voc in respect to the one found for the exposure at 365 nm. These results should be taken into account while doing light excitation measurements.

In order to study the effect of the light on BFCO sample, we performed I-V measurements in darkness and under a light emitting diode (LED) of 365 nm with 30 nm of spectral linewidth. Since the photovoltaic effect in ferroelectric materials can depend on the polarization state of the material, we first depolarized it in darkness by an oscillating damped voltage procedure and then measured the I-V characteristic under a 365nm LED with 153 mW/cm^2. The sample remains in the depolarized state as we collect current from zero to +8V. Afterwards, the voltage was swept from +8V to -8V (marked as positive to negative (P→N) sweep) followed by negative to positive (N→P) sweep from -8V to +8V. The resulting curves are reported in figure 4.29. Ferroelectric history dependence becomes important in the photovoltaic response as shown in the evolution of the short circuit current at 0V. The current Isc can be effectively tuned between 0.9 and 2.2 µA depending on the poling sweep. Another important result to notice is that there is an effect even in depolarized state which can suggest a role of the domain walls in the photovoltaic response. The depolarized state can be advantageous compared to the P→N sweep in this case. It is important to understand this hysteretic behaviour in order to reach high PV performance.

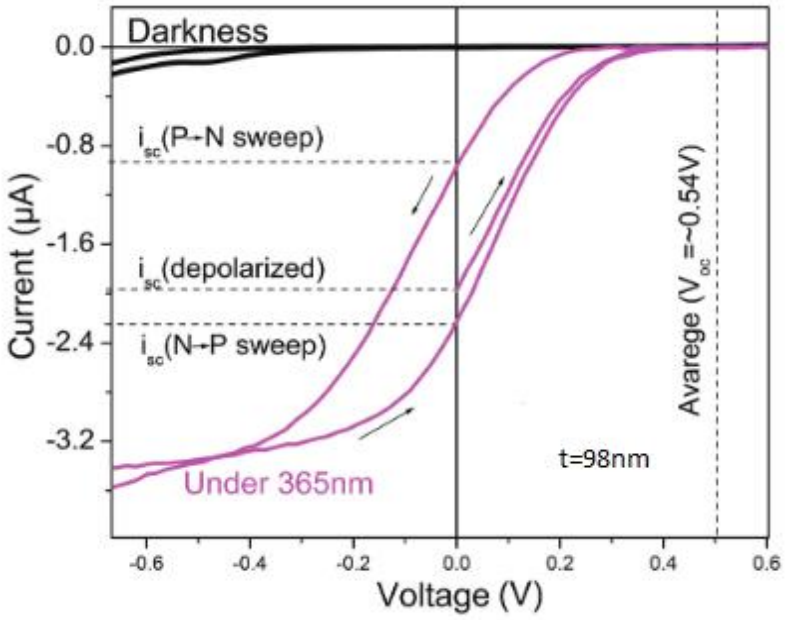

Fig.4.29. Current–voltage measurements on a BFCO sample, in darkness and under 365 nm light irradiation

To get more insight on the ferroelectric memory effect, we measured the open circuit voltage as a function of time by periodical illumination of the sample. Firstly, we polarized the sample positively by sweeping the voltage from -8V→+8V→0V. Subsequently we turned on the 365nm LED for 4 minutes and then off for 8 minutes. We repeated the procedure 3 times (fig.4.30). The curve features show that the photovoltaic response is a combination of optically reversible (transient) and irreversible (remnant) effects. With the sample initially polarized positively, the first pulse of light induces a jump in photovoltage reaching a value of 0.56 V. This is followed by an interesting behavior since when switching off the light, the voltage value did not drop down to 0 V but to a value of 50 mV giving rise to a remnant voltage value. All the subsequent light pulses show the same reversible effect. This behavior can be attributed to both a remnant polarization state and an effect of the light on the ferroelectric-induced polarization.

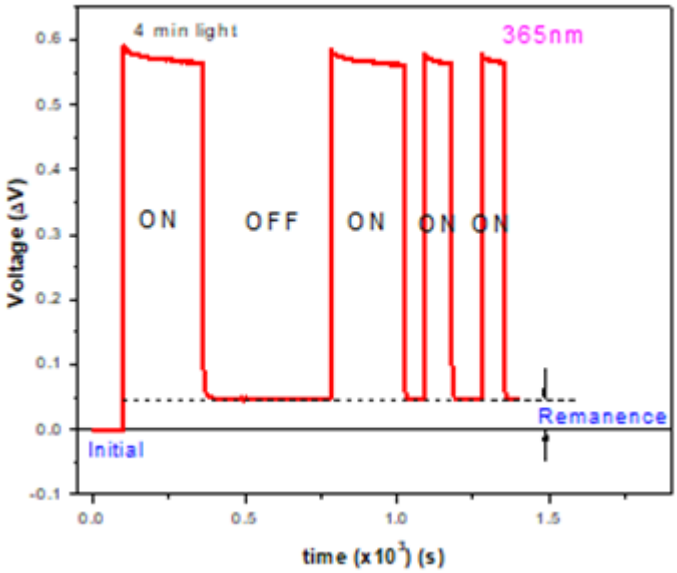

Figure 4.30. Transient and remnant effect of the BFCO sample

In order to elucidate these effects properly, we performed new PFM measurements on the 98 nm thick BFCO sample (fig.4.31). In this case, we wrote the right square in the figure as we did before but applying +8V (large square) and -8V (smaller one); then the sample was illuminated for 4 minutes (same light time as the measurement before). Subsequently we wrote the second square (the left one) in the same way under dark conditions. In agreement with the measurement reported in fig. 4.30, the electrically written FE domains clearly lose their contrast after 4 minutes, while a further light exposure does not modify the PFM image, which

can only be recovered electrically. This behaviour can be explained as follows: after the sample being initially polarized positively, the illumination generates carriers which distributes along the previously forced polarization direction. The generated photo-carriers reduce the surface's charges and consequently change the internal electrical field of the material depolarizing the sample. Upon turning off the light, the carriers trapping makes this decrease partly persisting (remnant effect) leaving the sample in a different polarization state. All the subsequent pulses of illumination reveal only reversible effect. These pulses are in fact of the same power and the corresponding trapping centres are already occupied.

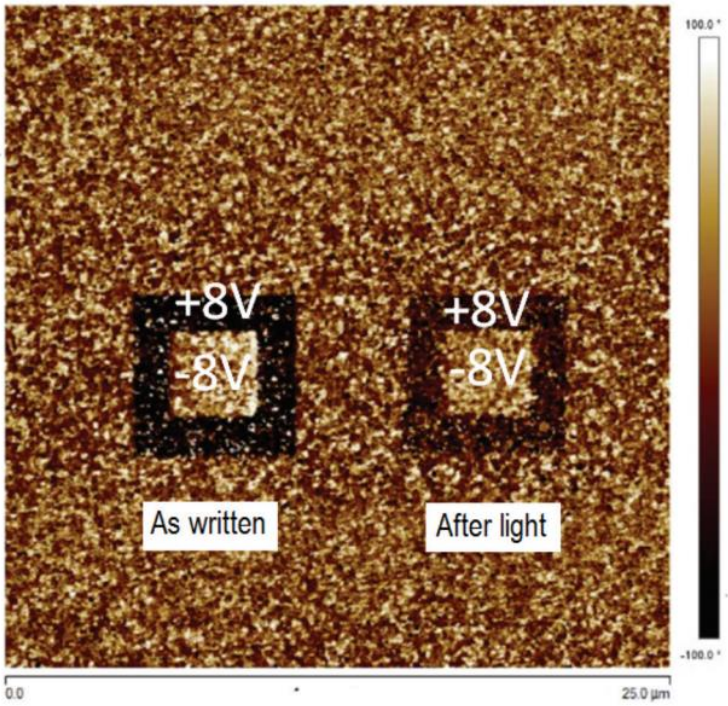

Figure 4.31. PFM poling images before and after exposure to 365 nm light

The hypothesis of carrier's trapping effect can be confirmed by measuring the photovoltage versus light intensity. The data are reported in fig.4.32. The curve exhibits a nonlinear behaviour with three different phenomena: a fast charge generation, an intermediate saturation and a slow relaxation. The latter can be possibly attributed to the charge trapping processes involved in the remnant effect as shown in fig.4.32. It is noteworthy that the possible effect of the light-induced increase of temperature in the sample can be discarded, as we have shown in fig.4.27 above.

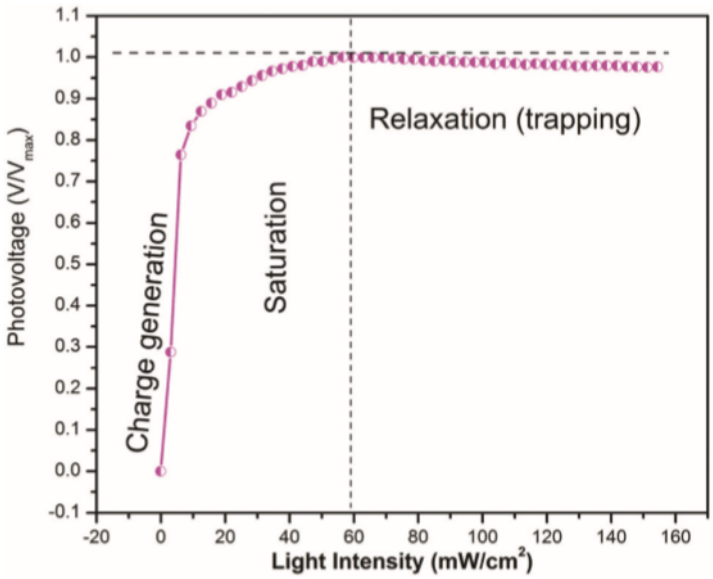

Figure 4.32. Relative change in voltage induced by 365 nm illumination plotted versus light intensity

4.4.6. Photovoltaic effect of PLD-BFCO samples

Current-Voltage characteristics measurements under solar simulator have been carried out for the 98 nm thick BFCO based device in order to study the photovoltaic response. The back contact is a Nb:STO substrate. Different top contacts were tested.

The dark and illuminated I-V characteristics of the device using an ITO as a top contact are plotted in fig.4.33. Before the measurements, the sample was polarized by applying a positive (+8.5V) or negative (-8.5V) voltage. Since the polarization direction is extremely important in these devices, we added an inset showing the applied direction of the voltage. The point is considered the top (where the sample is illuminated).

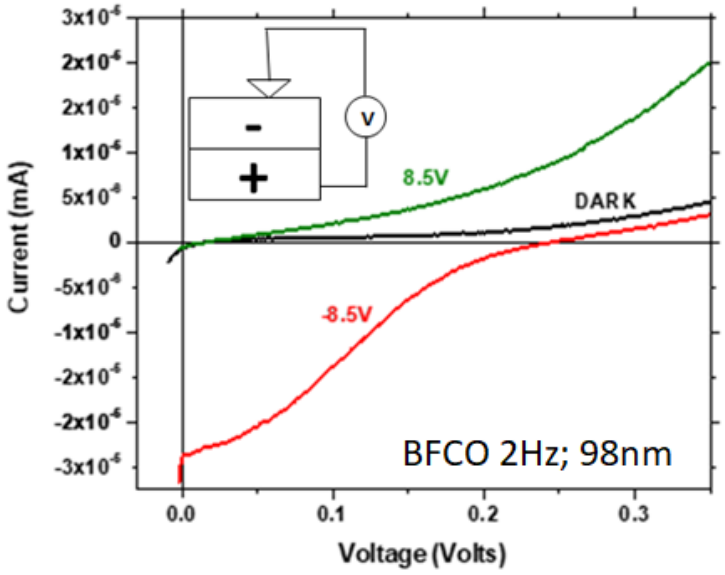

Figure 4.33. I-V under dark and illumination for the device ITO/BFCO/Nb:STO. The sample has been polarized by applying a positive (+8.5V) or negative (-8.5V) voltage prior the measurements.

The curves show that it is possible to change the current behaviour of the device by applying a voltage higher than the coercive field of the ferroelectric material (here 8.5 V) as already described above. However, the I_{sc} and V_{oc} (give in table 4.5 for -8.5 V) are too low to reach a device with a significant PV efficiency. Such low values can be attributed to a low absorbance in the visible region as well as low electron extraction due to close work function between ITO and BFCO, as shown above.

V_{oc} (V)	I_{sc} (nA)	FF
0.25	2.5	0.26

Table 4.5. Photovoltaic parameters of the device ITO/BFCO/NBSTO under Sun illumination

In order to increase the photovoltaic parameters of the BFCO devices, other top contacts were tested, as the formation of a Schottky barrier at the metal/semiconductor interface can be either favourable or detrimental for the device. The choices focused on top contacts with a higher work function compared to the ITO while keeping the optical transparency (as we illuminate from the top). The first contact tested is Platinum. In this case, the height barrier formed at the interface is of about 2eV, to be compared to 1.7 for ITO (fig.4.34).

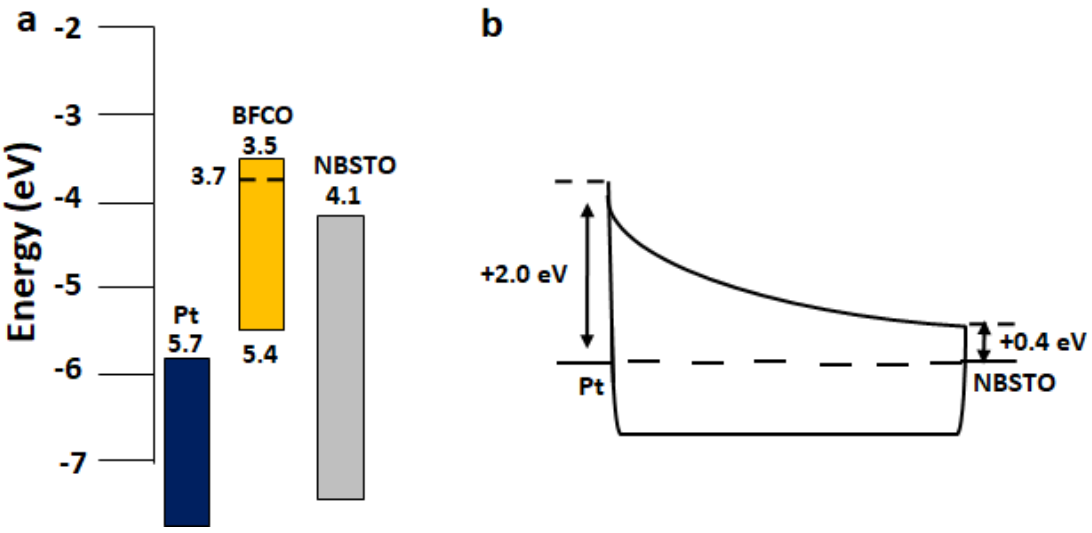

Fig.4.34. Sketch of the energy levels of the device Pt/BFCO/NBSTO

Pt was deposited by sputtering. The metal deposition required a careful control and calibration because only few nanometres of Pt are suited in order to obtain a semi-transparent film. To do so, Pt was sputtered on a glass substrate during 20, 30 and 50 seconds. Figure 4.35 plots the transmittance of the Pt/glass substrates. As expected, lower is the time of deposition, thinner is the Pt film and higher is its transmittance.

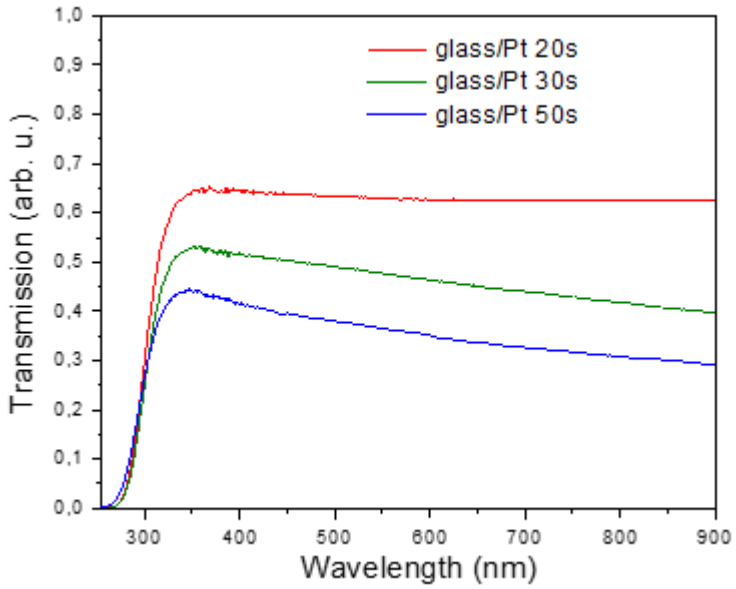

Figure 4.35. Transmittance measurements of Platinum sputtered on glass during 3 different time: 50 s (blue); 30 s (green); 20 s (red).

Only the sample deposited for 20 s has an acceptable transmittance as a top contact. The other two samples absorb more than 50% of the incident light and are not of use in our case. The thickness of the as-deposited films has been deduced from XRR measurements. The sample deposited for 30 s was found to be 3 nm thick while the ones of 50 s is 5 nm thick. The film deposited for 20 s was too thin to be detected by the equipment. It is guessed to be around 2 nm thick.

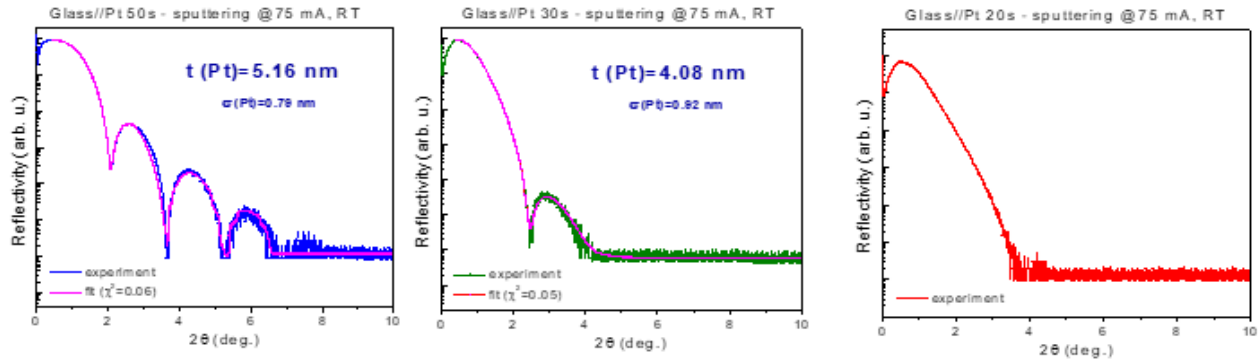

Figure 4.36. XRR measurements of Platinum sputtered on glass during 3 different time:

50 s (blue); 30 s (green); 20 s (red).

Finally, Pt/BFCO/NbSTO devices with 2 nm thick Pt layer and a 98 nm thick BFCO film were produced. Their I-V curves were recorded under dark and solar light illumination. The results are plotted in figure 4.37. Once more, the device did not reach acceptable I_{sc} and V_{oc} values. Although the measured short circuit current is one order of magnitude higher than in the case of ITO/BFCO device, the limited I_{sc} value is probably due to the high light absorption of the Pt top contact. More surprising is the low V_{oc}. In fact, as the Pt work function is higher than BFCO (around 5.7 eV) one should expect the Schottky barrier formed at interface to increase the internal electric field and therefore to generate higher V_{oc}. On the other hand, the high conductivity of Pt can cause the formation of interfacial charges with opposite sign in respect to the internal polarization of the film. The presence of such charges is detrimental for the device itself, as explained in chapter 2. Consequently, both low I_{sc} and V_{oc} are expected. Furthermore, the internal resistance due to interfacial charge formation can be responsible of the low Fill Factor of the device, and also reduces the current and the voltage.

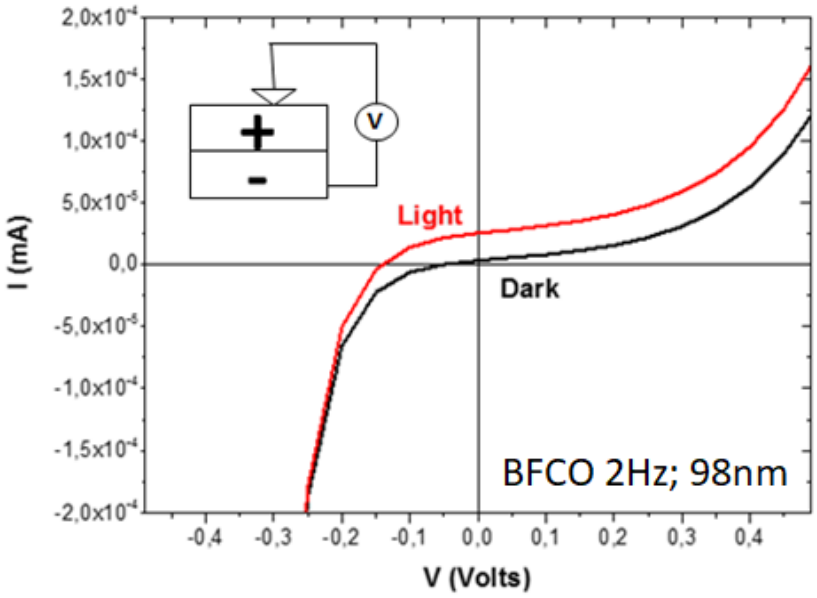

Figure 4.37. I-V curves of the Pt/BFCO/Nb:STO device under dark and light illumination

V_{oc} (V)	I_{sc} (nA)	FF
0.15	27.1	0.35

Table 4.5. Photovoltaic parameters of the device Pt/BFCO/NBSTO under 1 Sun illumination

Another series of devices uses a Gold layer as top contact. This is because its work function of 5.47 eV make it a good candidate to form a barrier with an energy ranging between the one of ITO and Pt (fig.4.38). The deposited gold layer was as thin as 5 nm in order to make it semi-transparent.

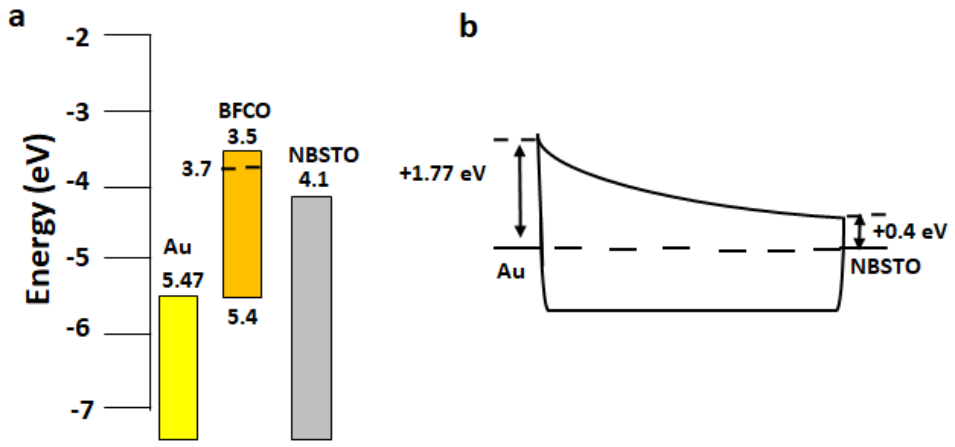

Fig.4.38. Schema of the energy levels of the Au/BFCO/Nb:STO device

The I-V curve of the Au/BFCO/Nb:STO device shows a quite reasonably high V_{oc} , around 330 mV, which is larger than the ones found for ITO/BFCO/Nb:STO and Pt/BFCO/Nb:STO devices. However, the photo-generated current is still too low to reach a good efficiency for the cell. Similar to the Pt case, the high conductivity of Au and therefore the presence of interfacial charges are probably responsible of the low Fill Factor.

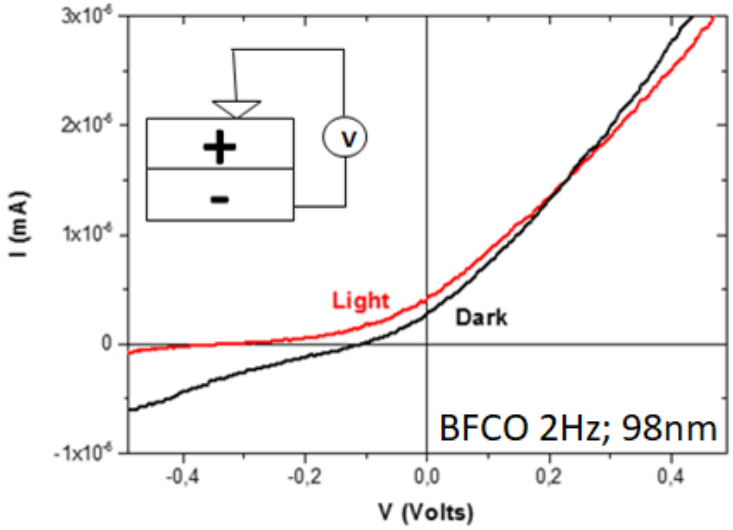

Figure 4.39.I-V curve of the Au/BFCO/Nb:STO device under darkness and illumination

V_{oc} (V)	I_{sc} (nA)	FF
0.33	4.8	0.22

Table 4.6. Photovoltaic parameters of the device Au/BFCO/NBSTO under Sun illumination

A new serie of devices with a WO_3 layer as top contact was prepared. The purpose is to use a material with a higher work function and a lower conductivity than Pt, which should enable to avoid the interfacial charges problem.

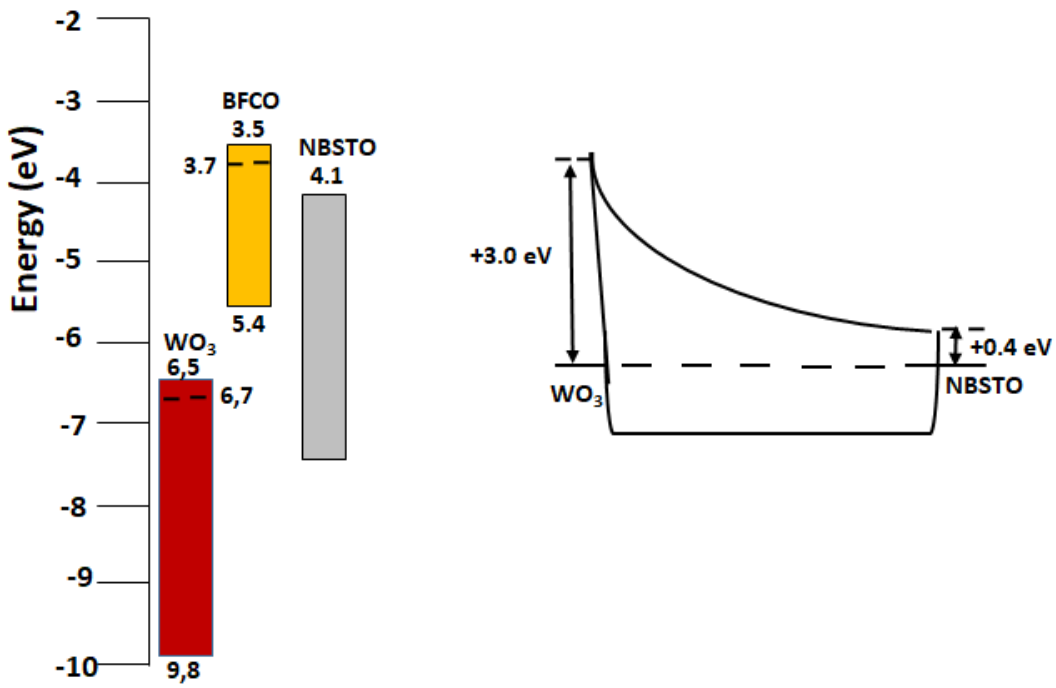

Fig.4.40 Sketch of the energy levels of the device WO_3/BFCO/NBSTO

In this case, we started from WO_3 powder and we sublimated it by using a vacuum thermal evaporation system. The amount of sputtered material was carefully checked by a quartz balance. We first deposited the material on a quartz substrate in order to measure the properties (thickness, transmittance and conductivity). From XRR measurements, we confirmed the deposition of a 36nm thick film with a good grade of roughness of less than 1nm, as shown in fig.4.41.

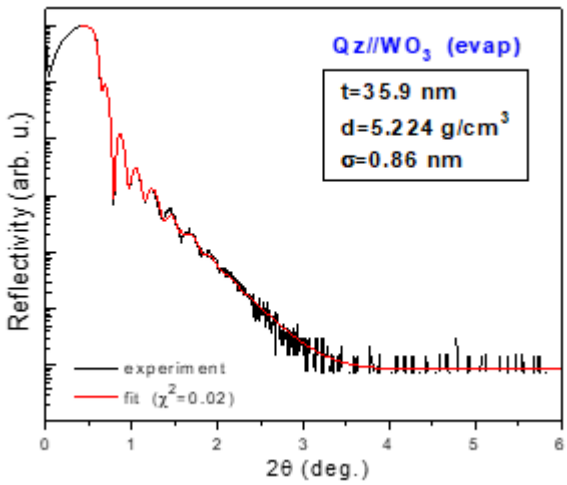

Figure 4.41.XRR of WO_3 film deposited by sublimation on Quartz

Optical analysis of the WO3 layers was performed by using a UV-Vis spectrometer. The film shows a good transmittance in a large range of wavelengths. It starts to absorb around 350 nm. This allows us to exploit a high part of the solar spectra as well as to take benefit from the high workfunction of this material.

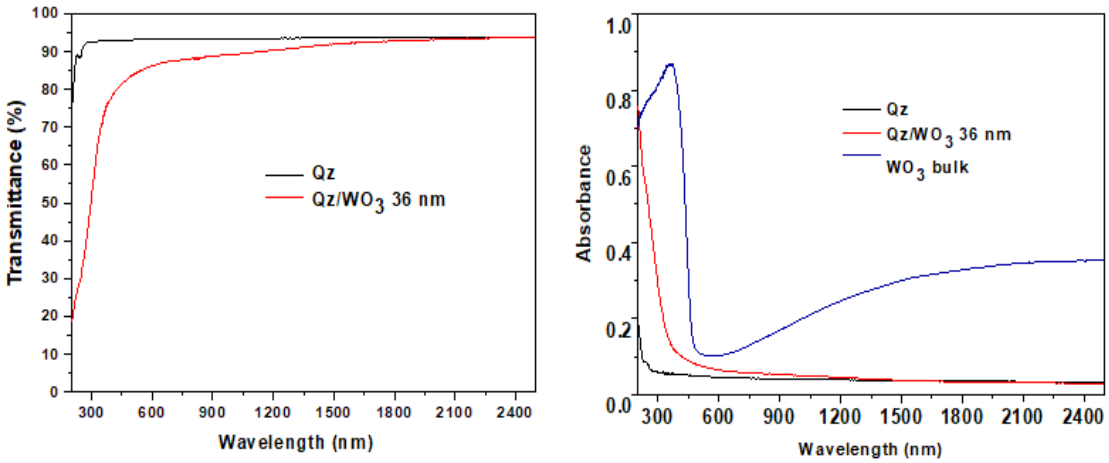

Figure 4.42 a) trasmittance measure of WO_3 film deposited on quartz; b) absorbance spectra of the same film compared with the bulk absorption one

The I-V characteristics of the WO_3/BFCO/Nb:STO device were recorded under dark and 1 sun illumination and the results are shown in fig.4.43. The open circuit voltage V_{oc} increases up to 400 mV which can confirm the assumption that having a top contact with a lower carrier mobility can be advantageous for the Voc. Yet, the resulting I_{sc} is once more very low suggesting that the increase in V_{oc} due to the higher barrier is not sufficient to balance the poor electron extraction (which can be due to the high barrier too). It should be noticed that the dark I-V curve does not pass by zero maybe because of the polarization record of the measurements.

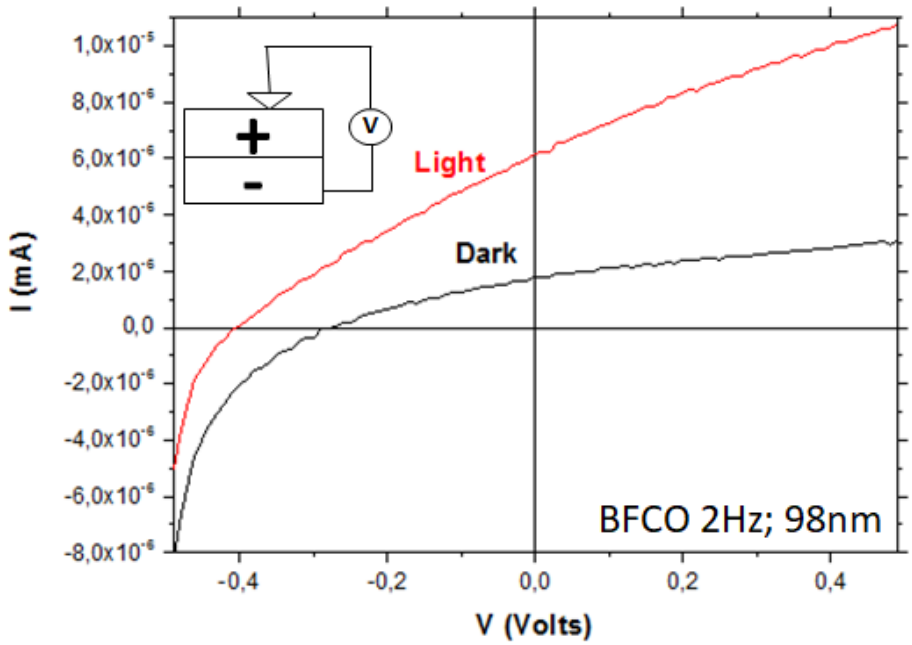

Figure 4.43. I-V curve of the WO_3/BFCO/Nb:STO device under darkness and illumination .

V_{oc} (V)	I_{sc} (nA)	FF
0.41	6.1	0.31

Table 4.7. Photovoltaic parameters of the device WO_3/BFCO/NBSTO under Sun illumination

Finally, we prepared some devices with a top contact with a lower height barrier than the ITO (1.2 eV, fig.4.44). Thus, 100 nm Aluminium-doped Zinc Oxide (AZO) were sputtered on BFCO samples of different thicknesses (7.5, 50 and 98 nm).

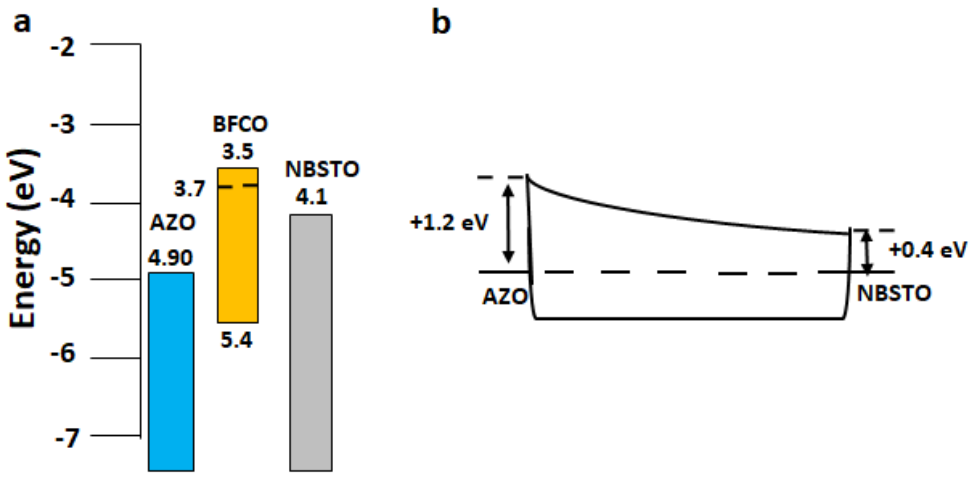

Fig.4.44 Schema of the energy levels of the device AZO/BFCO/NBSTO

First, we measured the transmittance of AZO deposited on quartz (fig.4.45). The curve corresponds to the case of a 110 nm thick sample. As shown, 80% Transmittance in the visible range is still a good compromise for a top contact for photovoltaic applications

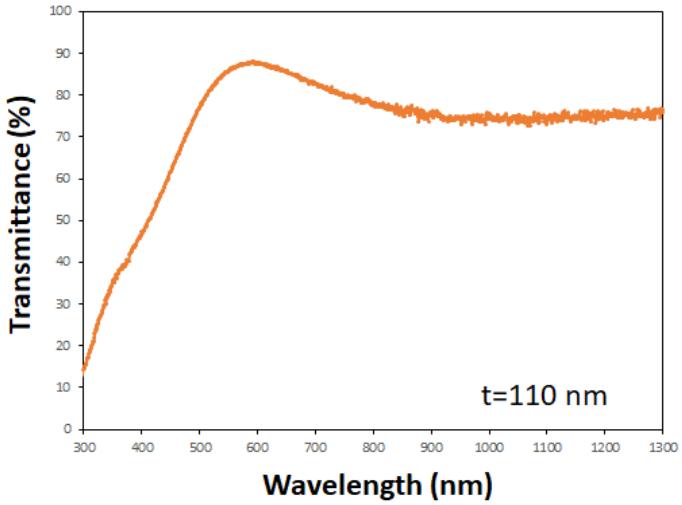

Fig.4.45: Trasmittance measure of AZO film deposited on quartz;

The devices using 50nm and 98 nm thick BFCO did not show any better photovoltaic performances as compared to previous devices. In contrast, the sample with a 7.5 nm BFCO exhibits a higher V_{oc} of 620mV and a good Fill Factor of almost 64%. It is most likely that the lower height barrier was able to generate a huge polarization inside the film and therefore a high Voc. The good FF can be related to the low resistance of the thinner film. On the other hand, the low photo-generated current is probably due to a weak light absorption by the thin BFCO absorber.

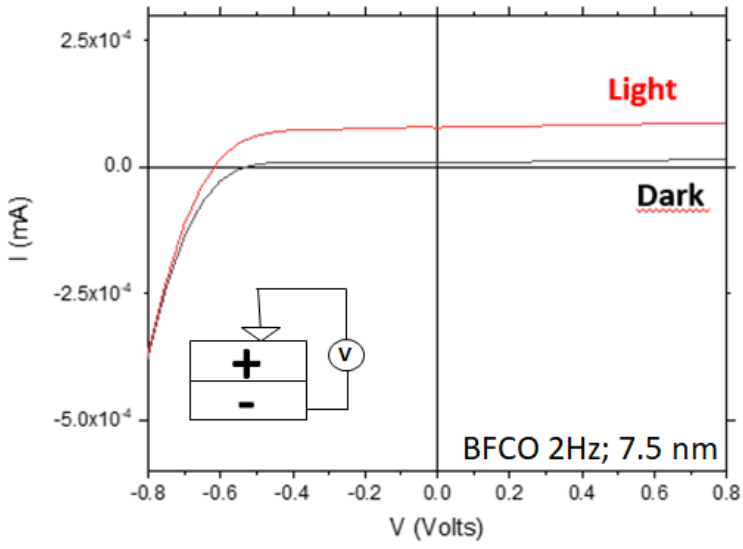

Figure 4.46.I-V curve of the AZO/BFCO/Nb:STO device under darkness and illumination

V_{oc} (V)	I_{sc} (nA)	FF
0.62	78.7	0.64

Table 4.8. Photovoltaic parameters of the device AZO/BFCO/NBSTO under Sun illumination

4.5. Conclusions

In this chapter, we have presented the structural, optical and electrical properties of BFCO films synthesized by the pulsed laser deposition technique. The synthesis resulted in materials oxides with a high degree of crystallinity. Especially, we were able to obtain an epitaxial growth of BFCO on STO and Nb:STO along the axis (100) without any secondary phase in the limit of detection of the machine. We have proven the formation of superstructures along the axis (111) and shown that no other phases were present. Thanks to the operational deposition parameters, especially the laser repetition rate, we were able to tune the bandgap of the BFCO films from 1.94 eV to 2.67 eV, which make such oxide materials suitable for several applications. These experimental results were confirmed by theoretical study, in which we demonstrated that a change in the ordering disposition Fe-Cr have an influence on the bandgap of he material. Moreover we have proven that these changes have an impact even on the magnetic properties of the sample, as shown in SQUID measure and theoretical study. We have demonstrated the ferroelectricity of the deposited films and shown how the polarization memory has a huge impact on the photovoltaic properties. Moreover, we have shown how photovoltaic measurements should be done carefully as the light has an impact on the polarization of the sample, possibly because of light generated carriers which got trapped in the interface metal/semiconductor and influence the internal electric field. We performed electrical studies on the device ITO/BFCO/Nb:STO and proved that it is possible to achieve current switching. We have studied the photovoltaic properties of the PLD-BFCO films. We have varied the top contact type, namely ITO, Pt, Au, WO3, looking for the best charges extraction. We have shown that the best solar cell device is AZO/BFCO/NBSTO for which the AZO/BFCO height barrier is the lowest. An open circuit voltage of more than 600 mV and a high fill factor of 0,64 were measured. However, the photogenerated current is still very low, in the nano-ampere range, which is indicative of either a low optical absorption or carriers' recombination traps or both. Such results are encouraging for photovoltaic applications but much further studies are needed towards a high efficient device.

References of chapter 4:

1. Serrano, A. *et al.* Stabilization of Epitaxial α-Fe $_2$ O $_3$ Thin Films Grown by Pulsed Laser Deposition on Oxide Substrates. *J. Phys. Chem. C* **122,** 16042–16047 (2018).
2. Petukhov, I. A. *et al.* Pulsed laser deposition of conductive indium tin oxide thin films. *Inorg. Mater.* **48,** 1020–1025 (2012).
3. Johnson, A. W. Synthesis of corrins and related macrocycles based on pyrrolic intermediates. *Philos. Trans. R. Soc. Lond. B. Biol. Sci.* **273,** 319–326 (1976).
4. Haindl, S., Hanzawa, K., Sato, H., Hiramatsu, H. & Hosono, H. In-situ growth of superconducting SmO1−x F x FeAs thin films by pulsed laser deposition. *Sci. Rep.* **6,** (2016).
5. Singh, R. K. & Narayan, J. The pulsed-laser deposition of superconducting thin films. *JOM* **43,** 13–20 (1991).
6. Oshima, T., Yokoyama, K., Niwa, M. & Ohtomo, A. Pulsed-laser deposition of superconducting LiTi 2 O 4 ultrathin films. *J. Cryst. Growth* **419,** 153–157 (2015).
7. Hayes, J. P., Stone, L. A., Snelling, H. V., Jenner, A. G. & Greenough, R. D. Magnetic and magnetoelastic properties of thin films by pulsed laser deposition. *IEEE Trans. Magn.* **33,** 3613–3615 (1997).
8. Baig, M. K. *et al.* Pulsed laser deposition of SmCo thin films for MEMS applications. *J. Appl. Res. Technol.* **14,** 287–292 (2016).
9. Zhang, K. *et al.* Development of a high magnetic field assisted pulsed laser deposition system. *Rev. Sci. Instrum.* **86,** 095105 (2015).
10. Goux, L., Gervais, M., Gervais, F., Champeaux, C. & Catherinot, A. Pulsed laser deposition of ferroelectric BST thin films on perovskite substrates: an infrared characterization. *Int. J. Inorg. Mater.* **3,** 839–842 (2001).
11. Purice, A. *et al.* Ferroelectric thin films obtained by pulsed laser deposition. *J. Eur. Ceram. Soc.* **26,** 2937–2943 (2006).
12. Carter, A. C. *et al.* Pulsed laser deposition of ferroelectric thin films for room temperature active microwave electronics. *Integr. Ferroelectr.* **17,** 273–285 (1997).
13. Nechache, R. *et al.* Bandgap tuning of multiferroic oxide solar cells. *Nat. Photonics* **9,** 61–67 (2014).
14. Huang, W. *et al.* Multiferroic Bi $_2$ FeCrO $_6$ based p–i–n heterojunction photovoltaic devices. *J. Mater. Chem. A* **5,** 10355–10364 (2017).
15. Aïssa, B., Nechache, R., Therriault, D., Rosei, F. & Nedil, M. High-frequency electromagnetic properties of epitaxial Bi $_2$ FeCrO $_6$ thin films grown by pulsed laser deposition. *Appl. Phys. Lett.* **99,** 183505 (2011).
16. Nechache, R. *et al.* Epitaxial thin films of the multiferroic double perovskite Bi2FeCrO6 grown on (100)-oriented SrTiO3 substrates: Growth, characterization, and optimization. *J. Appl. Phys.* **105,** 061621 (2009).
17. Yoshikawa, H. & Adachi, S. Optical Constants of ZnO. *Jpn. J. Appl. Phys.* **36,** 6237–6243 (1997).
18. Shabadi, V. *et al.* Origin of superstructures in (double) perovskite thin films. *J. Appl. Phys.* **116,** 114901 (2014).
19. Nechache, R., Harnagea, C. & Pignolet, A. Multiferroic properties—structure relationships in epitaxial Bi $_2$ FeCrO $_6$ thin films: recent developments. *J. Phys. Condens. Matter* **24,** 096001 (2012).

20. Baettig, P., Ederer, C. & Spaldin, N. A. First principles study of the multiferroics Bi Fe O 3 , Bi 2 Fe Cr O 6 , and Bi Cr O 3 : Structure, polarization, and magnetic ordering temperature. *Phys. Rev. B* **72,** (2005).
21. Song, Z.-W. & Liu, B.-G. Electronic structure and magnetic and optical properties of double perovskite Bi_2FeCrO_6 from first-principles investigation. *Chin. Phys. B* **22,** 047506 (2013).
22. Kresse, G. & Furthmüller, J. Efficient iterative schemes for *ab initio* total-energy calculations using a plane-wave basis set. *Phys. Rev. B* **54,** 11169–11186 (1996).
23. Kresse, G. & Joubert, D. From ultrasoft pseudopotentials to the projector augmented-wave method. *Phys. Rev. B* **59,** 1758–1775 (1999).
24. Blöchl, P. E. Projector augmented-wave method. *Phys. Rev. B* **50,** 17953–17979 (1994).
25. Heyd, J., Scuseria, G. E. & Ernzerhof, M. Hybrid functionals based on a screened Coulomb potential. *J. Chem. Phys.* **118,** 8207–8215 (2003).
26. Krukau, A. V., Vydrov, O. A., Izmaylov, A. F. & Scuseria, G. E. Influence of the exchange screening parameter on the performance of screened hybrid functionals. *J. Chem. Phys.* **125,** 224106 (2006).
27. Perdew, J. P., Burke, K. & Ernzerhof, M. Generalized Gradient Approximation Made Simple. *Phys. Rev. Lett.* **77,** 3865–3868 (1996).
28. Dudarev, S. L., Botton, G. A., Savrasov, S. Y., Humphreys, C. J. & Sutton, A. P. Electron-energy-loss spectra and the structural stability of nickel oxide: An LSDA+U study. *Phys. Rev. B* **57,** 1505–1509 (1998).
29. Bader, R. F. W. *Atoms in molecules: a quantum theory*. (Clarendon Press, 2003).
30. Henkelman, G., Arnaldsson, A. & Jónsson, H. A fast and robust algorithm for Bader decomposition of charge density. *Comput. Mater. Sci.* **36,** 354–360 (2006).
31. Tang, W., Sanville, E. & Henkelman, G. A grid-based Bader analysis algorithm without lattice bias. *J. Phys. Condens. Matter* **21,** 084204 (2009).
32. Wang, Y. *et al.* Quantifying charge ordering by density functional theory: Fe3O4 and CaFeO3. *Chem. Phys. Lett.* **607,** 81–84 (2014).
33. Gajdoš, M., Hummer, K., Kresse, G., Furthmüller, J. & Bechstedt, F. Linear optical properties in the projector-augmented wave methodology. *Phys. Rev. B* **73,** (2006).

Conclusions and perspectives

This thesis work is a contribution to the studies of structural, optical and electrical properties of BFCO double perovskite films and their implementation as absorbers in photovoltaic devices. The main objective is to produce a new type of solar cell, based on a ferroelectric absorber, without the need of a p-n junction which would be able in the near future to compete with the conventional devices.

We investigated the properties of BFCO synthesized by sol-gel technique and by PLD techniques. We demonstrate for the first time the formation of a double perovskite by sol-gel technique while published works reported the synthesis of BFCO by this wet method only when doping the BFO perovskite. The kinetic of the reaction by TGA analysis showed that the BFCO phase formation reactions takes place between 580 °C and 750 °C. We investigated the evolution of the phase formation at different temperatures in a conventional furnace, and showed the formation of multicrystalline phase films. On the other hand, we applied the rapid thermal annealing process on sol-gel BFCO synthesis which looks promising. Indeed, By an optimization of the N_2/O_2 ratio as annealing ambient and optimizing the annealing time, we were able to lower the presence of the parasitic phases leading to films containing only bismuth oxide and BFCO phases. In particular, the best results were obtained for the film annealed for 2 minutes in an atmosphere N_2/O_2: 70/30. Future works should focus on the optimization of the RTA annealing process aiming to avoid the formation of the bismuth oxide phase leading to a multiphase BFCO film. This optimization will allow to develop a BFCO based device by wet technique by depositing the BFCO solution on different bottom contact.

The last part of this work was dedicated to the growth and characterization of BFCO films deposited by pulsed laser deposition. We were able to obtain an epitaxial growth of BFCO on STO and Nb:STO along the axis (100) without any secondary phase in the limit of detection of the machine. By varying the deposition parameters, namely the laser repetition rate, we changed the bandgap from 1.96 eV to 2.64 eV. We demonstrated that the change in bandgap can be attributed to the ordering degree inside the double perovskite. Theoretical calculation of the Fe-Cr stacking inside the crystal has confirmed the importance of the ordering of the atoms in the structure of the BFCO films. The electrical properties of the BFCO films were evaluated through measurements of current and capacitance versus the voltage and measures of the internal polarization of the film. Thanks to I-V analysis made before and after

positive and negative polarization, we have shown that the short-circuit current depends on the memory of polarization within the BFCO films. The effect of the illumination on the polarization was confirmed by both electrical and PFM measurements. We have reported for the first time how light exposure increases the capacitance of the film and lowers the internal polarization. We have given an explanation to this phenomenon by assuming an electron charge trapping in the interface metal/semiconductor. Finally, we have fabricated photovoltaic devices using BFCO films and we have experienced different top contacts. We demonstrated that using a top contact with a high carrier mobility , such as Pt and Au, can be detrimental for the quality of the solar cells as the generation of an interfacial dipole can interfere with the internal polarization. We have also tried transparent oxide contacts with different workfunctions and we have proved that AZO creates a lower Schottky junction at the interface metal/semiconductor compared to ITO and WO_3. As a result, the AZO/BFCO solar cell device exhibits a good Voc of 620 mV and a high FF of 64%. However, we have found that the cell performances are limited by the low photovoltaic current most probably because of the lower light absorption within the 10 nm thick film. Future works should focus on the effect of the Schottky barrier on the internal polarization in order to optimize the photovoltaic properties of the device. Moreover it would be interesting to dope the double perovskite to possibly increase the conductivity of the film without affecting the ferroelectric properties of BFCO. Finally, a tandem cell by depositing BFCO with different bandgaps should be made in order to fabricate competitive ferroelectric oxides in the photovoltaic market.

Résumé de thèse en français :

Le marché photovoltaïque, utilisant des modules qui convertissent directement le rayonnement solaire en électricité, est en pleine expansion depuis 20 ans, avec une production mondiale approchant 400GW en 2017. L'essentiel de cette production, presque 95%, est à base de modules en silicium monocristallin ou multi cristallin, le reste est à base de semi-conducteurs en couches minces tels que les composés CdTe (tellure de cadmium), CIGS (Cuivre-Indium- Gallium-Sélénium (et/ou souffre)) ou du silicium amorphe. D'autres matériaux constituant la troisième génération de cellules/modules photovoltaïque sont organiques, donc à base de polymères ou de petites molécules. Plus récemment, les cellules solaires pérovskite hybrides ont fait leur entrée dans le domaine du photovoltaïque, en particulier parce que leur rendement de conversion supérieur à 20% associé à leur faible coût de fabrication les rend prometteurs. Les inconvénients majeurs à ce jour de cette nouvelle catégorie de cellules sont leur instabilité sous rayonnement (très forte dégradation) et la présence du plomb dans le composé principal qui est dangereux pour l'environnement. De nouvelles voies (nouveaux matériaux et/ou concepts novateurs) sont donc à trouver pour développer des cellules avec un rendement de conversion convenable et un coût raisonnable.

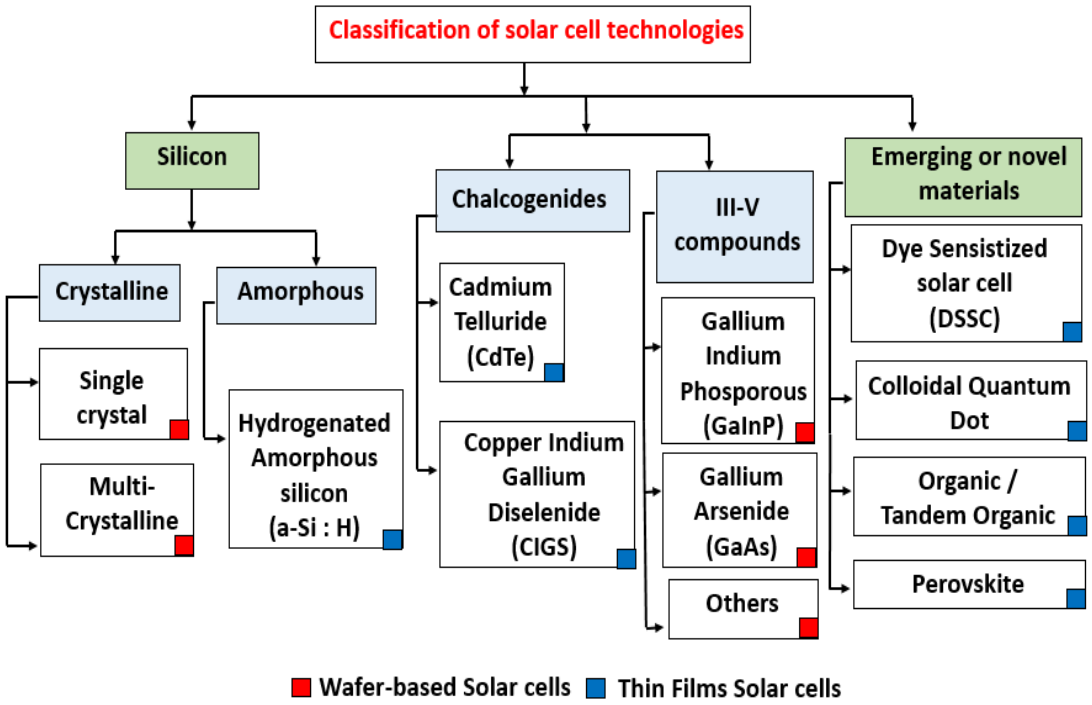

Fig.1 : Schéma de nouvelles technologies photovoltaïques

Une catégorie intéressante parmi les nouveaux matériaux pour la conversion photovoltaïque sont les oxydes inorganiques dont la structure cristallographique, la composition, la bande interdite et l'absorption optique peuvent être facilement modifiées lors de l'élaboration. Ces oxydes fonctionnels présentent une grande stabilité thermique et chimique. Parmi ces oxydes les plus étudiés, on peut citer le matériau Cu_2O, qui, combiné avec une couche organique a permis d'atteindre un rendement de conversion proche de 8%.

L'autre famille de matériaux très prometteuse pour le photovoltaïque tout-oxyde est celle utilisant comme absorbeurs des films de pérovskites ferroélectriques inorganiques (FERRO-PEV). Ces derniers se différentient des autres matériaux absorbeurs (CIGS, CdTe, Si …) par la structure cristallographique mais également par le fonctionnement du dispositif photovoltaïque lui-même, qui classiquement utilise des jonctions P-N pour la dissociation des charges. En effet, dans ce système utilisant des FERRO-PEV, un champ électrique externe initial est nécessaire pour polariser le matériau oxyde. De cette manière, l'oxyde ferroélectrique génère après excitation lumineuse non seulement les paires électrons-trous (e-h), mais les sépare même puisqu'ils vont suivre le champ électrique généré. Dans l'une des premières expériences sur un oxyde ferroélectrique, il a été constaté qu'une tension élevée de circuit-ouvert (Voc) peut être produite, bien supérieure en valeur à la largeur de la bande interdite du matériau lui-même, avec cependant un courant de court-circuit (Isc) généré faible. Ces matériaux FERRO-PEV sont restés une curiosité scientifique pendant longtemps car ils n'étaient pas capables de produire un rendement de conversion supérieur à 1%, principalement parce que la bande interdite de la plupart de ces oxydes est supérieure à 3 eV, avec donc une faible absorption du rayonnement solaire. Une avancée majeure a été obtenue par la découverte de la double pérovskite Bi_2FeCrO_6 (génériquement BFCO). Grâce à son double site B' et B' ', il a été possible d'obtenir une largeur de la bande interdite du matériau de 1,4 eV, plus adaptée par rapport au spectre solaire. De cette manière, il était démontré 3,3% de rendement de conversion avec une cellule solaire à simple jonction et 8,1% sur une cellule solaire tandem réalisée avec 3 couches BFCO avec différentes bandes interdites. Très peu de travaux ont concerné ce matériau dans la littérature. Ainsi, la maîtrise de la croissance de ces matériaux d'une part et la compréhension des phénomènes de transport des charges d'autre part constituent l'essence de ce travail de thèse. Ce manuscrit va adresser les points suivant : la synthèse de films BFCO par des voies chimiques (sol-gel) ou physique (dépôt assisté par laser pulsé ou PLD), les caractérisations très fines des matériaux obtenus pour

appréhender leurs propriétés optiques et électriques en fonction de la composition des couches et de leurs structures cristallographiques, et enfin la réalisation de composants photovoltaïques test sur ces matériaux et commenter leurs propriétés de conversion.

Dans une première partie, nous nous sommes concentrés sur la synthèse des films BFCO par la méthode chimique sol-gel (BFCO-SG). En particulier, la synthèse de composés tels que $BiFeO_3$ et $BiCrO_3$ par sol-gel a déjà été démontrée mais à ce jour, il n'y a pas beaucoup d'informations concernant la synthèse sol-gel des films de BFCO. Le principal problème réside dans le fait que de nombreuses pérovskites à base de Bi avec la formule Bi [B] O_3 nécessitent généralement une pression élevée pour obtenir leur forme pérovskite. La stabilité chimique du BFO est assez controversée: certains groupes montrent une stabilité jusqu'à 930 ° C et après sa décomposition en Bi_2O_3 et $Bi_2Fe_4O_9$. D'autres ont indiqué qu'il n'était stable qu'à des températures plus basses mais qu'aucune conversion à 100% n'était obtenue. Il est donc primordial d'analyser la réaction avant de commencer la synthèse. Une première poudre a été préparée par frittage afin d'étudier la cinétique de la réaction par RTA-TGA :

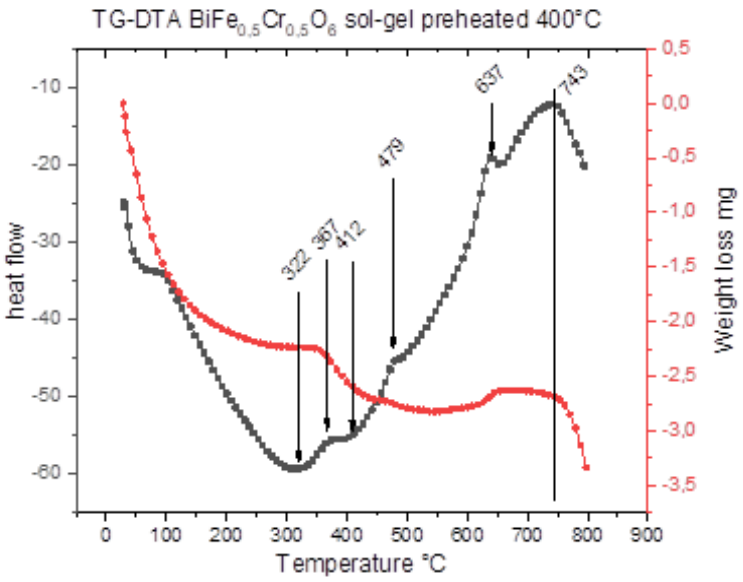

Fig.2: TGA rapide à base de poudre BFCO

L'analyse TGA montre que la réaction de BFCO commence autour de 637 ° C et se maintient jusqu'à 743 ° C où les réactions de dégradation ont lieu. Cela étant, nous avons effectué une analyse DRX sur la poudre en augmentant la température à 500 ° C (avant le début de la réaction), à 650 ° C (lorsque la réaction vient de commencer) et à 750 ° C (à la fin de la

réaction). Après ça, nous avons préparé la solution de sol gel et déposée sur Si (100) ; un recuit thermique commun dans un four pendant 1 h sous air a été fait. Les analyses DRX sont montrées dans la fig.3 :

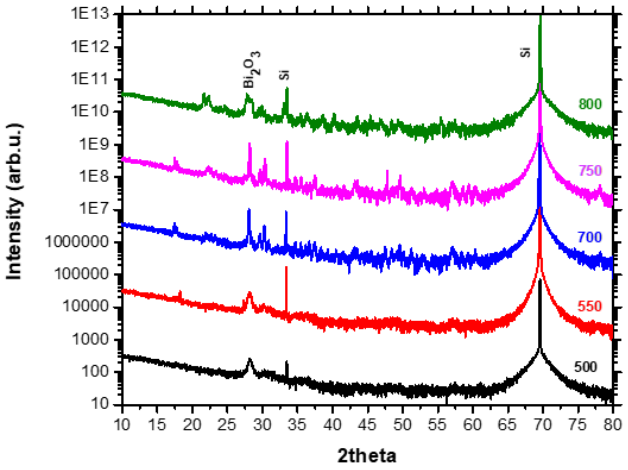

Fig.3: Spectres de diffraction des rayons X des films de BFCO déposés par sol-gel et chauffés à différentes températures

Comme on peut le voir sur la figure 3.6, seule la phase Bi2O3 est formée à 500 ° C mais la phase BFCO est absente à 700 ° C, un pic de faible intensité commence à apparaître et il devient plus intense jusqu'à former un doublet à 800 ° C. Enfin, un pic de faible intensité est observé à 78 ° pour les échantillons recuits à 700 et 750 ° C, ce qui peut indiquer la formation d'une phase BFCO. Ceci est cohérent avec l'analyse de TGA rapportée ci-dessus qui indique que la phase BFCO peut être formée dans la plage de température de 700 ° C à 750 ° C. Comme nous n'étions pas arrivé à former une seule phase BFCO avec recuit commun, nous avons essayé le recuit par recuit thermique rapide (RTA) comment suggéré dans la littérature. Les échantillons avec 3 différentes stœchiométries, sont recuits sous 2 différentes atmosphères, comme montré dans le tableau :

Samples	Formula	Temperature (°C)	N2/O2	Time [RTA] (s)	Layers*	Substrate
BFCO RTA 08	Bi_2FeCrO_6	750	80/20	120	2	Si
BFCO RTA 09	$Bi_2Fe_{1.1}Cr_{0.9}O_6$	750	80/20	120	2	Si
BFCO RTA 10	$Bi_2Fe_{0.9}Cr_{1.1}O_6$	750	80/20	120	2	Si
BFCO RTA 11	Bi_2FeCrO_6	750	70/30	120	2	Si
BFCO RTA 12	$Bi_2Fe_{1.1}Cr_{0.9}O_6$	750	70/30	120	2	Si
BFCO RTA 13	$Bi_2Fe_{0.9}Cr_{1.1}O_6$	750	70/30	120	2	Si

Table.1.Échantillons BFCO déposés par sol gel chauffé par RTA

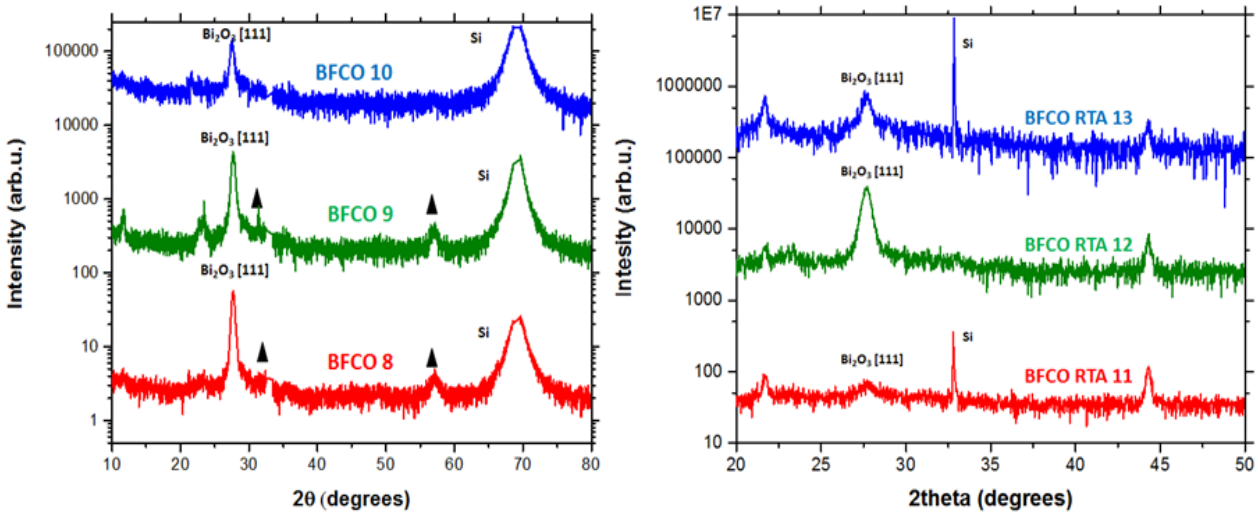

Fig.4: DRX spectre du BFCO en différent stœchiométrie recuit par RTA en diffèrent atmosphères

Dans la figure, les triangles soulignent la phase de BFCO. La phase de Bi2O3 est trouvée pour tous les échantillons. Pour l'échantillon BFCO 8 qui a Fe = Cr = 1, le DRX ne présente que la phase de BFCO et d'oxyde de bismuth. Pour l'échantillon BFCO 9 avec Fe / Cr = 1,2, la phase de l'oxyde de bismuth est bien identifiée comme celle de BFCO; d'autres phases non identifiées sont également présentes. Comme pour l'échantillon BFCO 10 qui présente un excès de chrome (Fe / Cr = 0,82), seule la phase de l'oxyde de bismuth est visible. Les données DRX montrent que les échantillons recuits dans une atmosphère oxydante plus forte (11, 12,13) présentent une inhibition dans la formation d'une phase BFCO dans les échantillons et résultent plutôt de la formation de la phase d'oxyde de bismuth et des 1 à 2 autres phases probablement des composés oxydes de fer ou de chrome. Dans cette étude préliminaire sur la synthèse de BFCO, on a démontré qu'il est difficile d'obtenir une seule phase du BFCO par méthode sol-gel. Par contre, si avec recuit commun on a l'apparition de différentes phases parasites, avec recuit thermique rapide on peut obtenir un film avec seulement la phase de BFCO et d'oxyde de Bismuth. Des études complémentaires devront se focaliser sur l'élimination de l'oxyde de Bismuth afin d'obtenir une seule phase BFCO.

Dans une deuxième étude, nous nous sommes concentrés sur la synthèse des films BFCO obtenus par la méthode physique d'ablation laser pulsée (pulsed laser deposition ou PLD) utilisant une cible de BFCO pressée. Les films BFCO-PLD ont été déposés sur des substrats isolants de SrTiO3 (STO) (100), (111) et (110) et substrats conducteurs tels que Nb: STO (100) dopé à 0,5% en Nb afin d'avoir un contact arrière conducteur. Lors de cette étude, nous avons

varié plusieurs paramètres de fonctionnement tels que la fluence du laser, la fréquence des tirs laser, la pression partielle d'oxygène dans le réacteur, et la température de dépôt. Nous nous sommes concentrés sur des conditions de dépôt spécifiques (T = 750 ° C, pO2 = 10-2 mbar, E = 26 mJ) et nous avons montré qu'il était possible d'obtenir des films épitaxiés à des taux de répétition du laser différents:

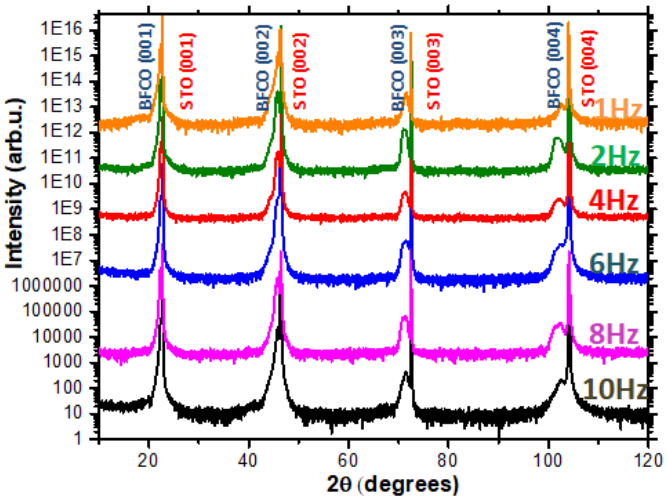

Figure 5 : Θ-2θ scan du BFCO déposé par PLD

Un Φ scan et un Θ-2θ le long de l'axe (111) ont été réalisés pour montrer la présence de superstructure du BFCO. Les valeurs de la bande interdite des films BFCO dépsoés par PLD ont été extraites des mesures d'ellipsométrie. Les résultats sont présentés sur la fig.4.9. Les facteurs de mérite liées aux valeurs du chi carré étaient toujours meilleures que 0,2. On constate que la bande interdite augmente de 1,9 à 2,6 eV lorsque la vitesse de dépôt augmente de 1 à 10 Hz:

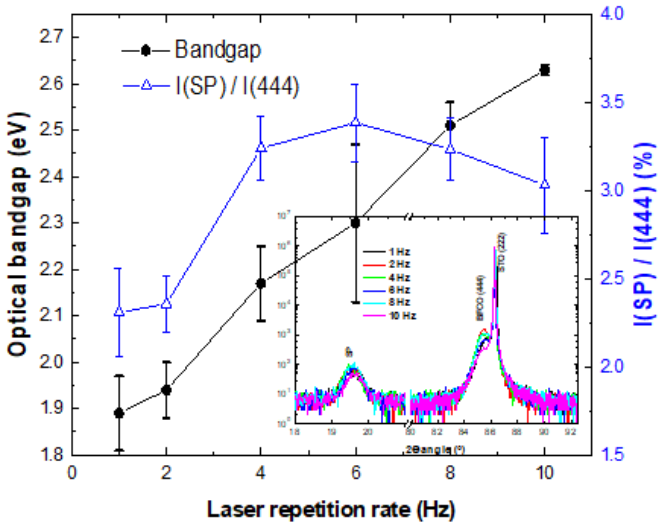

Fig.6. Variation de la bande interdite avec le taux de répétition du laser. Les valeurs sont définies comme le rapport entre l'intensité du pic de la superstructure (SP) et le pic (444) de BFCO (zoomé dans l'encart)

Normalement, cet effet est lié à une différence dans la superstructure, visible sur le pic de la superstructure par XRD (encart sur la fig.6). De manière surprenante, le rapport I_{sp} / I_{444} avec augmentation du taux de répétition a peu évolué, probablement en raison de la faible diffusion entre Fe et Cr. En complément, nous étudions les propriétés magnétiques des films développés. En fait, il est connu que le désordre cationique à l'intérieur de la double pérovskite devrait réduire fortement l'aimantation en raison des interactions antiferromagnétiques (Fe-O-Fe et Cr-O-Cr) apparaissant dans le système. :

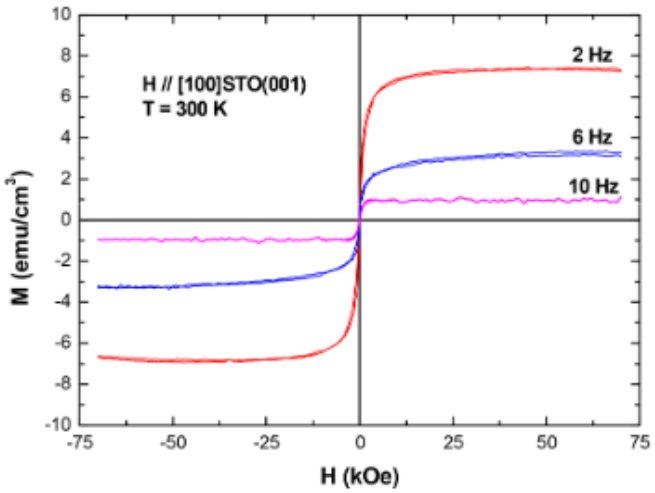

Fig7 : Cycle d'aimantation à la température ambiante mesuré pour le BFCO déposé à 2, 6 et 10 Hz.

Les valeurs croissantes de l'aimantation suggèrent un ordre accru à l'intérieur du cristal. Nous avons donc étudié l'effet du couplage Fe / Cr par des études théoriques; Nous avons d'abord construit une cellule unitaire hexagonale de BFCO (contenant les sites 3 Fe et 3 Cr); ensuite, en utilisant la fonctionnelle HSE06, nous avons extrait la bande interdite pour les différentes configurations. En construisant les cellules hexagonales, nous avons maintenu la position atomique indépendamment du site de Fe et de Cr occupé par un atome de Fe ou de Cr. Nous avons construit la structure «parfaitement ordonnée» en utilisant une cellule hexagonale où Fe occupe le site Fe et Cr occupe le site Cr. De cette façon, la cellule présente une configuration alternative des plans Fe et Cr (0001). Nous avons ensuite utilisé la notation FCFCFC où F et C correspondent respectivement aux plans Fe et Cr (0001) dans l'empilement. Nous avons construit trois autres configurations légèrement désordonnées qui sont CFFCFC; FFCCFC; FFFCCC. La configuration ordonnée ainsi que les trois désordonnées sont présentées dans la fig.8 :

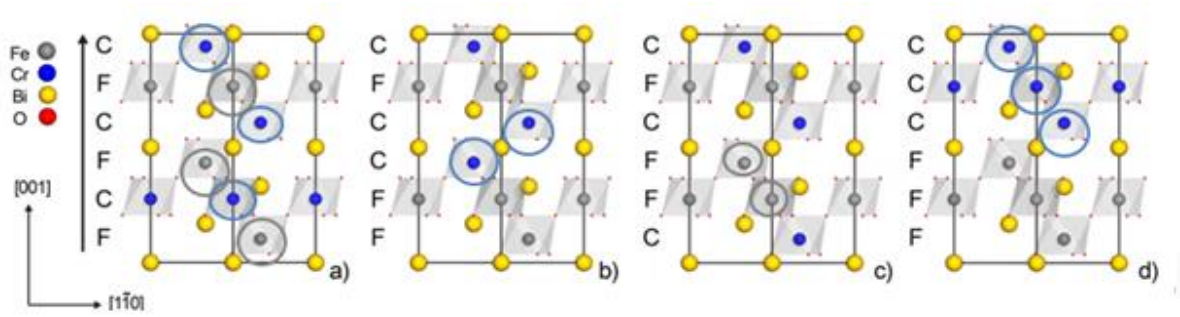

Configuration	Eg (up)/Eg (down) (eV)
a) FCFCFC	4.15/2.30
b) FFCCFC	3.12/2.52
c) CFFCFC	3.13/2.55
d) FFFCCC	3.08/2.50

Figure 8 : a) Structure cristalline idéale «entièrement ordonnée» et b-d) «désordonnée» utilisée pour le calcul ab initio et les bandes interdites relatives

Il est possible de remarquer qu'un ordre croissant dans la structure cristalline provoque une décroissance de la largeur de la bande interdite, en bon accord avec les résultats expérimentaux. Par la suite, nous avons déposé BFCO à 2Hz sur Nb: STO pour effectuer les mesures électriques, une épaisseur de 100 nm d'une couche transparente d'ITO a été pulvérisée comme contact supérieur. La figure 4.23 représente une courbe I-V entre -8V et 8V enregistrée dans l'obscurité. À + 6V, un pic clair provenant de l'inversion de polarisation FE apparaît malgré la forte contribution des courants de fuite. Cet effet est représenté de manière plus visible dans l'encadré de la figure 9 :

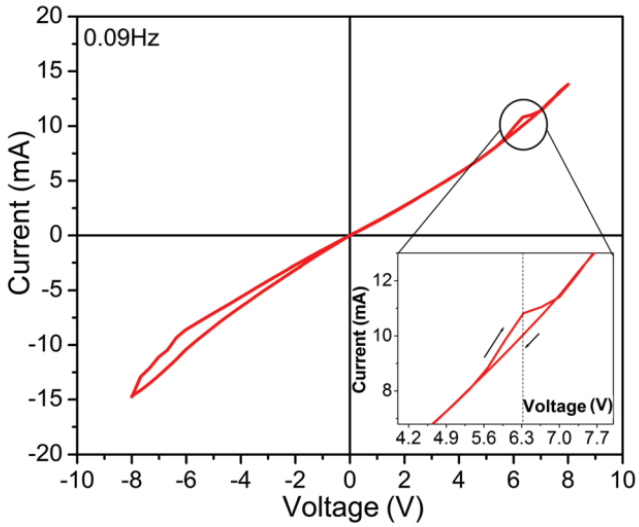

Figure 9: Boucle I-V d'un film Bi2FeCrO6 sous l'obscurité.

Afin d'étudier l'effet de la lumière sur l'échantillon BFCO, nous avons effectué des mesures I-V sous obscurité et illuminé par une diode électroluminescente (DEL) de 365 nm avec une largeur de raie spectrale de 30 nm. L'effet photovoltaïque dans les matériaux ferroélectriques pouvant dépendre de l'état de polarisation du matériau, nous l'avons d'abord dépolarisé dans l'obscurité puis avons mesuré la caractéristique I-V sous une illumination LED 365 nm à 153 mW / cm2. L'échantillon reste dans l'état dépolarisé pendant que nous collectons le courant de zéro à + 8V. Ensuite, la tension a été balayée de + 8V à -8V (marquée comme positive à négative (P → N)) suivie de balayage négatif à positif (N → P) de -8V à +8V (Fig.4.31.). Les courbes résultantes sont reportées dans la figure 10. La dépendance à l'histoire ferroélectrique devient importante dans la réponse photovoltaïque, comme le montre l'évolution du courant de court-circuit à 0V. l'Isc peut être modulé efficacement entre 0,9 et 2,2 µA en fonction du balayage de polarisation.

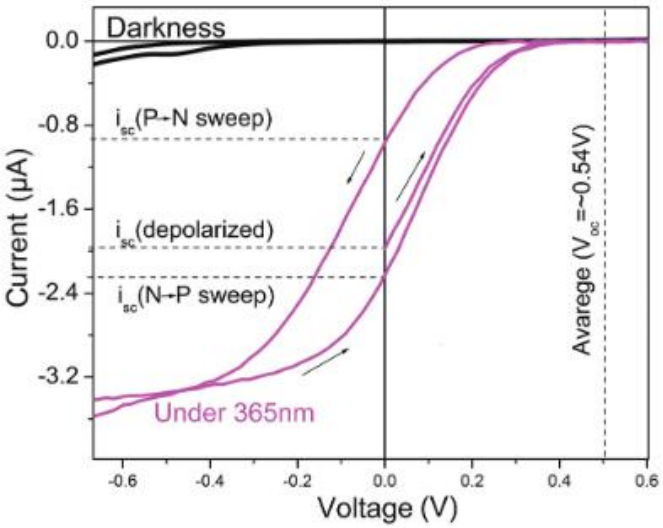

Fig.10 : Mesures de courant-tension sur un échantillon BFCO, dans l'obscurité et sous irradiation lumineuse à 365 nm

Pour mieux comprendre l'effet de la mémoire ferroélectrique, nous avons mesuré la tension en circuit ouvert en fonction du temps en allumant périodiquement l'échantillon. Tout d'abord, nous avons polarisé l'échantillon de manière positive en balayant la tension de -8V → + 8V → 0V. Par la suite, nous avons allumé la LED 365nm pendant 4 minutes puis éteint pendant 8 minutes. Nous avons répété la procédure 3 fois (fig.11). Les caractéristiques de la courbe montrent que la réponse photovoltaïque est une combinaison d'effets optiquement réversibles (transitoires) et irréversibles (rémanents). Avec l'échantillon initialement polarisé positivement, la première impulsion de lumière induit un saut de photo tension atteignant une valeur de 0,56 V. Ceci est suivi d'un comportement intéressant car lors de la coupure de la lumière, la valeur de la tension ne descend pas à 0 V mais une valeur de 50 mV donnant lieu à une valeur de tension résiduelle. Toutes les impulsions de lumière suivantes montrent le même effet réversible. Ce comportement peut être attribué à la fois à un état de polarisation résiduel et à un effet de la lumière sur la polarisation induite par le ferroélectrique.

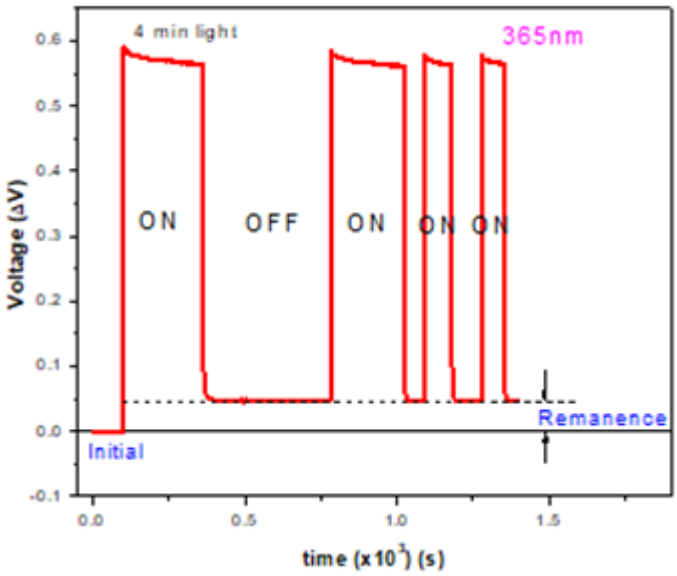

Figure 11 : Effet transitoire et résiduel de l'échantillon de BFCO

Afin d'élucider correctement ces effets, nous avons effectué de nouvelles mesures de piezoresponse force microscopy (PFM) sur l'échantillon BFCO de 98 nm d'épaisseur (fig.12). Nous avons écrit le carré droit en appliquant + 8V (grand carré) et -8V (plus petit); ensuite, l'échantillon a été éclairé pendant 4 minutes (même temps lumineux que la mesure précédente). Par la suite, nous avons écrit le deuxième carré (celui de gauche) de la même manière sous obscurité. Les domaines FE écrits électriquement perdent clairement leur contraste après 4 minutes, tandis qu'une exposition à la lumière supplémentaire ne modifie pas l'image PFM, qui ne peut être récupérée que électriquement. Ce comportement peut être expliqué comme suit: après que l'échantillon a été polarisé initialement de manière positive, l'illumination génère des porteurs qui se distribuent le long de la direction de polarisation précédemment induite. Les photo-porteurs générés réduisent les charges de la surface et modifient par conséquent le champ électrique interne du matériau en dépolarisant l'échantillon. En éteignant la lumière, le piégeage des porteurs rend cette diminution partiellement persistante (effet résiduel), laissant l'échantillon dans un état de polarisation différent. Toutes les impulsions d'illumination subséquentes ne révèlent qu'un effet réversible; ces impulsions sont en fait de même puissance et les centres de piégeage correspondants sont déjà occupés.

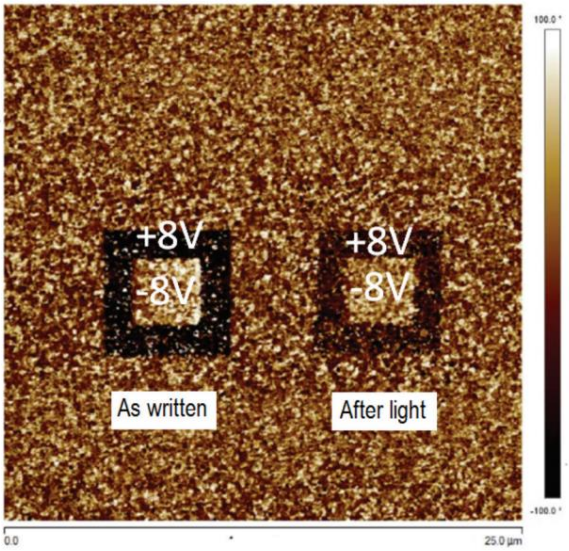

Figure 12 : Images de polarisation PFM avant et après exposition à la lumière à 365 nm

L'hypothèse de l'effet de piégeage des porteurs peut être confirmée en mesurant la tension photoélectrique en fonction de l'intensité lumineuse. Les données sont reportées sur la fig.13. La courbe présente un comportement non linéaire avec trois phénomènes différents: une génération de charge rapide, une saturation intermédiaire et une relaxation lente. Ce dernier facteur peut être attribué aux processus de piégeage de charge impliqués dans l'effet résiduel.

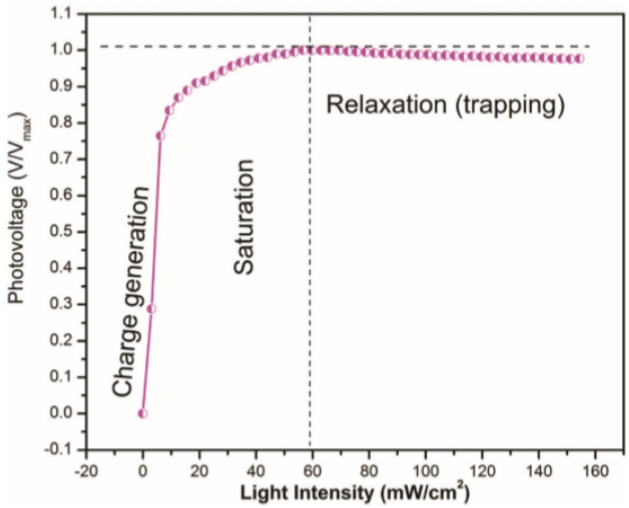

Figure 13 : Variation relative de la tension induite par un éclairage à 365 nm en fonction de l'intensité lumineuse

Afin d'étudier les propriétés photovoltaïques des échantillons BFCO, nous avons effectué des mesures I-V sous lumière solaire. Comme la barrière à l'interface métal / semi-conducteur

joue un rôle important dans la réponse photovoltaïque du dispositif, nous avons essayé différents contacts supérieurs (ITO, Pt, Au, WO3). Malheureusement, aucun d'entre eux n'a pu produire un courant de court-circuit remarquable. Le meilleur dispositif à ce jour a été réalisé par BFCO 10 nm sur Nb: STO en utilisant 100 nm d'AZO comme contact supérieur. La figure 14 montre un schéma des niveaux d'énergie du dispositif.

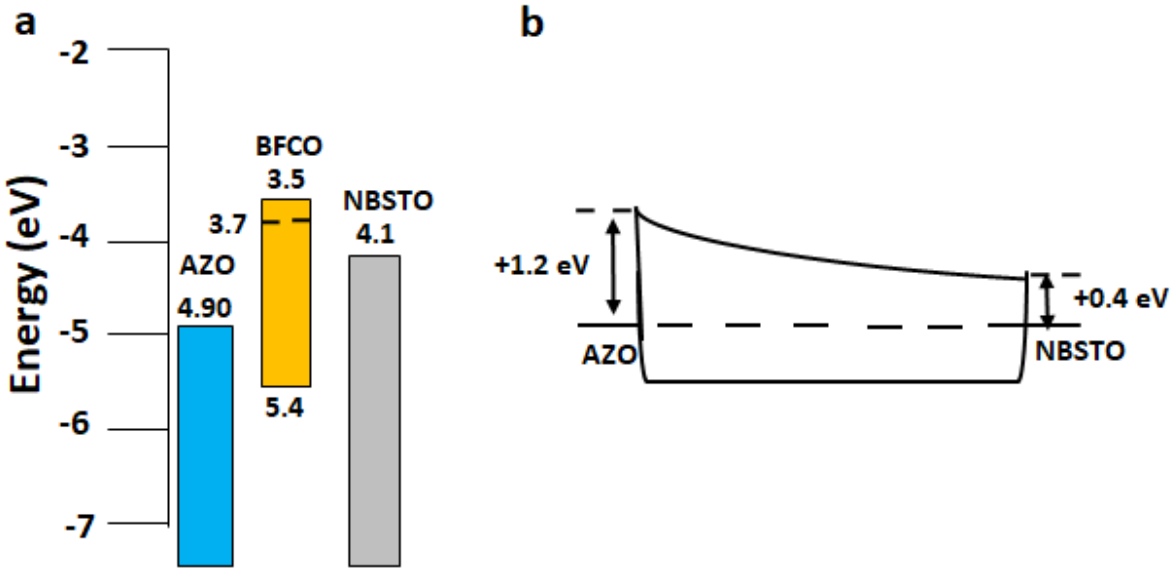

Fig.14 : Schéma des niveaux d'énergie de l'appareil AZO / BFCO / NBSTO

L'échantillon présente un Voc supérieur à 620 mV et un bon facteur de forme de près de 64%. Il est fort probable que la barrière de hauteur inférieure ait été capable de générer une polarisation énorme à l'intérieur du film et donc un Voc élevé. Le bon FF peut être lié à la faible résistance de la couche AZO plus mince. En revanche, la faible courante photo générée est probablement dû à une faible absorption de la lumière par le film mince absorbant BFCO.

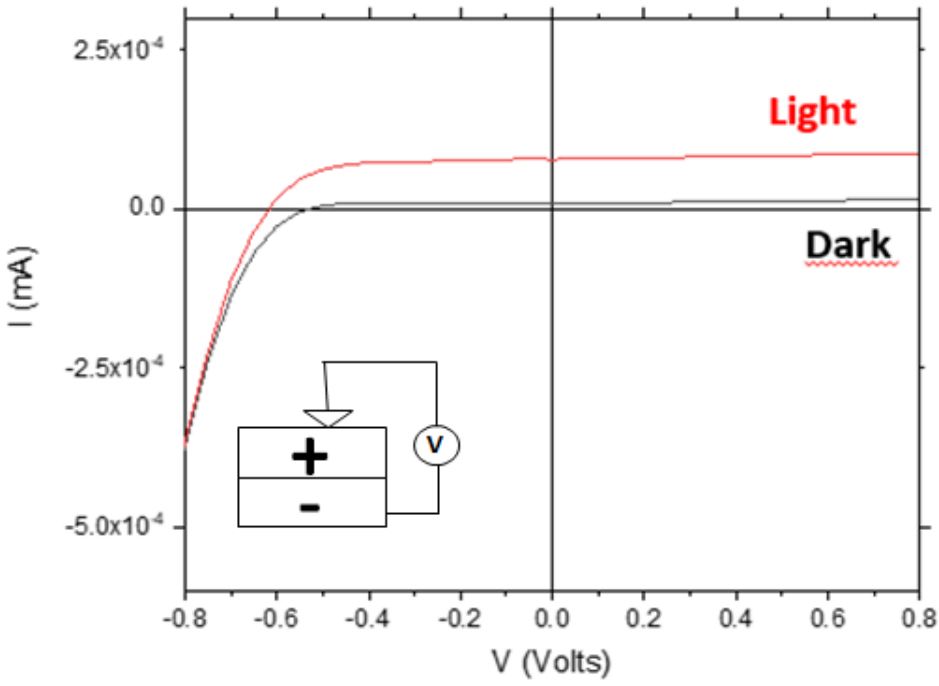

V_{oc} (V)	I_{sc} (nA)	FF
0.62	78.7	0.64

Figure 15 : Courbe I-V du dispositif AZO / BFCO / Nb: STO dans l'obscurité et l'éclairage et Paramètres photovoltaïques e

Pour conclure, l'étude sur le BFCO déposée par PLD a apporté un nouvel éclairage sur l'ingénierie de la bande interdite de ces films. En modifiant le paramètre de dépôt, nous avons pu moduler la bande interdite entre 2,64 eV et 1,96 eV. Nous avons démontré comment cet effet peut être lié au degré d'ordre Fe/Cr dans la double pérovskite au moyen de résultats expérimentaux et de calculs théoriques. Par la suite, le meilleur film obtenu pour une application photovoltaïque a été intégré à un dispositif et les propriétés électriques ont été évaluées. Nous avons montré comment le courant de court-circuit dépend de l'historique de la polarisation et de la forte influence de la lumière sur les propriétés ferroélectriques du film. En essayant différents contacts supérieurs, nous avons montré comment il est possible de modifier la réponse photovoltaïque. Les travaux futurs devraient maintenant se concentrer sur la création du dispositif de cellule solaire en mettant en œuvre l'interaction entre le film et le contact supérieur. En outre, il convient de trouver un moyen d'augmenter la conductivité du film sans affecter les propriétés ferroélectriques du matériau absorbant.

Alessandro QUATTROPANI

Synthesis of Ferroelectric oxides for photovoltaic applications

Résumé

Dans ce travail, nous avons étudié la croissance de films d'oxydes Bi2FeCrO6 (BFCO) en utilisant les techniques de sol-gel et dépôt par laser pulsé (PLD). Dans le cas de la voie chimique, des précurseurs en solution ont été préparés, puis déposés par centrifugation sur des substrats de silicium (100) ou de quartz. Les nombreuses analyses structurelles (DRX) et d'imagerie (SEM, TEM) effectuées sur ces films BFCO ont montré que les films sont assez homogènes mais présentent de nombreuses phases parasites qui peuvent être éliminés partiellement par recuit thermique rapide. Des dispositifs tests à base de films BFCO par sol-gel ont été préparés et qui ont montré des propriétés électriques limitées à cause des nombreux défauts. Des films BFCO ont également été produits par la technique PLD sur des substrats STO et NbSTO. Les propriétés structurelles, optiques et électriques sont présentées. La diffusion épitaxiale de haute qualité et les films en phase pure sont démontrés par diffraction des rayons X. Nous avons étudié l'évolution de paramètres tels que la bande interdite en fonction des conditions de croissance, montrant qu'elle peut être ajustée de 1, 9 à 2,6 eV. Ce comportement a été corroboré par des calculs théoriques sur l'arrangement atomique dans la structure BFCO. Les propriétés ferroélectriques sont étudiées par microscopie à force piézoélectrique. La lumière s'est avérée avoir un effet sur la polarisation. Il a également été démontré que la mémoire de la polarisation affecte la réponse photovoltaïque. Enfin, des dispositifs basés sur BFCO sont fabriqués et leurs propriétés photovoltaïques sont analysées. Des valeurs de tension de circuit ouvert de 600mV sont encourageantes pour la nouvelle génération de cellules solaires.

Mots-clé : Oxydes, pérovskites, ferroélectricité, cellules solaires, BPVE, BFCO

Résumé en anglais

In this work, we have produced Bi2FeCrO6 oxides (BFCO) by sol-gel technique and pulsed laser deposition (PLD). By sol-gel, precursors in solution were prepared, which are then deposited by centrifugation on silicon or quartz substrates. The numerous structural (XRD) and optical images (SEM, TEM) analyses carried out on these BFCO films show that the films are fairly homogeneous but exhibit many parasitic phases, which they can be partly eliminated by rapid thermal annealing. Finally, we present the first results obtained on BFCO-SG perovskite devices. On the other hand, BFCO films were deposited on STO and Nb:STO substrates. Their structural, optical and electrical properties are presented. High-quality epitaxial growth and pure-phase films are demonstrated by X-ray diffraction. We show that the band gap of the PLD-BFCO films can be tuned from 1, 9 to 2.6 eV thanks to the variation of growth conditions. Theoretical calculations has confirmed the observed behavior and highlight the importance of the ordering phase. The ferroelectric properties of the PLD films are studied by the piezoresponse force microscopy. Illumination is shown to have a strong effect on polarization. We show that the polarization memory affects the photovoltaic response. Finally, devices based on BFCO are manufactured and their photovoltaic properties are analyzed.

Keywords: Oxides, perovskites, ferroelectricity, solar cells, BPVE, BFCO